Green Synthesis of Copper-Doped Zinc Oxide Nanoparticles by Using *Solanum Incanum* Leaves Extract for Enhanced Antimicrobial and Antioxidant Activities

Adam Mengistu Mena

A Thesis Submitted to the Department of Applied Biology

For Partial Fulfillment of the Requirement for the Degree of Master's in Biotechnology

School of Applied Natural Science

Office of Graduate Studies

Adama Science and Technology University

June, 2023

Adama, Ethiopia

Green Synthesis of Copper-Doped Zinc Oxide Nanoparticles by Using *Solanum Incanum* Leaves Extract for Enhanced Antimicrobial and Antioxidant Activities

Adam Mengistu Mena

Main Advisor: Mohammed Naimuddin (Ph.D.)

Co-advisor: Buzuayehu Abebe (Ph.D.)

A Thesis Submitted to the Department of Applied Biology

For partial fulfillment of the requirement for the Degree of Master's in Biotechnology

School of Applied Natural Science

Office of Graduate Studies

Adama Science and Technology University

June, 2023

Adama, Ethiopia

DECLARATION

I declare that this thesis entitled **"**Green Synthesis of Copper-Doped Zinc Oxide Nanoparticles by using *Solanum incanum* Leaves Extract for Enhanced Antimicrobial and Antioxidant Activities**"** is my own work and has not been submitted to any university for a similar purpose. The references used in this thesis are duly recognized by proper citations.

Name of the student	Signature	Date

RECOMMENDATION

We the advisors of this thesis, hereby certify that we have read the revised version of the thesis entitled **"**Green Synthesis of Copper-Doped Zinc Oxide Nanoparticles by using *Solanum incanum* Leaves Extract for Enhanced Antimicrobial and Antioxidant Activities**"** prepared under our guidance by Adam Mengistu submitted in fulfillment of the requirements for the degree of Master's Science in Biotechnology. Therefore, we recommend the submission of a revised version of the thesis to the department following the applicable procedures.

Mohammed Naimuddin (Ph.D.)	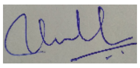	11-07-2023
Major-Advisor	Signature	Date
Buzuayehu Abebe (Ph.D.)	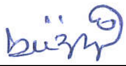	12-07-2023
Co-advisor	Signature	Date

APPROVAL PAGE

We, the advisors of the thesis entitled **"**Green Synthesis of Copper-Doped Zinc Oxide Nanoparticles by using *Solanum incanum* Leaves Extract for Enhanced Antimicrobial and Antioxidant Activities" developed by Adam Mengistu hereby certify that the recommendation and suggestions made by the board of examiners are appropriately incorporated into the final version of the thesis.

Mohammed Naimuddin (Ph.D.)		11-07-2023
Major Advisor	Signature	Date
Buzuayehu Abebe (Ph.D.)		12-07-2023
Co-advisor	Signature	Date

We, the undersigned, members of the Board of Examiners of the thesis by Adam Mengistu have read and evaluated the thesis entitled**"** Green Synthesis of Copper-Doped Zinc Oxide Nanoparticles by using *Solanum incanum* Leaves Extract for Enhanced Antimicrobial and Antioxidant Activities" and examined the candidate during the open defense. This is, therefore, to certify that the thesis is accepted for partial fulfillment of the requirement of the degree of Master of Science in Biotechnology.

Chairperson	Signature	Date
Internal Examiner	Signature	Date
Gizachew Haile (Ph.D.)		10/7/2023
External Examiner	Signature	Date

Final approval and acceptance of the thesis are contingent upon the submission of its final copy to the Office of Postgraduate Studies (OPGS) through the Department Graduate Council (DGC) and School Graduate Committee (SGC).

Department-Head	Signature	Date
School-Dean	Signature	Date
Office of Postgraduate Studies, Dean	Signature	Date

ACKNOWLEDGMENTS

The study would not be possible without the mercy of the Almighty God, who gives me strength, courage, and perseverance. I want to forward my deepest thanks to my advisor Dr. Mohammed Naimuddin for his crucial remarks, valuable support, sustainable and appreciable guidance, and comments in every step of this work. Also, my great thanks go to my co-advisor, Dr. Buzuayehu Abebe, for his supportive idea, smooth guidance, and fluent advice. I extend my gratitude to Adama Science and Technology University, Applied Biology Department, for the offer of an MSc scholarship and financial funds for this study. Lastly, I would like to express my heartfelt respect to my family for their support in various ways, and my friends who have helped me during this study.

TABLE OF CONTENTS

LIST OF TABLES

LIST OF FIGURES

FEGURE **PAGE**

LIST OF ACRONYMS

AMR	Antimicrobial resistance
ATCC	American Type Culture Collection
CIF	Crystallographic information file
DRS	Diffuse Reflectance Spectroscopy
3D-VESTA	3D visualization for electronic structural analysis
DMSO	Dimethylsulphoxide
DPPH	2, 2-diphenyl-1-picrylhydrazyl
EDXS	Energy dispersive X-ray spectroscopy
FESEM-EDS	Field emission scanning electron microscope energy dispersive spectroscopy
FTIR	Fourier transform infrared
GCD-Z	Green synthesized copper doped zinc oxide
HRTEM	High resolution transmission electron microscope
MBC	Minimum bactericidal concentration
MDR	Multi drug resistant
MHA	Mueller Hinton agar
MIC	Minimum inhibition concentration
MNPs	Metal oxide nanoparticles
MZI	Measurable zone of inhibition
NC	Nanocomposite
NPs	Nanoparticles
PL	Photo Luminescence
ROS	Reactive Oxygen Species
TGA	Thermo Gravimetric Analysis
XRD	X-ray Diffraction

ABSTRACT

Nanoparticles could become an indispensable, viable therapeutic option for treating drug-resistant infections. Nanometer-scale material synthesis using a green approach has received attention. The aim of the study was to synthesize bitter apple (Solanum incanum) leaf extract aided ZnO nanoparticles, and ZnO- ceftriaxone *conjugate for the evaluation of antimicrobial and antioxidant activities. The green synthesis parameters such as as temperature, pH, and volume ratio of the precursor to plant extract was optimized. The synthesized metal nanoparticle nanocomposite and conjugate were subjected to characterization and biological activity tests. The FESEM-EDS elemental mapping analysis proved the novelty of the green synthesis approach in synthesizing single ZnO and copper-doped ZnO composite with good dopant distribution. The XRD and TEM analysis of the synthesized nanomaterials showed nanometer-scale sizes (7-50 nm). The optical property adjustments from 3.04 to 2.97 eV for indirect Kubelka-Munk functions were confirmed from DRS-UV-vis analysis. The angle shift on the XRD pattern analysis confirmed the perfect dopant inclusion in the host lattice relative to a single ZnO. The lattice fringe values from HRTEM analysis confirmed the existence of both CuO and ZnO crystals with local heterojunctions. The conjugation of ceftriaxone with synthesized zinc oxide was highly confirmed by the peak at 270 nm on the UV-vis spectroscopy. Doping and heterojunctions have crucial values in charge transfer and visible light harvesting behavior, as proved by the PL analysis. The synergistic effects of doped composites and antibiotic conjugate showed greater antibacterial activity against both the gram-positive and gram-negative bacteria. The highest antibacterial activity was observed in the order of 43.3% <49.5%<71.5%<79.5% for ZnO<CuO<ZnO-AB<GCD-Z10.5, respectively. Similarly, the reduction in the MIC, MBC, and tolerance test values was also observed in the order of ZnO<CuO<ZnO-AB<GCD-Z10.5, respectively. This was plausibly a result of more reactive oxygen species (ROS) generation through bacteria-cell-catalyst interaction and the release of metal ions. The antioxidant activity of the doped nanoparticles and* ceftriaxone-ZnO conjugate was analysed *using the 2,2-diphenyl-1-picrylhydrazyl (DPPH) free radical scavenging assay. Their antioxidant potential was found to be in the order of ZnO<CuO<GCD-Z10.5<ZnO-AB, respectively. Thus, the overall analysis leads to the conclusion that the potentiality of synthesized materials has a future outlook for biological and medical applications, especially in the development of antimicrobials for combating antibiotic resistance bacteria.*

Keywords: Antibiotic resistance, Green synthesis, Doped nanoparticles, Synergistic effect, Antibiotic conjugate, Reactive oxygen species, Antibacterial activity, Antioxidant activity

1. INTRODUCTION

1.1. Background

The rapid spread of bacterial infections and the massive occurrence of antibiotic-resistant bacteria are increasing the worldwide mortality rate, which is estimated to reach up to 10 million deaths every year by 2050 with a treatment cost of USD 100 trillion (Maruthapandi *et al.*, 2020; Hassan *et al.*, 2017). In 2014, the World Health Organization (WHO) recognized the phenomenon of Antimicrobial resistance (AMR) as a major threat to global health, in response to the massive increase in populations of multi drug-resistant strains worldwide (Bengtsson-Palme *et al.*, 2018). A variety of factors, including antibiotic misuse and abuse, agricultural antibiotic use, rising income levels, and easy migration routes, have been reported to drive the spread of antimicrobial resistance. Multi drug-resistance (MDR) and AMR give rise to infections such as hospital-acquired, ulcerate skin, lung, urinary tract (UTI), catheter, ear, eye, Gingivitis, etc. leading to increased medical costs, and marked morbidity and mortality. Clinically relevant bacteria such as *Escherichia coli* (*E. coli*), *Klebsiella pneumoniae* (*K. pneumoniae*), *Enterobacter* spp., *Proteus* spp., *Staphylococcus aureus* (*S. aureus*), *Pseudomonas aeruginosa* (*P. aeruginosa*), *Acinetobacter* spp., methicillin-resistant *S. aureus* (MRSA) among others have been implicated in infections, AMR and MDR, respectively.

AMR and MDR patterns in gram-negative and gram-positive bacteria give rise to infections that are either difficult to treat or impossible to cure with conventional antimicrobial agents. Consequently, it becomes an urgent and nonstop issue to find solutions to combat this widespread phenomenon associated with bacteria and other microbes as well. Photosensitive materials capable of reducing oxygen and oxidizing water molecules to produce a highly oxidizing agent may potentially provide possible solutions. Zinc oxide (ZnO) is one of the current choices as a novel antibacterial material that has the capacity to generate reactive oxygen species (ROS). It is one of the wide-band gap (3.34 eV) semiconductor materials with anexciton band energy of 60 meV. ZnO has wide applications due to its unique properties, although with some drawbacks, such as being incapable of harvesting the majority of the solar spectrum (the visible range) and having photon-induced e^-/h^+ recombination properties (Saravanan *et al.*, 2013). Transition metal or metal ion inclusion, or creating a defect or shallow state within the ZnO band gap, has been extensively studied and found to be one of the crucial techniques used to advance the drawbacks of ZnO and increase its biomedical application (Karthik *et al.*, 2022).

Oxides of copper, a narrow band gap material, have extraordinarily good properties for biocidal applications (Verma and Kumar, 2019). Doping of copper in the ZnO lattice creates an accepter level near the ZnO conduction band at a 0.17 eV energy level and near the conduction band at about 0.45 eV, which consequently induces green photo luminescence emission (Agarwal *et al.*, 2019). The ionic radii of copper ions (0.073 nm) are comparable with those of Zn ions (0.073 nm), which create significant optoelectrical and biological property changes in ZnO after inclusion (Khalid *et al.*, 2021). Furthermore, CuO-ZnO hetero junction (p-n heterojunction (type II, staggered gap type)) diminishes the ZnO's e^-/h^+ recombination properties, consequently enhancing the charge separation and visible light harvesting properties, as well as increasing stability and reusability (Bekru *et al.*, 2022; Costas *et al.*, 2022). The synergistic effects of CuO-ZnO heterojunction on antibacterial activity have also been reported (Khalid *et al.*, 2021). Additionally, the conjugation of antibiotics that contain various functional groups that enable them to interact with metal ions and form antibiotic-metal nanoparticle complexes is crucial to improving biological activities (Kara *et al.*, 1991). These have contributed to the high generation of ROS due to the carboxyl, hydroxyl, amines, and others that are capable of scavenging the radicals (Hwang, 2012).

There are several nanoscale material synthesis technologies for both chemical and physical approaches. However, costs, hazardous chemical usage, and toxic byproducts are some of the many disadvantages associated with these approaches. Thus, the use of the biosynthesis approach, specifically using plant metabolites such as stabilizing, reducing, and gelating agents, received attention due to easy availability, low cost and biocompatability (Momeni *et al.*, 2016). *Solanum incanum* L., which is the source of several groups of phytochemicals and multiple metabolites, is one of the medicinal plants used as a reducing and capping agent (Lashin *et al.*, 2021). There are recent reports regarding the green synthesis of ZnO nanoparticles (NPs) and copper-doped ZnO nanocomposites (NCs) for different applications. For example, Thi *et al.*, (2020), synthesized ZnO NPs in the presence of orange fruit peel extract as a biological reducing agent. Besides, copper-doped ZnO NCs were synthesized using plant extracts of *Clerodendrum infortunatum*, *Synadium grantii*, *Erbascum sinaiticum benth*, *and Piper chaudocanum*, respectively (Bekru *et al.*, 2022; Karthik *et al.*, 2022; Khan *et al.*, 2018). To the best of our knowledge, *S. incanum* plant extract has never been used for the green synthesis of current NPs. This work also gives insight into the chemistry of doping and hetero junction in detail, and conjugation of NPs with antibiotics which are crucial parameters for the enhancement of the properties of the materials in several applications such as antibacterials.

Thus, this study aims to synthesize the ZnO-NPs, CuO-NPs, copper-doped ZnO NCs, and NPs-AB conjugate using a green approach in the presence of *S. incanum* plant extract for the development of antimicrobial agents. The determination of the doped particles distribution was analysed by using FESEM-EDS with high purity. The TEM-HRTEM-SAED analysis was investigated to the confirmation of the size crystallinity, and heterojunction formation between CuO and ZnO. The XRD pattern analyses were observed for the evaluation of crystalline nature of synthesized NPs and the angle shift or the appearance of new peak due to doping. The optical properties of the NPs and composite were compared according to the DRS-UV-vis and PL analysis. The doping and heterojunction strategies also improve the material charge transfer properties without recombination. The continuous charge transfer process (electron-hole relaxation) results in a reaction with oxygen and water that produces a high oxidizing agent, ROS, which is beneficial for several applications such as catalysis and antibacterial activity (Ben Salem *et al.*, 2023). The conjugation of antibiotics with the NPs has been shown to be beneficial for synergistic effect (Vazquez-Muñoz *et al.*, 2019). The greater ROS generation and novel antibacterial activity for the doped composite and conjugate than single ZnO were also confirmed in this study.

1.2. Statement of Problem

Infections by pathogenic bacteria are one of the most global problems and a constant health risk in all countries. Today, the burden of infectious diseases on health, economics, and other social dimensions is so complex that global costs cannot be estimated (Dye, 2014). Current antimicrobial therapies are declining in efficacy due to their limited variety, antagonistic interactions, and, above all, the impact of unfinished antibiotic therapy leading to the development of microbial resistance. MDR bacteria pose one of the world's most serious public health problems. The emergence of resistant microbes often reduces the effectiveness of current treatments and poses a serious public health risk (Versporten *et al.*, 2018). It also adversely affects many areas of human activity, such as agriculture, aquaculture, and veterinary medicine. Unfortunately, the emergence and spread of antibiotic resistance are global challenges.

Strategies for maintaining antibiotic efficacy have been recommended by various global scientists. One alternative to combating MDR organisms is the use of nanoantibiotics (nanomaterials with antimicrobial properties). Due to their antiviral and antibacterial properties, synthetic green zinc and copper nanoparticles are today's most promising nanoantibiotics (Westerhoff *et al.*, 2015). Although nanotechnology is widely used in developed countries, it is still in its infancy in Ethiopia, so there is a lot of room for advancement in this area. Specifically, there are some studies that have been done on the synthesis of silver nanoparticles using *S. incanum* callus (Auta, 2011), but there are no papers reported on the synthesis of copper and zinc nanoparticles using the current plant leaves, their synergistic effect with each other and with conventional medicine. Mostly, it has been proposed as a medicinal plant for various microbial infections in Ethiopia as well as for its availability, but not much attention has been paid to its contribution to the synthesis of certain nanoparticles.

1.3. Objectives of the Study

1.3.1. General objective

The main objective of this study was to synthesize ZnO nanoparticles and nanocomposite and evaluate their biological activities against antibiotic resistant bacterial strains.

1.3.2. Specific objectives

The specific aims of this study were:-

- To extract phytochemical from *S. incanum* leaves.
- To evaluate the phytochemicals that assist in nanoparticles synthesis as reducing and capping agents.
- To optimize the synthesizing parameters for green synthesis of nanoparticles.
- To synthesize copper oxide, zinc oxide, copper-zinc oxide nanoparticles, and zinc oxide-ceftriaxone conjugate using the plant leaves extract.
- To characterize the synthesized nanoparticles
- To study the biological activities of the synthesized nanomaterials on antibiotic resistant bacteria.
- To evaluate the synergistic effect of synthesized nanomaterials with each other on biological activities.

1.4. Significance of the Study

Improving the antimicrobial activity of nanoparticle-based antibiotics will allow us to fight bacterial infections that may be resistant to conventional antibiotic treatment and provide additional therapeutic possibilities in the healthcare, veterinary, and agricultural sectors. Therefore, nanoantibiotics will certainly have a potential impact on economic and social issues, as they can help alleviate the current antibiotic resistance crisis. With its exciting applications, it could bring about a revolutionary change in the fields of antibiotic treatment, medical therapy, improved drug delivery, and unmet medical needs. Furthermore, the study was observed as highly potent in providing a good understanding of working groups in related fields. The success of this work may trigger inspiration for the coming generations to adopt nano-based advanced research for the scientific progress of the country.

1.5. Scope of the Study

The scope of this study was limited to the synthesis of ZnO, CuO and CuO doped ZnO using *S. incanum* leaf extract; optimization of parameters for synthesis, characterization of synthesized nanoparticles and nanocomposite by using XRD, TGA, DRS, PL, FTIR, SEM-EDX, TEM, and UV-Vis spectroscopy; antibacterial tests of the synthesized nanoparticles and nanocomposite against antibiotic resistant bacterial strains such as *E. coli, P. aeruginosa, S. aureus, and S. pyogenes.* In addition, we also prepared ZnO-antibiotic conjugate to evaluate the antibacterial and antioxidant activities.

2. LITERATURE REVIEW

2.1. Introduction to Antimicrobial Resistance

Antimicrobial resistance (AMR), which renders common life-threatening illnesses difficult or impossible to treat, is still on the rise globally and has serious socioeconomic and public health consequences. According to recent projections, if AMR is not controlled by 2050, it might result in 10 million deaths annually and up to $100 trillion USD in economic losses worldwide. In reality, according to earlier estimates, there were 4.95 million deaths associated with AMR in 2019 (Stanton *et al.*, 2022).

Antibiotic resistance genes (ARGs) and antibiotic-resistant bacteria (ARBs) with human-like biochemical and genetic traits have also been found in animals and their habitats, which indicates that antibiotic resistance is circulating throughout the ecosystem (Nadimpalli *et al.*, 2020). Because the health of different fields, such as humans, animals, and environments, interact with one another, it is vital to combat AMR outside the bounds of each relevant field. This is done by using the concept of "One Health" (Rousham *et al.*, 2018).

Wastewater is frequently a significant source of AMR since it contains a variety of AMR from people, animals, and surroundings. Because of the selection pressure that they exert on bacteria, the leftover antimicrobials in wastewater from people, animals, and crop plants are also a major reason for concern (Frascaroli *et al.*, 2021).

A recent metagenomic analysis of ARGs in untreated sewage around the world revealed a higher abundance of ARGs in wastewater in low- and middle-income countries than in high-income countries, reflecting the state of sanitation and general health (Baba *et al.*, 2022). Although the direct discharge of untreated human waste containing many ARB and ARGs into the soil and water environment is one of the major contributors to environmental AMR contamination. Sewage treatment plants were concerned to ensure the removal of harmful microorganisms, so they play a pivotal role in reducing AMR (Bürgmann *et al.*, 2018). However, because they were not intentionally designed to manage AMR, ARB and ARGs can persist even after sewage treatment plants(STP) and remain at detectable levels in water environments receiving the discharge (Baba *et al.*, 2022).

2.2. Antibiotic-resistant Bacteria

Since the most drug prescribed from hospital are used intensively and frequently. It favors the selection of resistant strains, which can cause serious infections in patients (Crabtree *et al.*, 2019). Resistance leads to ineffective clinical treatment in the case of some bacterial species, increasing the problem of microbial resistance to antimicrobials (Wilson *et al.*, 2020). Resistance such as extended-spectrum β-lactamase producing (ESBL), *Klebsiella pneumoniae* carbapenemase (KPC) producing, and methicillin-resistant *Staphylococcus aureus* (MRSA) lead to therapeutic failure, high treatment cost, and patient death (Sánchez-López *et al.*, 2020). Among the multi-drug resistance microorganisms in hospital, the most common is MRSA strains that are most prevalent pathogens (Table 1).

Recent study estimates that death rate due to antimicrobial resistance may reach to 10 million by 2050 (Wilson *et al.*, 2020). The statins are known for their antihyperlipidemic effects by competitively inhibiting the enzyme HMG-CoA reductase, decreasing cholesterol biosynthesis. This drug is also known to present pleiotropic effects, such as anti-inflammatory and antithrombotic (Jain and Ridker, 2005). Furthermore, in 2008 a study that described the antibacterial effects of statins found that simvastatin and fluvastatin were active against MRSA and Vancomycin-resistant *Enterococcus* (VRE) strains. Metals have been used since ancient times as antibacterial agents and present different properties and spectra of action. Among the metals, silver is one of the most commonly used due to its efficiency as an antimicrobial and low toxicity, being impregnated in utensils and materials used in medicine (Jerwood and Cohen, 2007).

In 2017, the World Health Organization (WHO) first published a list of twelve families of antibiotic resistant bacteria that pose the greatest threat to human health. The WHO categorizes bacteria into critical, high and medium priority, according to their urgency of need to develop new antibiotics to combat these pathogens. The pathogens included in the most critical group are the multidrug resistant bacteria (Table 1) that pose threats to patients in hospitals and nursing homes as well as to patients whose conditions require medical devices such as ventilators and blood catheters. Critical-priority bacteria comprise *Acinetobacter*, *Pseudomonas*, some Enterobacteriaceae such as: *K. pneumoniae, E. coli* and *Enterobacter spp.* (Bowden *et al.*, 2017). These pathogens are resistant to multiple antibiotics and can cause severe and often fatal infectious diseases such as bloodstream infections and pneumonia. The high priority category includes bacteria such as *Enterococcus* *faecium* and *Staphylococcus aureus* that are resistant to various antibiotics, such as vancomycin and fluoroquinolones (Karataş *et al*., 2020). The medium priority category includes bacteria such as *Streptococcus pneumoniae* and *Shigella* that, although they may have some resistance, effective antibiotics are still available that can kill them (Scandorieiro *et al.*, 2016).

Table 1. Different antibiotic resistant pathogens

No	*Bacterial spp*	Description	Antibiotic resisted	References
1	*Staphylococcus aureus*	Gram-positive, facultative anaerobe, catalase and coagulase-positive	Penicillin, Methicillin	(Jubeh *et al.*, 2020)
2	*Escherichia coli*	Gram negative, facultative anaerobic	Ampicilin, Amoxacillin	(Tornberg-Belanger *et al.*, 2022)
3	*Bacillus subtilis*	Gram positive, aerobic spore-forming bacterium	Erythromycin, Ampicilin	(Yesuf *et al.*, 2016)
4	*Salemonella typhi*	Gram negative, facultatively anaerobic	Ciprofloxacin, Ampicilin	(Tornberg-Belanger *et al.*, 2022)
5	*Klebsiella pneumonia*	Non-fastidious, commonly encapsulated gram-negative bacillus	Carbapenem	(Jubeh *et al.*, 2020)
6	*Pseudomonas aeruginosa*	Aerobic gram-negative bacterium	Ceftazidime and cefepime	(Scandorieiro *et al.*, 2016)
7	*Enterococci faecalis*	Normal gram-negative intestinal microbiota	Vancomycin	(Scandorieiro *et al.*, 2016)
8	*Enterococci faecium*	Gram-negative intestinal microbiota	Vancomycin	(Scandorieiro *et al.*, 2016)
9	*Enterobacter aerogenes*	Non-fastidious gram-negative rods that are sometimes encapsulated	tigecycline and colistin	(Tornberg-Belanger *et al.*, 2022)
10	*Mycobacterium colombiense*	Phylum Actinomycetota, belonging to the genus Mycobacterium.	Tetracycline	(Tan *et al.*, 2016)
	Mycobacterium tuberculosis	Pathogenic bacteria in the family Mycobacteriaceae and the causative agent of tuberculosis.	Tetracycline	(Tan *et al.*, 2016)

2.3. Nanotechnology and its Importance

Nanotechnology is a technology related to design, formation, and usage of materials with nanosized components and dimensions of these components (Tatli Seven *et al.*, 2018). It is the processes carried out by controlling the matter at the molecular level. Medicine, devices and systems that are formed and used due to their small dimensions have different properties or functions. It is possible to use nanotechnology in various fields such as medicine, pharmacy, food industry, veterinary medicine, and textile. Nanotechnology is thought to be originally designed for vaccines and cancer drugs (Sanginario *et al.*, 2017).

As the different studies have shown that the positive results have been obtained from nanomaterial treatment of brain tumors since the drugs can be transported to the target site via blood and brain barrier by using nanoparticles. All the nanosystems used provide some advantages in pharmaceutics when compared to conventional systems. These advantages are increasing the therapeutic effect by increasing the half-life of the drugs, reducing the side effects of the drugs, monitoring the release and distribution of the drugs, staying in circulation for a long term (Luo *et al.*, 2022), monitoring of the treatment efficiency, developing effects without harming other systems and organs, avoiding some drug use problems like drug application at night, forgetting to take or administer drugs, using drugs in short time intervals, etc.. Also in other area such as industry, nanotechnology has high acceptability due to its compatible size (Singh *et al.*, 2004).

In the development of drug delivery applications, nanocarriers are designed in different pharmaceutical forms including oral, parenteral, pulmonary, nasal, transdermal, or topical formulations (Karatas *et al.*, 2020). Delivery of the drug to the structure where it will activate is one of the main problems of pharmaceutical technology. Drug use is limited due to the situations such as low drug solubility, overdose and formation of toxicity, non-specific transfer, short halflife period etc. Today, many researchers participate in activities of developing new drug delivery systems in order to minimize the increasing problems of the drugs and to turn new developments into clinics (Onoue *et al.*, 2012). In addition to that nanotechnology has another different application area in health such as cancer treatment (damage the rapidly proliferating cells), wound healing that means slower release of the nanoparticles than the gel increases the retention time on the skin, treatment of infectious diseases, diabetes treatment, etc. (Karatas *et al.*, 2020).

2.4. Synthesis Methods of Nanoparticles

Nanoparticles are present in the forms of needles, spheres, prisms, and cubic bars. They are colloidal structures with dimensions varying between 10 and 100 nm. They are formed of natural or synthetic macro molecules (Cushing *et al.*, 2004). These are the systems where the active substance is dissolved, absorbed or bound in the particle. In the pharmaceutical sector, their practical use in the applications such as direct binding to the active substance, confinement, and targeting has brought them into a preferred position (Karatas *et al.*, 2020). They are called as nanocapsules or nanospheres according to their preparation techniques. Nanocapsules are vesicular structures. The drug is confined in a cavity and surrounded by a polymer membrane. Nanospheres are the matrix systems in which the drug is physically dispersed. Nanoparticles provide advantages due to some of its characteristics. One of them is that they have small particle sizes. Thus, they pass through the small capillary and are taken into the cell, and it is provided to accumulate the active substance in the target site (Bowden *et al.*, 2017).

Different approaches can be used for nanoparticle synthesis. This includes: physical, chemical, biological, or combination between them; the final characteristics of products are important such as to fully reply to the requirements. The methods used for synthesizing nanoparticles can be framed in two main ways: top bottom approach and bottom up approach (Salleh *et al.*, 2020). The principle of the top bottom synthesis is to take a bulk piece of material and then modify it into the wanted nanostructure and subsequent stabilization on the resulting nanosized metal oxide nanoparticles by the addition of colloidal protecting agents (Landage *et al.*, 2014).

The top-down or top-bottom approach involves the use of bulk materials and reduces to the nanoparticles by the way of physical, chemical, or mechanical processes. In this approach, it is starting from larger structures, which decomposed into smaller units until reaching the desired size. The bottom-up synthesis refers to the construction of a structure atom-by-atom, molecule-by-molecule, or cluster-by-cluster. This approach is employed in reverse of NPs which are formed from simpler substances; therefore, this procedure is called building up approach. Examples of these cases are sedimentation and reduction techniques which includes sol-gel, green synthesis, spinning/spraying, and biochemical synthesis (Khan *et al.*, 2018).

2.4.1. Physical method

Top-down synthesis incorporates physical techniques like evaporation-condensation, laser ablation, and electron beam evaporation processing. One of the key benefits of using these physical approaches is the lack of solvent contamination during nanoparticle formation. In the ball milling process, metal components are combined with milling balls in a certain proportion together with inert gas while rotating at a high speed. These variables determine the size of the nanoparticles that are produced (Salleh et al., 2020). In addition, since capping agents are rarely used, the agglomeration effect is frequently a serious difficulty for these approaches. There are some drawbacks to chemical reduction utilizing high temperatures or pressure, including the high energy costs associated with raising the temperature of the environment near the source material and the length of time needed to attain thermal stability (Scandorieiro et al., 2016).

2.4.2. Chemical method

The chemical processes result in the production of particular nanoparticle forms that are effective against microbes. The most frequent and straightforward method for creating stable, colloidal dispersions of silver nanoparticles in water or organic solvents is chemical reduction. Sodium borohydride, trisodium citrate, and elemental hydrogen make up the majority of the reducing agent (Mitchell et al., 2021). For instance, the Turkevich method of reducing silver ions (Ag^+) in aqueous solutions results in silver particles that have a diameter of several nanometers. Silver atoms are created via the reduction of different complexes with Ag^+ ions, which is followed by their aggregation into oligomeric clusters. The development of colloidal silver particles may be facilitated by these clusters (Marinescu et al., 2020).

2.4.3. Green Synthesis of MNPs

Biological synthesis involves the synthesis of nanoparticles by using plant extracts and microorganisms such as bacteria and fungi. Phytonanotechnology is considered as a new field for the synthesis of nanoparticles which is eco-friendly, simple, cost effective. scalability, biocompatibility and synthesis of nanoparticles via universal solvent as reducing agents are the advantages of phytonanotechnology. Phytonanotechnology use plants for the synthesis of nanoparticles. Nanoparticles are synthesized using different parts of plant such as root, fruit, stem, seed and leaf (Ahmad *et al.*, 2021). The mechanism for the synthesis of nanoparticles using plants extract has been clarified by different scholars. It has been illustrated that organic acid, proteins, vitamins and secondary metabolites such as alkaloids, flavonoids, terpenoids, polysaccharides and heterocyclic compounds are responsible for the synthesis of various types of nanoparticles (Mat Yusuf *et al.*, 2020).

Microorganisms are also considered nanofactories that hold wide potential as cost effective tool, eco-friendly, avoid toxic and harsh chemicals and energy demand for the synthesis of nanoparticles (Luu *et al.*, 2020). Various reductase enzymes are present in the microorganisms due to which microorganisms have the ability to accumulate and detoxify heavy metals (Rizvi *et al.*, 2020). These reductase enzymes play vital role in reduction of metal salts into the nanoparticles. Over the past few years, various microorganisms such as yeast, fungi and bacteria have been shown to be used in the production of NPs (Rizvi *et al.*, 2020).

2.5. Heterojunction of MNPs

Due to the synergistic impact, constructing a binary, ternary, or more heterojunctions can increase the surface area to volume ratio and decrease the recombination of electron/hole pairs as compared to single metal oxide nanomaterials. The heterojunction can be created using metal oxides with the same band gap or distinct band gaps. For binary metal oxides, it can form using either the negative-negative (n-n) or positive-negative (p-n) method, while for ternary heterojunction, it can form using either the p-n-n or n-n-n method (Abebe *et al.*, 2021). For instance, researchers found that when pure Fe2O3 and NiO combine to produce binary nanocomposites, their antibacterial properties are improved. The inhibition zone of α-Fe2O3/ NiO is larger than that of NiO and α-Fe2O3 separately (Bhushan *et al.*, 2021).

Colotropis gigantea leaf extract was used to make CuO-ZnO composite materials, which also exhibited strong antibacterial action against *E. coli* and *S. aureus* germs. Green synthesis techniques were used by to create granular nanoflakes shaped MgO/ZnO nanocomposite materials, granular nanoflakes morphologies of ZnO, and seedless fruit extract from the *Ricinus communis L*. plant (Vaez and Javanbakht, 2020).

2.6. Antibiotic-Metal nanoparticles (MNPs) conjugates

Antibiotics contain several electron-rich functional groups which act as potential metal binding sites for antibiotics- metal complex (AMC) formation**.** The metal complexes of antibiotics play a significant role in medicinal chemistry and the related bioprocesses in the human physiological system. The pharmacological behavior of antibiotics depends upon metal coordination/complexation (Kara *et al.*, 1991).

The antibiotics are known to form chelates with metals, such as Mg^{2+}, Ca^{2+}, Fe^{2+}, Cu^{2+} and Zn^{2+} in blood plasma for effective transport of the drug in intercellular spaces, inhibit bacterial protein or cell wall synthesis, and regulate efflux mechanisms of bacterial resistance (Zebedee and Lamb, 1988). Inside cells, tetracycline (TET) predominantly occurs as a complex, $Mg (TET)^{+}$, which represses the synthesis of protein in bacterial cells via binding to 30S subunit of the ribosomal unit (Pioletti, 2001). Other tetracyclines, like minocycline and doxycycline, also interact with structural calcium and/or zinc metal ions of matrix metalloproteinases. The antibacterial activity of quinolones in the human body largely depends on their reduced bioavailability due to coordination with metal ions like Al^{3+}, Fe^{2+} and Cu^{2+} (Kara *et al.*, 1991).

2.7. The Role of Phytochemicals present in the plant extract for Nanoparticle Formation

Due to the phytochemicals present in the extracts, which play a significant role in the synthesis of metal and metal oxide nanoparticles, numerous plant parts, including leaves, peels, roots, seeds, barks, fruits, and gums, are used in the preparation of these particles (Din *et al.*, 2020). The bio reduction of metal ions to create nanoparticles has a great potential for the phytochemicals flavones, polyphenols, terpenoids, sugars, ketones, aldehydes, carboxylic acids, amides, alkaloids, phenolic acids, and proteins (Sorbiun *et al.*, 2018). Many scientists believe that plant extracts function in the formation of copper oxide nanoparticles as both reducing and stabilizing agents. As the previous studies report on CuO nanoparticle synthesis using plant extracts suggested that the extract acted as reducing as well as capping agents during nanoparticle formation (Crabtree *et al.*, 2019).

By reducing metal ions with a few chemical molecules, metallic oxide nanoparticles can be synthesized. *Momordica charantia* fruit extract contains gallic acid, which has been utilized as a catalyst to reduce copper ions into CuO nanorods that can combat bacterial strains that are resistant to a variety of drugs (Crabtree *et al.*, 2019), claim that the aqueous extract of the husk of the oak fruit contains functional groups, such as phenolic and flavonoids, that can reduce and cap the nanoparticles. Controlling the size and stability of the nanostructured material was also made easier by the reduction technique.The stability of nanoparticles can be attributed to the formation of stable bonding between metallic nanoparticles and phytochemicals present in the leaf extract (Ahmad *et al.*, 2021).

Additionally, the FTIR results revealed that the presence of flavonoid and phenolic acids in a particular plant leaf extract had a significant role in the reduction of copper ions and the creation of nanoparticles. In colloidal synthesis, capping agents play a significant role in controlling the particle morphology, stabilizing the nanoparticles, and inhibiting further development and agglomeration (Hasheminya and Dehghannya, 2021).

Polysaccharides including starch, dextran, and heparin, which are often used as capping agents in plant extract and are safe for the environment, are introduced and assessed from a green chemistry perspective. The *Ocimum tenuiflorum* leaf extract causes the reduction of Cu^{2+} ions to Cu nanoparticles and functions as a capping agent, according to a study (Mekawi *et al.*, 2019). It may be inferred from this that plant extracts are a great and safe source for the synthesis of metals and metal oxide nanoparticles, which are essential but non-toxic .

Consideration should be given to using less dangerous and energy-saving capping agents in nanoparticle synthesis as part of a green synthetic strategy for laboratory research and commercial manufacturing (Singh *et al.*, 2018).

2.8. Bitter Apple (*Solanum incanum*)

S. incanum is a medicinal plant which belongs to the family *Solanum L.* (*Solanaceae*) and is an important plant taxon that comprises many multipurpose flowering plants in several communities and cultures. It is one of the species with multiple traditional applications in many Ethiopian communities. It has several species known for their medicinal importance. The species is native to and widely distributed in the Horn of Africa. It has thorny leaves, yellow fruits, and blue flowers with yellow pistils (Abebe *et al.*, 2019). It propagates by seeds, and the seeds germinate slowly. *S. incanum* is common around houses, overgrazed grasslands, wastelands, and road sides (Sbhatu and Abraha, 2020). *S.incanum* L. is used to treat sore throat, stomach-ache, head-ache, painful menstruation, liver pain and pain caused by onchocerciasis, pneumonia and rheumatism throughout tropical Africa. The leaf sap is used for washing painful areas, and ash of burnt plants mixed with fat applied externally to treat pain. For relief of tooth-ache a root infusion is used as mouth wash, fruit or root is rubbed on the gums or smoke of burning seeds is inhaled.

The fruits of *S. incanum* are found to be the source of several groups of phytochemicals, including terpenes, flavonoids, bioflavonoid, xanthenes, and multiple metabolites like tannins, saponins, cyanates, and oxalate, and anthraquinones as well as steroid glycosides in the form of glycoalkaloids such as solanine and solasonine. The utilization of *S. incanum* plants for the biosynthesis of nanoparticles involves high interests of its content of secondary chemicals that are potent reducing agents for metal ions. Likewise, the leaves of *S. incanum* are rich in minerals such as K and Ca (Auta, 2011).

2.9. Antibiotic action mechanism of MNPs.

The therapeutic activity of many antibiotics originate from their ability to inhibit cell wall synthesis, interfering with the expression of essential proteins and disrupting DNA replication machinery (Figure 1). However, bacteria have developed the ability to resist each of these mechanisms of action. One fundamental mechanism of bacterial resistance is alteration of the target of the antibiotic. For example, modification of cell wall components confers resistance to vancomycin, whereas altered structures of ribosomes resist tetracycline (Wang *et al.*, 2017). Similarly, bacteria can overexpress enzymes such as β-lactamases and aminoglycosides to degrade antibiotics. Additionally, overexpression of efflux pumps enables bacteria to evade multiple antibiotics simultaneously. Finally, many pathogens such as *Chlamydophila pneumonia* reside inside the cellular compartments of the host cells to escape from the antibiotics that are mostly confined to extracellular space.

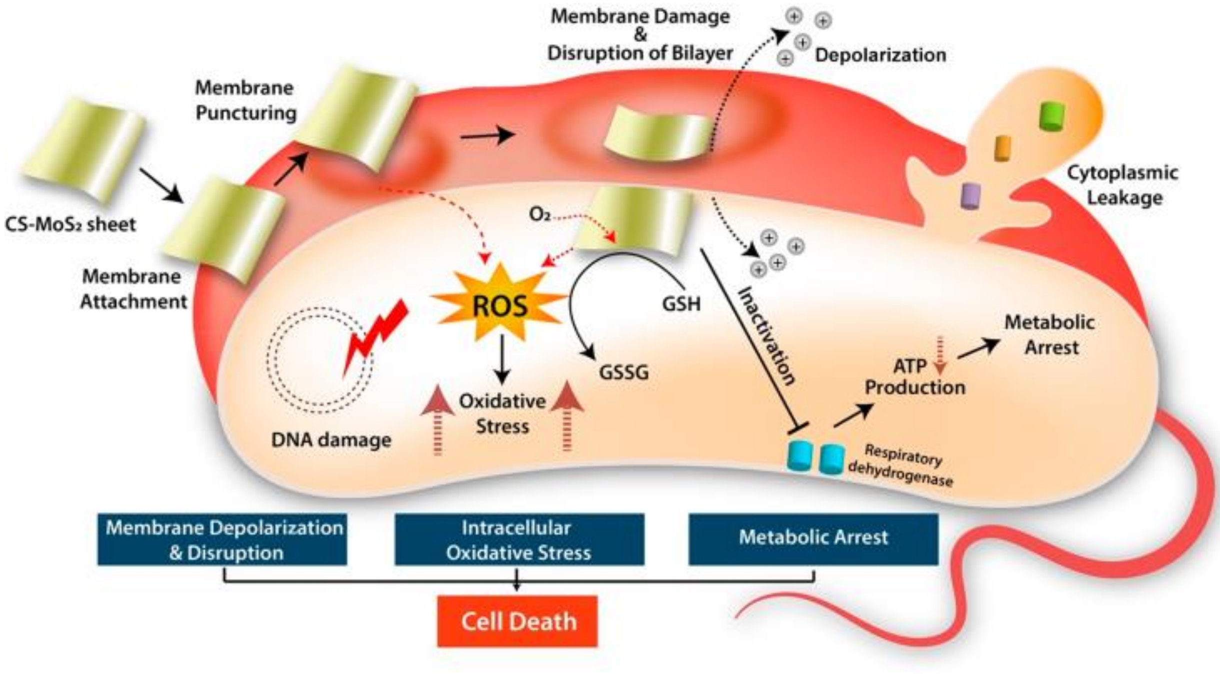

Figure 1. Antibacterial mechanisms for bacterial cell activity inhibition by the electrostatic and/or van der Waals interaction of NPs and NCs with the bacterial cells, which leads to ROS generation and oxidative stress creation (Roy *et al.*, 2019).

Because of their distinctive physio-chemical characteristics, nanoparticles can circumvent the mechanisms that cause bacteria to become resistant to antibiotics. This allows them to use a variety of innovative bactericidal pathways to produce antimicrobial action. The bacterial membrane can be disrupted by nanomaterials, allowing cytoplasmic components to flow out (Gupta *et al.*, 2016). Nanomaterials that penetrate the membrane can potentially bind to unicellular elements including DNA, ribosomes, and enzymes to interfere with normal cellular function. Cell death can come from oxidative stress, electrolyte imbalance, and enzyme inhibition caused by cellular machinery disruption (Wang *et al.*, 2017). Nanomaterials' primary material, shape, size, and surface functionalization all have a role in the bactericidal paths they take (Figure 1).

3. METHODS AND MATERIALS

3.1. Description of the Study Area

The study was carried out in Adama Science and Technology University, Applied Biology and Chemistry Laboratories. The plant sample has been collected from Adama city around ASTU and the other chemicals and buffers were purchased from authenticated chemical markets. Adama is located in East Shewa zone, Oromia regional state, located at 99km South East from Addis Ababa, the capital city of Ethiopia. Adama is found at an average altitude of 1712m above sea level and annual rain fall of 7600mm and mean manual monthly temperature of 21^{o}C. The climate of the area is hot or arid type. It is located between 8°33'35′N–8°38′46"N latitudes and 39°10′57′E–39°30'15′E longitudes (Hirpha *et al.*, 2020).

3.2. Collection of Plant and Identification

Solanum incanum sample was collected on January 20, 2023, from the Adama, Oromia Region of Ethiopia. The plant material was identified and voucher specimen number AM-001 was deposited at the National Herbarium of Ethiopia, Addis Ababa University, Ethiopia.

Figure 2. Morphological view of *S. incanum.* It has thorny leaves, yellow fruits, and blue flowers with yellow pistils.

Fresh leaves of *Solanum incanum* that weigh about 1 kg were collected from study area. Just after the collection of plant material, it was brought to the laboratory, washed thoroughly with fresh water, and then washed with distilled water thrice. The washed plant material was allowed to air dry in the lab, crushed manually, and ground by an electric grinder to get a fine-textured powder. The powder was then sieved through a mesh (0.25 mm) to get particles of uniform size, weighed and 234 g was stored in the refrigerator in a polymeric plastic bag.

3.3. Overall Experimental Procedures

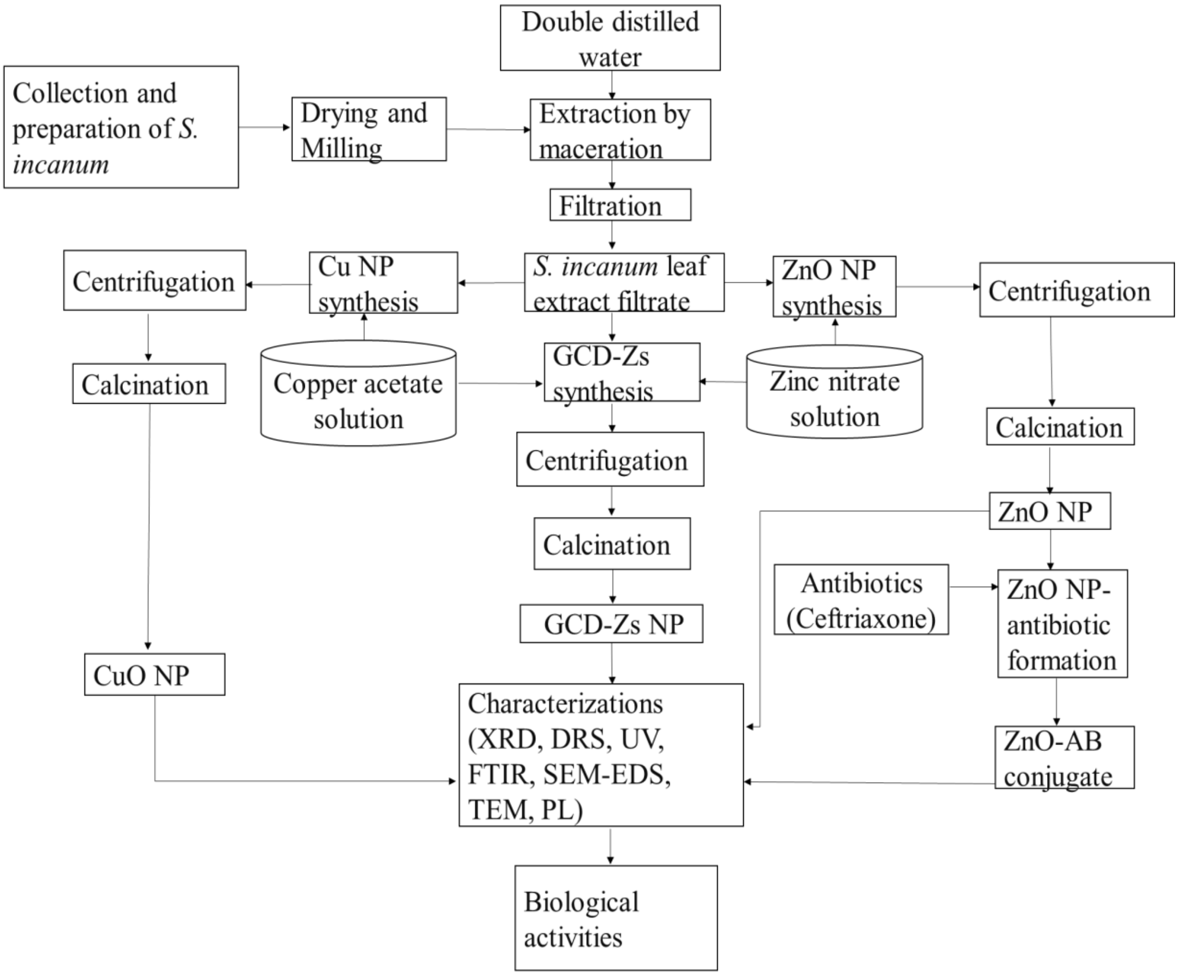

Figure 3. Flow chart for the experimental procedures of the study.

3.4. Materials and Chemicals Used

Four pathogenic bacterial strains two Gram-negative bacteria (*E. coli* and *P. aeruginosa*) and two Gram-positive bacteria (*S. aureus* and *S. pyogene*s) were obtained from the Oromia Regional Laboratory, Adama, Ethiopia. The materials used for the laboratory work were conical flasks, measuring cylinders, beakers, funnel, Petridish, test tubes, digital balance, spatula, filter paper, hot plate, pH meter, magnetic stirrer, refrigerator, incubator, muffle furnace, grinder, and centrifuge.

3.5. Preparation of the Plant Leaves Extract

The aqueous extract of the plant was prepared by cold maceration. For this purpose, 50 g of powdered plant leaf was soaked in 500 mL of distilled water, and the suspension was placed in a shaker at 20 °C for 24 h with continuous agitation at 120 rpm. The extract was filtered by Whatman filter paper No 1 and stored at 4 °C for further analysis (Hayat *et al.*, 2022).

3.6. Phytochemical Analysis

3.6.1. Test for Alkaloids

A 1 mL of the *S. incanum* extract filtrate was treated with a few drops of Wagner reagent, and observation for yellow color formation (Sbhatu and Abraha, 2020).

3.6.2. Test for Flavonoids

The plant extract was mixed with a few fragments of magnesium ribbon, and concentrated HCl was added dropwise. The evaluation for appearance of pink scarlet to indicate the presence and absence of flavonoids (Halder *et al.*, 2022).

3.6.3. Test for Phenols

A 1 mL of the plant extract filtrate was taken in a test tube, and 1 to 2 drops of ferric chlorides ($FeCl_3$) were added. The consideration of colour change of the mixture after a few minutes was followed (Hussain *et al.*, 2023).

3.6.4. Test for Saponins

The filtrate of plant extract (1 mL) was taken in a test tube and diluted with 5 mL of distilled water. It was shaken by hand for 15 minutes. A foam layer formation on the top of the test tube was evaluated (Halder *et al.*, 2022).

3.6.5. Test for Steroids

The plant extract filtrate (1 mL) was taken in a test tube and dissolved in chloroform (1 mL). Then the sides added 1 mL of acetic anhydride and 2 drops of concentrated sulfuric acid to the test tube. The upper layer in the test tube turned red was considered (Oloya *et al.*, 2022).

3.6.6. Test for Tannins

The plant extract filtrate (2 mL) was taken, and then a few drops of 10% ferric chloride solution were added to the filtrate. Then followed by evaluation of blue-green color appearance in the mixure (Hussain *et al.*, 2023).

3.6.7. Test for Terpenoids

The plant extract filtrate (1 mL) was taken in a test tube and dissolved in chloroform (1 mL). The concentrated sulfuric acid (2 drops) was added to the test tube and shaken. The observation for lower yellow color indicates the presence of terpenoids (Agidew, 2022).

3.7. Optimization of Synthesis Parameters

Aqueous solutions (0.25 M) of the precursor salts, i.e., zinc nitrate and copper acetate, were prepared. For the optimization of NP synthesis, three parameters such as volume ratio (salt solution: plant filtrate), temperature, and the pH of synthesis have been used and stirring time was for 2 h (Achamo *et al.*, 2022. Since it was considered a host metal nanoparticle, the optimization of the current study was focused on zinc. The volume ratio optimization was carried out as different volumes of plant extracts (10 and 20 mL) were added dropwise to prepare a fixed zinc nitrate salt solution (10 mL) by continuous stirring at 80 rpm for 1.5 h using a magnetic stirrer at room temperature. Also, by varying the volume of salt solution (20, 30, and 40 mL) to a fixed amount of plant extract (10 mL) and selecting the best ratio out of five for other parameters in the synthesis of nanoparticles was done and brownish nanoparticle synthesis was visually assessed. In addition, the crystal formation of nanoparticles was confirmed by periodically measuring absorbance after 30 min using a UV-visible spectrophotometer. For the temprature optimization, 2:1 volume ratio and the pH of the solution (6.8) have been constant to varying temperature (25, 50, 75, and 100 ℃). The optimal temperature (75 ℃) and volume ratio (2:1) were maintained to varied pH values (3.8, 6.8, and 9.8) for optimize pH of synthesis. Then, lastly, the optimally synthesized nanoparticle suspensions were centrifuged at 5,000 rpm for 30 min. The supernatant was discarded, and the pellet containing nanoparticles was washed three times with deionized water and ethanol (96%), then subjected to air drying in an oven and stored at a cool, dry place for further analysis after being calcined at 450^{o}C temperature (Maruthapandi *et al.*, 2020). The selected optimal conditions i.e volume ratio, pH and temperature have been used similarly to copper oxide nanoparticle synthesis.

3.8. Optimization of Nanocomposite Synthesis

To optimize the GCD-Z synthesis, we have taken the varied concentrations of copper acetate (0, 1.5, 5.5, 10.5, and 15.5%) in a 2:1 volume ratio of precursor to plant extract mixture. For this purpose, 40 mL of copper acetate and zinc nitrate mixture and 20 mL of plant extract were mixed foreach copper content. The plant extract was added to the precursors after stirring for 20 min at 25 °C then the pH of the mixtures was adjusted to 9.8 by drop-wise addition of 1M sodium hydroxide solution (Khalid *et al.*, 2021). The stirring was continued for 2 h at 75^{o}C after the pH was adjusted until the white precipitation was observed visually. The resulting colloidal solution was aged at room temperature for 24 h for more precipitation and centrifuged. The product thus obtained was washed well with ethanol and distilled water, transferred to a Petri dish, and dried in an electric oven at 45 °C for overnight. The resulting powder was subjected to calcination in the muffle furnace for 2 h at 400°C (Ibrahim *et al.*, 2022). Lastly, the XRD analysis was used to select the appropriate/best nano composition.

3.9. Green Synthesis of Nanocomposite

Based on the XRD result, the optimal composition was synthesized at 10.5% of CuO in Cu-ZnO nanocomposite. For this purpose the concentration of zinc oxide precursor was reduced to 0.22 M as 7.9 g of zinc nitrate was dissolved in 120 ml of distilled water and 0.11 g of copper acetate was added to the solution. Then 60 ml of the plant extract was added and the mixture have been adjusted to basic (pH 9.8) by dropwise adding NaOH. Then it was subjected to continuous magnetic stirring for 1.5 h at 75^{o}C until the color change was observed as a sign of the formation of the nanoparticle. Lastly, after following the same procedure as previously the CuO/ZnO nanocomposite was calcined at 450^oC based on the TGA result (Figure 4) and characterized.

3.10. Preparation of MNP-antibiotic Conjugate

The conjugate of metal oxide nanoparticles and antibiotics was prepared to evaluate the antibacterial activity of antibiotics in combination with green synthesized nanoparticles against antibiotic-resistant bacteria. Nanoparticles synthesized as in the previous section were subjected to the preparation of conjugates with a certain conventionally resistant antibiotic (Ceftaizone) (Gashe *et al.*, 2018). For the conjugation of antibiotics, 100 mg of synthesized ZnO nanoparticles were dispersed in 100 ml of distilled water and mixed with an antibiotic solution that was formed by dissolving 100 mg in 100 ml of distilled water. After stirring with a magnetic stirrer for 15 min 1 mL of 0.5M phosphate buffer solution was added to it. The reacting mixture was incubated for 24 h and then centrifuged for 15 min at 5,000 rpm. The antibiotic-conjugated nanoparticle was obtained in the form of pellets after discarding the supernatant and being washed three times with distilled water and ethanol (96%), respectively. The obtained conjugate was dried in the oven at 50 °C for 8 h. Then, a 153 mg of prepared antibiotic conjugate was subjected to UV-vis spectroscopy analysis and biological activities test (Gashe *et al.*, 2018).

3.11. Characterization of Nanoparticles

The green synthesized CuO, ZnO, and GCD-Z10.5, were subjected to characterization for the determination of temperature stability, crystalline or amorphous natures, evaluation of size and morphology, optical properties, and identification of functional groups used in the reduction of green synthesis of nanoparticles.

3.11.1. Thermo Gravimetric Analysis (TGA)

To estimate the calcination temperature of the produced material, TGA was performed using simultaneous DTA-TG equipment (DTG-60H, Shimadzu Co., Japan). In a platinum crucible on the pan of the microbalance, 7.53 mg of uncalcined ZnO nanoparticle samples were heated from 23.30^oC to 801.65^oC using Al_2O_3 as an inert material at 20 degree/min.

3.11.2. X-Ray Diffraction (XRD) analysis

To analyze and estimate the crystalline size of the synthesized nanoparticles, an X-ray diffractometer (DW-XRD-Y7000, DRAWELL, China) was used. The XRD data was recorded in terms of diffraction intensity versus 2θ from 10º to 80º and the result was plotted using Origin Pro software. The diffraction pattern also provided the information on size and shape of the unit cell from peak positions and information on electron density inside the unit cell. Also, the crystallite size was estimated using the Scherer formula (Ghaffar *et al.*, 2022).

3.11.3. Field Emission Scanning Electron Microscope (FE-SEM) analysis

Scanning electron microscopy (FE-SEM, ZEISS SIGMA VP, Germany) is used to estimate the topography, morphology, and crystallographic information of synthesized nanoparticles and it was conducted for morphological analysis of current green synthesized nanoparticles (ZnO, CuO, and CuO/ZnO). The nanoparticles were kept on a sample stub with carbon tape and the stubs were placed in the electron microscope sample chamber (Liu *et al.*, 2019). The SEM analyses of the synthesized nanoparticles were recorded at different magnifications (2.5, 5, 10, 20, and 30 KX).

3.11.4. Energy Dispersive X-ray spectroscopy (EDX) analysis

Energy-dispersive X-ray spectroscopy (EDX) was used to determine the chemical composition of the green-produced nanoparticles and nanocomposites. Energy dispersive X-ray spectroscopy (EDX) is an analytical technique used to determine the elemental analysis or chemical characterization of a sample via interaction between the sample and the X-ray excitation source. Every atom has a distinct arrangement of electrons in discrete energy levels around the nucleus while at rest. When a high-energy beam of radiation strikes a sample (matter), it may excite an electron from the inner shell, causing a hole to form. To compensate for this vacancy, electrons from the outer shell migrate to the inner shell, and the energy differential between the outer and inner shells can be generated in the form of an X-ray. Because each element has a distinct electronic configuration, when the sample is exposed to high-energy electromagnetic radiation, it emits a distinctive X-ray that acts as a fingerprint for each element. A detector can detect the number and energy of X-rays emitted by a sample.

3.11.5. Transmission electron microscopy, high-resolution transmission electron microscopy, and selected area electron diffraction (TEM-HRTEM-SAED) analysis

For the determination of particle size, morphology, and crystallinity of nanoscale-sized ZnO-GNPs and GCD-Z10.5 materials, further analysis by transmission electron microscopy, high-resolution transmission electron microscopy, and selected area electron diffraction (JEOL JEM 2100 HRTEM, JEOL, USA) analytical techniques were used.

3.11.6. UV-vis Diffuse Reflectance Spectroscopy (DRS) analysis

The optical properties of the green synthesized ZnO, and GCD-Z10.5 was analyzed by using UV-vis spectrophotometer (Carry 100 UV-Vis, Agilent Technologies, USA). The band gap energy for ZnO, and GCD-Z10.5 were calculated by using Kubelka-Munk function plots (Liu *et al.*, 2019).

3.11.7. Photo Luminescence (PL) analysis

The emission of light from the green synthesized nanoparticles was measured under optical excitation by using a photoluminescence instrument (S/N: MY18490002, Agilent Technologies, USA). For this analysis, about 5 mg of calcined ZnO, CuO, and GCD-Z10.5 nanoparticles were suspended in DMSO in separate vials and sonicated for 30 min at 75 kHz by an ultrasonic bath (sonicator). The prepared nanoparticle suspension was added to the cuvette and subjected to PL scanning and data was recorded. The obtained data were analyzed as graphs by using Origin Pro (8.5 version) software.

3.11.8. Fourier Transform Infrared Spectroscopy (FTIR) analysis

Fourier Transform Infrared Spectroscope (FTIR) (FT/IR-6600typeA, JASCO Japan) was used to detect the changes of major functional groups residual of synthesized nanoparticle samples. For this purpose, a 0.5g synthesized nanoparticles powder were mixed along with IR-grade powder and then this powder has been transferred into a sample cup of the diffuse reflectance accessory and scanned in the spectrum region (Saravanan *et al.*, 2013). The FTIR spectral data were recorded and analyzed by using Origin Pro (8.5 version) software.

3.11.9. UV-Vis Spectroscopy analysis

To measure the optical properties, synthesized nanoparticles were dispersed in dimethyl sulfoxide (DMSO). The DMSO i.e. the solvent used as reference was added to one cuvette and nanoparticles suspension was added to another cuvette. The absorption spectrum of synthesized nanoparticles was measured using a spectrophotometer in the wavelength range between 200–600 nm. The UV–Vis absorption spectra of the synthesized nanoparticles was recorded with a double-beam spectrophotometer and the result was analyzed and piloted using Origin Pro software (Singh *et al.*, 2016).

3.12. Preparation of Antibiotic-resistant Bacterial Species

Experiments of biological activities were performed on four pathogenic antibiotic-resistant bacterial strains, Gram-negative: *E. coli* (ATCC 25922) and *P. aeruginosa* (ATCC 27853); Gram-positive: *S. aureus* (ATCC 25923) and *S. pyogenes* (ATCC 13311), that were obtained from the Oromia Regional Laboratory (Adama, Ethiopia). For experiments, all stock cultured bacteria were activated on Mueller-Hinton (MH) agar plate. After activation, the cultures have been subjected to inocula development by inoculating a loop full of cells from a single colony into Mueller-Hinton (MH) broth and incubated for 24 h at 37˚C. Then the active pure bacterial cultures and sub-cultures were maintained with the turbidity of 0.5 McFarland standard ($\sim 1 \times 10^8$ colony forming unit (cfu)/mL). A 0.5 McFarland standard was prepared by combining 0.05 ml of 1 percent $BaCl_2$ and 9.95ml of 1 percent H_2SO_4 in distilled water. This process was repeated every time before starting a new experiment.

3.13. Antimicrobial Activity of Green Synthesized MNPs, Nanocomposites, and MNPs-Abs conjugate.

The antibacterial properties of the biosynthesized NPs were investigated using the standard method of Kirby–Bauer disc diffusion method (Muthuvel *et al.*, 2020). The fresh overnight culture of each strain has been swabbed uniformly over a sterilized and cooled Mueller-Hinton agar medium (MHA) dish. Then, 6 mm diameter sterile discs that impregnated with 20 µL of different green synthesized sample solutions (10, 5, and 2.5 mg/ml) and allowed to dry before being placed onto the plates and incubated for 24 h at 37^{o}C. The discs impregnated with Ciprofloxacin solution (30 µg/ml) and DMSO (10%) were used as positive and negative control, respectively. After incubation, the antimicrobial activity was determined by measuring the diameter of the zone of inhibition. The antibacterial activity was normalized and calculated in terms of percentage inhibition which iwas calculated as diameter of sample/diameter of control x 100. The same procedure was followed for the synthesized nanocomposite and antibiotic-nanoparticle conjugate. Then the corresponding zone of inhibition has been compared accordingly.

3.14. Determination of minimum inhibitory concentration (MIC)

The minimum inhibitory concentration of green synthesized nanoparticles was investigated by measuring the absorbance of bacterial growth. For this purpose, the six double dilutions of the nanoparticles suspension were prepared from 20 mg/ml to 0.625 gm/ml. The 10 ml of Mueller Hinton broth was inoculated with 0.1 ml of bacterial culture with turbidity of 0.5 McFarland standards ($\sim 1 \times 10^8$ colony forming unit (cfu)/mL)and 0.5 ml of various concentrations of prepared nanoparticles suspensions in each test tube and incubated at 37 °C for 24 h. The visual observation for the presence and absence of turbidity that indicate bacterial growth was considered. Also, the absorbance of the mixture was observed before and after the incubation for each test tube by taking a sufficient amount into a cuvette and measuring OD at 610 nm (Akbar *et al.*, 2021). During the experiment MHB without nanoparticles and bacteria used as positive control and MHA alone as negative control.The least concentration that looks clear visually and contains approximately similar or less absorbance value with the concentration earlier after incubation was taken as MIC.

3.15. Determination of minimum bactericidal concentration (MBC)

The MBC (Minimum Bactericidal Concentration) is lowest antibacterial concentration that prevents an organism's growth after subculture onto media. To determine MBC, the test tubes that contained MIC and higher concentration were considered. A 0.1 ml of a mixture of NPs, bacteria, and broth together was taken from each sample mixture and spread on the corresponding MH agar plates. The appearance of colonies on the agar plate that indicate the viability of bacteria was observed after incubation at 37^{o}C for 24 h. The smallest concentration that have no formation of bacterial colonies on the agar plate was considered as MBC. The TV (tolerance value) was determined for each sample against ARB by dividing MBC to MIC. Tolerance test was performed on all the tested NPs/NCs/conjugate against the bacterial species and tolerance values (TV) were obtained. The TV was determined for each sample by obtaining ratio of MBC to MIC.

3.16. Antioxidant activity

The antioxidant activity test was performed using the DPPH free radical scavenging assay. DPPH solution (0.1 mM) was prepared in methanol by dissolving 0.004 g DPPH in 100 ml methanol. The solution was kept in darkness for 30 min to complete the reaction. The powder of each GNPs, GNCs and conjugate were diluted in five vials 2000, 1000, 500, 250, 125 µg/ml. From this concentrations 1 ml of each were mixed with 3ml of 0.004% DPPH. Ascorbic acid was prepared with the same concentration of samples and used for comparison as positive standard in the experiment. The resulting solutions were subjected to UV-Vis spectrophotometer to record absorbance at 517 nm after keeping 30 min in dark place incubation for further reaction (Kalia *et al.*, 2021). The percentage DPPH inhibition was calculated according to the following formula,

% of radical scavenging activity = Abs of DPPH (control) - Abs of sample/Abs of DPPH (control)*100. The IC50 values were calculated by plotting DPPH percentage inhibition versus log transformed concentration of sample extract.

3.17. Data Analysis

The experimental results of antibacterial tests were expressed as mean ± standard deviation (SD) of three replicates. During the analysis, the data were subjected statistical Package of Social Science (SPSS 22.0) version was used to analyze the experiment results and the results were presented as tables. The differences between means were determined by using one-way ANOVA and least significant difference test. The level of statistical significance was set at $p \leq 0.05$. The OriginPro8 software was used to analyzes and draw graphs for all the instrumental analyses. After insertion of organised data, the line and stack lines by Y offset graph line selection was considered. For the polyhedral structure models of synthesized metal oxide nanoparticles the 3D Visualization for Electronic Structural Analysis (3D-VESTA) was used.

4. RESULTS AND DISCUSSION

4.1. Phytochemicals screening

The extract of plant leaves was subject to qualitative screening of phytochemicals, that play crucial role of reducing agents in the synthesis of nanoparticles. Thephytochemicals presented in in Table 3 are most reported from medicinal plants. However, our results showed the absence of two phytochemicals (Flavonoids and Steroids) that were indicated in a minus (-) sign and others present were indicated in (+) sign .

Table 3. Phytochemicals screening results of *S.incanum* leaves extract

Phytochemical	Existence	Description
Alkaloids	+	Yellow reddish
Flavonoids	_	No pink scarlet
Phenols	+	Bluish black
Saponins	+	About 3 cm foam
Steroids	_	No red, green
Tanins	+	Blue green
Terpenoids	+	Yellow lower layer

In the green synthesis method of metal oxide nanoparticles, various plant extracts are used as reducing and capping agents. These extracts contain a variety of phytochemicals that can act as reducing agents. Among the tested phytochemicals for their presence, five were confirmed from the expected color change based on a previous report (Sbhatu and Abraha, 2020). But in the case of flavonoids and steroids, no reaction and color formation was observed which is in agreement with previous reports and considered as absent for current study. According to our qualitative result, we assumed that the pyhtochemicals which contributed to the synthesis of metal oxide nanoparticles were those indicated by plus sign (Table 3). Some alkaloids such as caffeine, ephedrine, and quinine have been reported to show reducing properties and can be used for synthesizing AuO NPs (Lashin *et al.*, 2021). The other bioactive compounds such as phenols, saponins, tanins and terpenoids have a different functional groups including carboxylic acid (-COOH), hydroxyl (-OH), aldehyde (-CHO), nitrile (-CN), and amines ($-NH_2$) which participate in reducing the metal ions into free metals (Khan and Khan, 2023). Flavonoids such as quercetin and catechin have been reported to possess reducing properties that can be used in the synthesis of ZnO NPs, however, in the current plant species extract test flavonoids were found to be absent. We reasoned that phenols, saponins, tanins and terpenoids found in the *S. incanum* L. to take part in the reduction reactions for the fabrication of metal oxide nanoparticles and nanocomposites and are highly potent to reduce metal ions. The results were confirmed with FTIR that detected the functional group of carboxyl, hydroxyl and others at approximate band positions of 3440 and 3245 cm^{-1} on the uncalcined ZnO-GNPs (Figure 13a).

4.2. Green synthesis parameters optimization

The optimization process included three variables, precursor plant extract ratio, temperature and pH and the varied conditions are summarized in Table 1 (see Materials and Methods). The different optimization parameters were analyzed by UV-vis spectrophotometry. The results show that a 2:1 precursor plant extract ratio, temperature of 75 °C, and pH of 9.8 were obtained as optimal conditions, as shown in Figure 4. These conditions were used for the subsequent synthesis, characterization, and application tests.

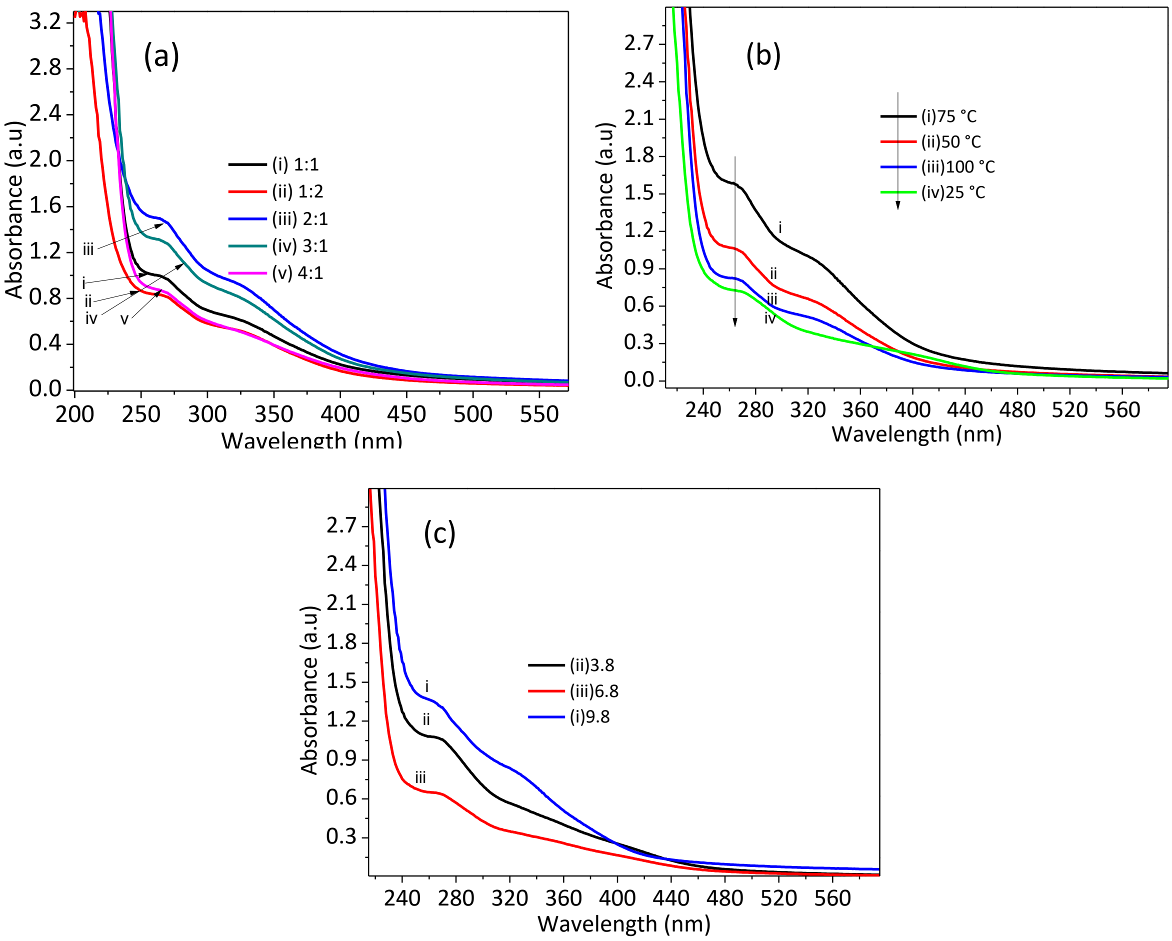

Figure 4. UV-vis spectra for the optimization of parameters during synthesis: (a) plant extract-precursor concentration ratio, (b) temperature, (c) solution pH. The 2:1 precursor plant extract ratio, temperature of 75 °C, and pH of 9.8 were obtained as optimal conditions.

The peak intensity of the absorbances in the UV graphs reflects the concentration of the materials. Therefore, the highest peak generating conditions were considered to be forming the maximum amount of nanoparticles (Figure 4 a-c) by the green synthesis method. The bioactive compounds that are found in the extract of the current plant species have reduced the zinc ions in the fabrication, and the peak intensity was observed in the wavelength range of 270–340 nm. Since the range of the peak appearance was approximately at a similar position, our attention was on the sharpness (higher absorbance) of the peaks, which indicate the formation of ZnO NPs. In a previous report with a similar approach, the optimization for copper oxide formation with the greater absorbance values confirmed the greater number MNPs formation (Achamo *et al.*, 2022). The high intensities of the peaks at 2:1 plant extract-precursor, temperature of 75 °C, and pH of 9.8 were considered as optimal conditions as there was more formation of the ZnO NPs. The optimal conditions were adopted and applied for further synthesis of other NPs and NCs.

Table 2. Synthesis parameters optimization:

Precursor: extract ratio		Temperature	pH
Precursor (mL)	extract (mL)		
10	10	25	3.8
10	20	50	6.8
***20**	**10**	***75**	***9.8**
30	10	100	
40	10		

*2:1 precursor; extract ratio, 75ºC temperature, and pH of 9.8 were obtained to be optimum

A temperature of 25°C and pH of 6.8 were used during precursor: extract ratio optimization; the optimum 2:1 precursor: extract ratio and pH of 6.8 were used during temperature optimization; the optimum 2:1 precursor: extract ratio and 75°C were used during pH optimization. The extract-precursor concentration ratio, temperature, and pH optimizations: the 2:1 precursor plant extract ratio, a temperature of 75°C, and a pH of 9.8 were obtained to be the optimal condition's value.

4.3. Thermal gravimetric analysis (TGA)

The surface energy of nanoscale-sized materials is much greater than that of their bulk counterparts , which assists in their aggregation with one another. Besides, the coalescence or aggregation of NPs is greatly assisted by temperature (Ma *et al.*, 2019). Thus, the maximum calcination temperature applied for the removal of plant organic matter after its role as a capping, reducing, and gelating agent should be optimized. Figure 5a and b shows the TGA-DTA thermal stability analysis result of the green synthesized copper-doped zinc oxide nanocomposites (GCD-Zs) and ZnO NPs plant extract organic matter respectively. The first two weight losses on the TGA curve within the temperature range of 50–300 °C are due to surface and/or interstitial absorbed water molecule removal. However, within this 50–300 °C temperature range, the decomposition of some organic substances also occurred (Doan Thi *et al.*, 2020). The respective DTA stability loss endothermic peaks due to water removal and organic substance decomposition were detected at 150 and 250 °C, respectively. The third greatest mass loss on the TGA curve detected in the temperature range of 250–420 °C (see the respective broad and intense exothermic DTA peak) is due to the total precursor and left-over organic matter decomposition to give pure metal oxide crystal. In the thermal stability analysis result of the ZnO-GNPs-plant complex, the first two weight losses within the temperature range of 50–130 °C are due to water molecule removal and decomposition of about 30% of some organic substances. The stability peaks were detected at 64 and 117 °C, respectively. The third mass loss within the 190–403 °C range is due to the total precursor and left-over organic matter decomposition to give pure metal oxide crystal (Figure 5a).

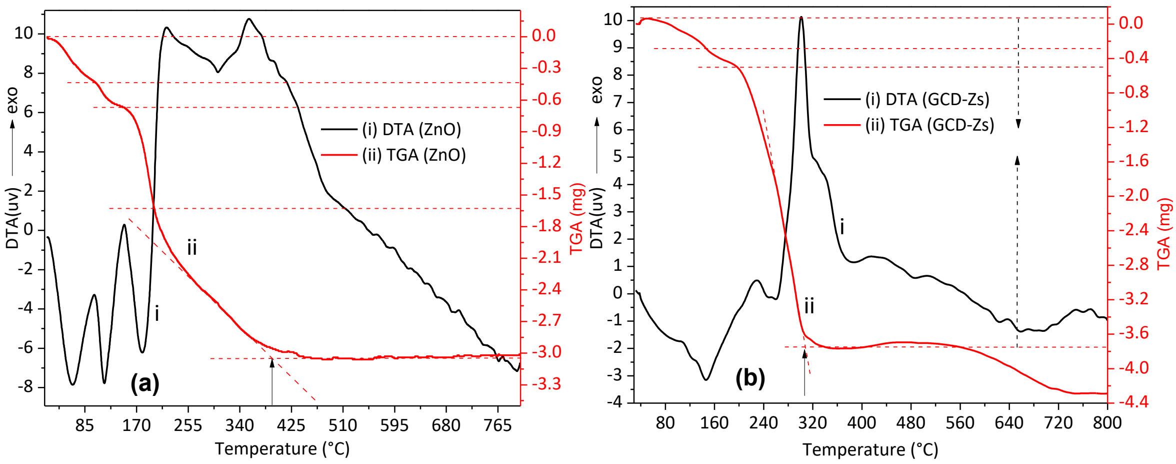

Figure 5. Thermal gravimetric analysis and differential thermal analysis (TGA-DTA) for ZnO and GCD-Z10.5 precursor-plant extract before calcination.

The GCD-Zs-plant complex has greater stability than the ZnO-GNPs-plant complex, which indicates that the copper precursor is acting as a catalyst for the degradation of the plant extract and is also increasing material crystal structure perfection (Ren *et al.*, 2015). Thus, 450 °C was selected for the next consecutive characterization and application experiments. The selected temperature is greater than the TGA optimal temperature of 403 °C (ZnO-GNPs) and 315 °C (GCD-Zs) for the purpose of decomposition of the under-capped leftover organic matter (Figure 5a and b).

4.4. X-Ray Diffraction (XRD)

The crystallinity of green synthesized powdered zinc oxide nanoparticles (ZnO-GNPs) and (GCD-Zs) was characterized by the XRD technique, as shown in Figure 6. Figure 6a shows the XRD patterns of ZnO-GNPs and GCD-Zs with different copper dopant percentages of 1.5–15.5%. The crystallinity of GCD-Zs was found to be greater than that of ZnO-GNPs, and increased with an increase in the dopant concentration. The more crystalline the material, the better its antibacterial activity as compared to its relatively amorphous equivalents (Perelshtein *et al.*, 2015). The additional peak detected at about 35.5 and 38.7 degrees was due to the occurrence of copper oxide. The intensity of the CuO-independent peak also increases as the percentage of dopant increases. It was also observed that as the dopant concentration increased, the average crystallite size also showed a slight reduction. The average crystallite sizes were calculated according to the Scherrer's equation, $(k\lambda)/(\beta\cos\theta)$ (Table 4.), where the value of the constant k is taken as 0.9, assuming that the particle has a spherical shape and the x-ray radiation wavelength λ has a value of 0.15406 nm. The information for full width at half maximum(FWHM) of the peak β and Bragg x-ray diffraction angle θ were taken from the XRD pattern analysis data (Sharma and Jha, 2017). According to the Scherrer's calculation, the GCD-Zs10.5 has a smaller size (22 nm) and a greater surface area compared to the other composites. However, the average crystallite size for ZnO-GNPs (~7 nm) was found to be much smaller than that of GCD-Zs (Table 4.).

Table 4. Crystallite sizes of green synthesized nanoparticles calculated by Scherrer's Equation from the XRD results.

NPs		Peaks (2θ)	FWHM	Crystallite size (nm)
ZnO		36.0153	1.45940	7.46
		31.7139	1.16980	7.38
		34.3985	1.50400	5.78
		Av		**6.87**
CuO		35.5475	0.25110	34.71
		38.7508	0.27640	31.84
		48.7996	0.24870	36.65
		Av		**34.4**
GCD-Z copper doppant (%)	1.5	36.2690	0.37010	23.6
		31.7878	0.37070	23.28
		34.4532	0.29130	29.83
		Av		**25.57**
	5.5	36.2525	0.40860	21.38
		31.7732	0.39370	21.92
		34.4432	0.32310	26.90
		Av		**23.4**
	10.5	36.2843	0.42540	20.53
		34.4820	0.33260	26.13
		31.7995	0.42760	20.18
		Av		**22.28**
	15.5	36.2709	0.36100	24.20
		31.7869	0.37610	22.95
		34.4611	0.29660	29.30
		Av		**25.48**

FWHM : full width at half maximum, it is the width values of XRD peaks at which the half of maximum amplitude reached.

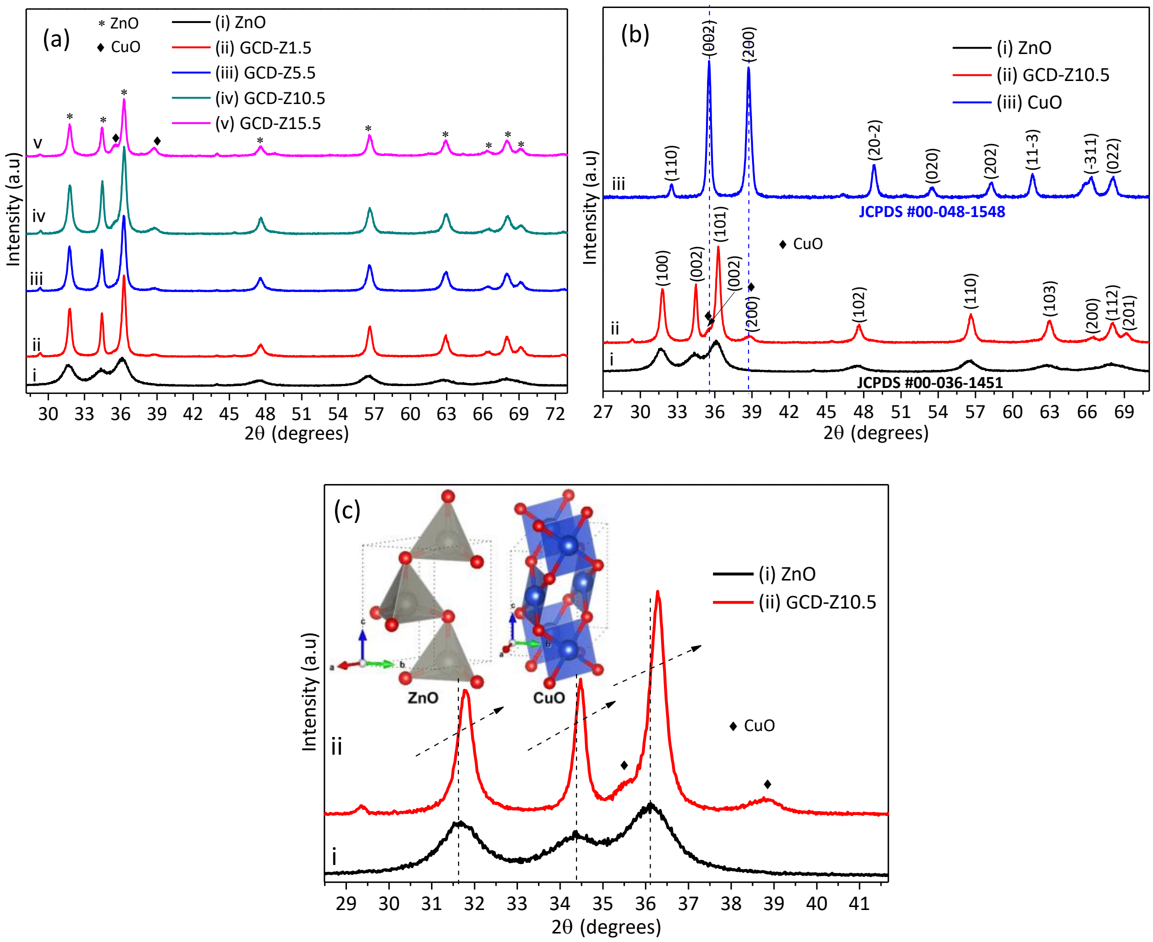

Figure 6. XRD patterns of ZnO, CuO NPs, and GCD-Zs nanocomposites: (a) XRD patterns of ZnO-GNPs and different percentages of GCD-Zs (1.5%–15.5%), in which the crystallinity increases with dopant%; (b) XRD patterns of ZnO- and CuO-GNPs and GCD-Z10.5; here, the CuO phase was detected at 35.5 and 38.7 degrees on the GCD-Z10.5; (c) magnified view of the XRD pattern for ZnO-GNPs and GCD-Z10.5.

There is a higher angle shift on the XRD pattern of GCD-Z10.5 than single ZnO, confirming the copper inclusion in the ZnO lattice. The inset in Figure 6c is the polyhedral structure models of ZnO and CuO crystals developed by the software 3D Visualisation for Electronic Structural Analysis (3D-VESTA) from the crystallographic information file (CIF) data.

Figure 6b compares the XRD patterns of single CuO- and ZnO-GNPs with GCD-Z10.5. The peaks at 2θ values of 31.8, 34.5, 36.3, 47.6, 56.7, 62.9, 66.5, 68.0, and 69.2° that have the corresponding crystal planes of (100), (002), (101), (102), (110) (103), (200), (112), and (201) match the hexagonal ZnO geometry (JCPDS 00-036-1451) (Paraguay-Delgado *et al.*, 2022). Single CuO-GNP has about nine major peaks at 2θ values with its corresponding crystal planes of 32.5 (110), 35.5 (002), 38.7 (200), 48.8 (20-2), 53.5 (020), 58.2 (202), 61.6 (11-3), 66.3 (-311), and 68.1 (022) (Zhu *et al.*, 2018) (JCPDS, File No. 00-048-1548). As shown in the XRD pattern of the GCD-Z10.5 (Figure 6b, inset label ii), the copper peaks detected at 35.5 and 38.7 degrees exactly matched the single monoclinic CuO (Costas *et al.*, 2022). In all the GNPs and GNCs, no impurity peaks other than ZnO and CuO were detected within the detection limit of the XRD instrument, which confirms the purity of the synthesis method. Figure 6c shows the magnified view of single ZnO-GNPs and GCD-Z10.5. The GCD-Z10.5 peak showed a high angle shift of 0.26 degrees, indicating the inclusion of copper in the ZnO lattice. In this study, the copper solubility level in the ZnO lattice was found to be below 5.5%, and above this level, a copper-independent peak was detected on the GCD-Zs XRD pattern. A similar copper-independent peak detection after a 4% copper dopant amount and a higher angle shift starting from 2% copper doping were also reported in the Theyvaraju *et al.* study (Theyvaraju and Muthukumaran, 2015). Even if the angle shift was detected due to slight radii differences between copper and zinc ions, no structural distortion was observed due to the exchange of copper atoms with zinc atoms. The lower solubility level of copper (only up to 5%) was also reported in another study (Morales-Mendoza and Paraguay-Delgado, 2021). The polyhedral structure models of ZnO and CuO crystals, which have the space groups of *P63mc (#186-1)* and *C2/c (#15-1)*, respectively, were created by the software 3D Visualisation for Electronic Structural Analysis (3D-VESTA) using data from the crystallographic information file (CIF).

4.5. Field Emission Scanning Electron Microscopy-energy Dispersive X-ray Spectroscopy (FESEM-EDXs)

Field emission scanning electron microscopy (FESEM) as an image analysis technique in the presence of energy dispersive X-ray spectroscopy (EDS) as a compositional analysis technique was used for the morphological and elemental composition analysis (Figures 7 and 8). ZnO-NPs have porous and/or amorphous morphology, which is created due to the evolution of gaseous byproducts as a result of combustion (Figure 7a). The combustion reaction occurred due to the heat treatment of the complexes formed between the nitrate precursor and plant extract (phytochemicals and multiple metabolite groups). Once the ignition temperature of the complexes is reached, the material starts to combust to form a porous product (Manikandan *et al.*, 2014). FESEM image analysis clearly confirmed the higher crystalline nature of the GCD-Zs compared to ZnO GNPs (Figure 8). The total change of ZnO's porous and/or amorphous morphological nature to a spherical crystalline morphology in GCD-Z10.5 is probably due to copper inclusion. This crystalline morphology for GCD-Zs and the amorphous nature of ZnO-GNPs are also consistent with the XRD result interpretation.

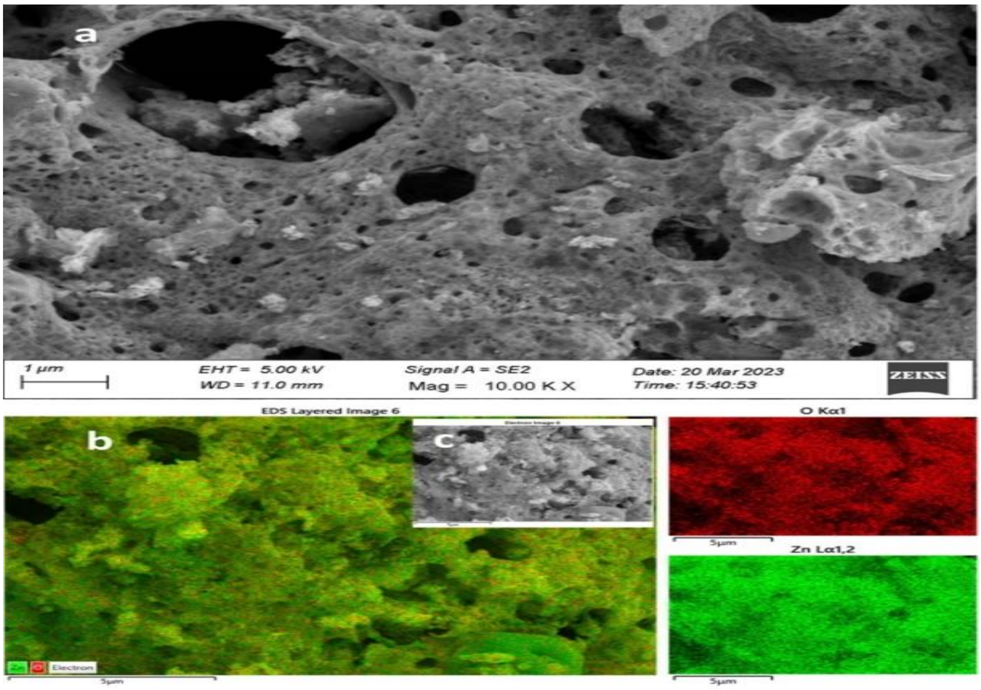

Figure 7. FESEM-EDS morphological, crystallinity, elemental composition, and elemental mapping analysis for ZnO-GNPs.

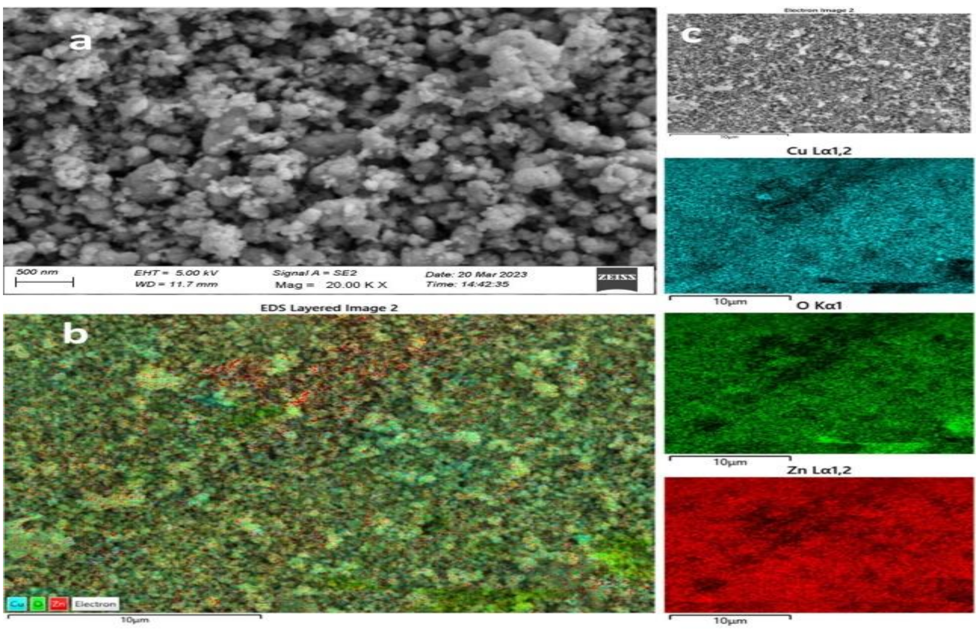

Figure 8. FESEM-EDS morphological, crystallinity, elemental composition, and elemental mapping analysis for GCD-Z10.5.

The crystalline nature of single CuO-GNPs compared to ZnO-GNPs synthesized independently following the same procedures was confirmed on the low-magnification SEM image, as shown in Appendix Figures, respectively. The accurate composition and well-doped distribution on the surface of the host material boost crucial host properties such as optoelectricity, which is crucial for antibacterial, catalysis, and several other applications (Abebe and Murthy, 2022).

The compositional analysis for ZnO-GNPs and GCD-Zs was determined by the EDX analysis, as shown in Figures 9 and 10, respectively. The EDX spectra show only zinc and oxygen for ZnO and zinc, copper, and oxygen for GCD-Z10.5, without any other impurities. The elements are observed at 1.00, 0.95, and 0.40 keV as major peaks for zinc, copper, and oxygen, respectively. The obtained amounts are fitting and in accordance with the added amount during synthesis (Figures 9 and 10 inset tables). In addition, the elemental distribution analyzed by the EDS mapping also showed the occurrence of a good dopant distribution. The EDS layered mapping images (Figures 7b and 8b) for both ZnO-GNPs and GCD-Zs were analyzed from the electron images taken at the specific surface (Figures 7c and 8c). The mapping images for zinc and oxygen are given as red and green for ZnO-GNPs, respectively. The mapping images for GCD-Zs, presented in red, green, and aqua colours, are for zinc, copper, and oxygen, respectively.

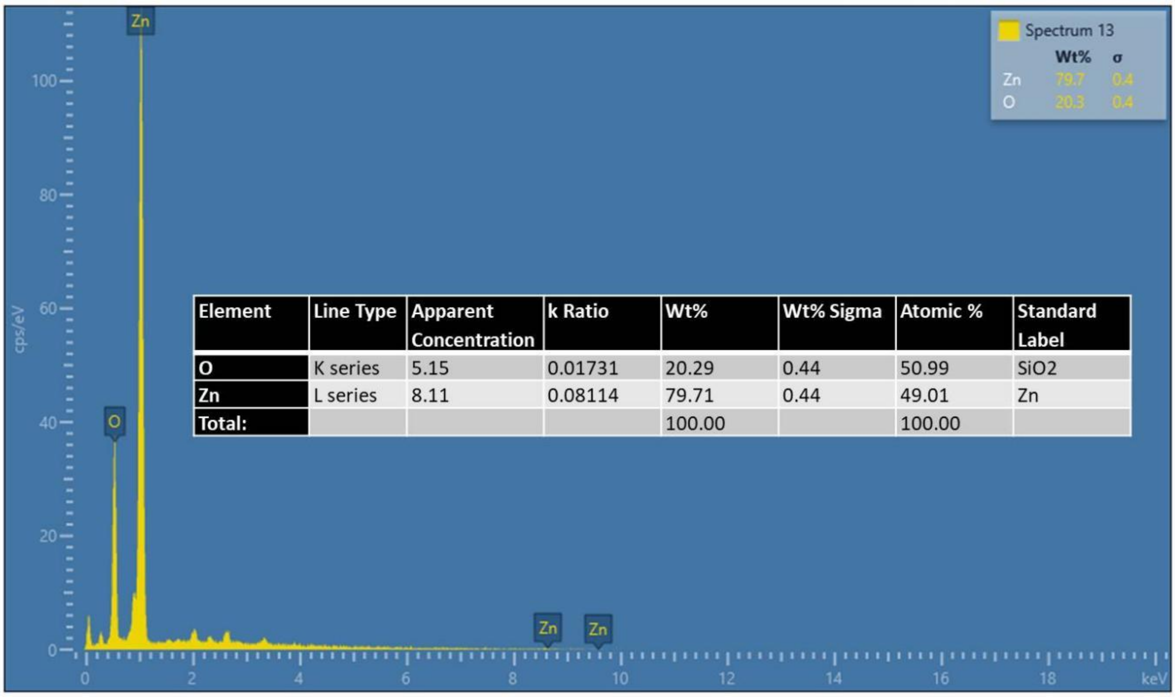

Figure 9. EDX analysis spectrum for ZnO-GNPs.

The inset table show compositional analysis table; only the expected elements of zinc and oxygen are detected without any impurities, confirming the ability of the methods to synthesize pure nanomaterial.

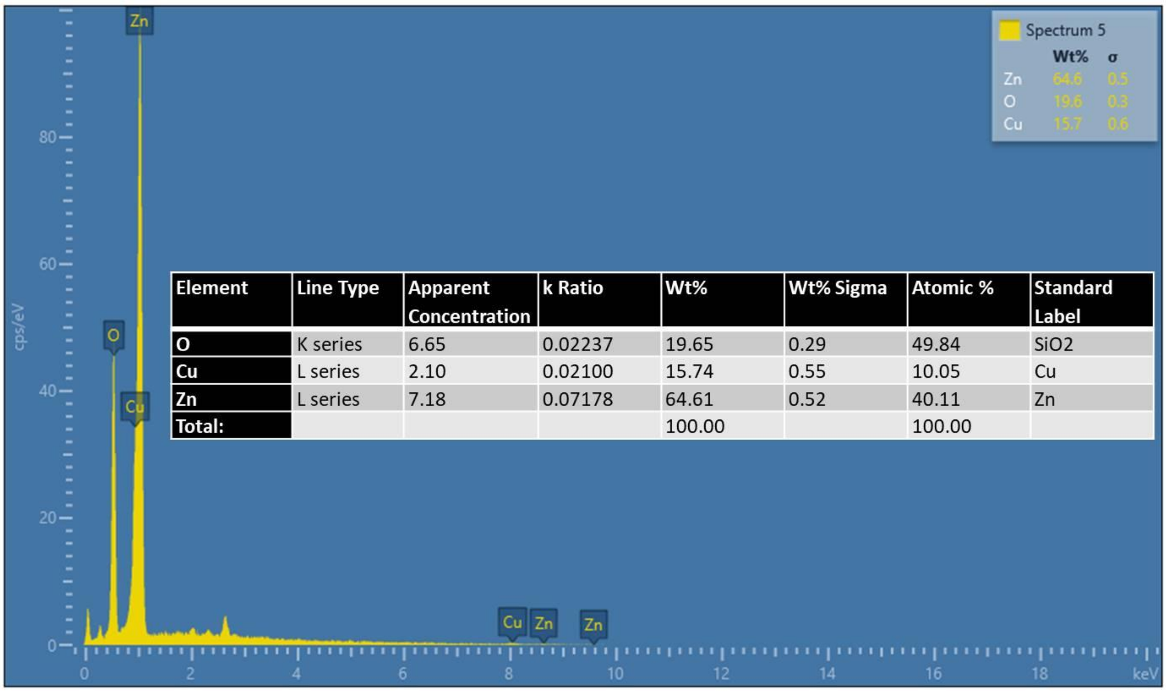

Figure 10. EDX analysis spectrum for GCD-Z10.5.

The inset table show compositional analysis table; only the expected elements of zinc, copper, and oxygen are detected without any impurities, confirming the ability of the methods to synthesize pure material. The obtained amounts were in accordance with the amounts added during synthesis. According to our EDS O is abunddant in the particles and followed by Zn, this may be due to the oxidation capacity of metals in normal condition. In relative with copper ,the is higher concentrated in the EDS result this in consistence with initial amount during synthesis.

4.6. High-resolution Transmission Electron Microscopy, and Selected Area Electron Diffraction (HRTEM-SAED)

The particle size, morphology, and crystallinity of nanoscale-sized ZnO-GNPs and GCD-Z10.5 materials were further analyzed using transmission electron microscopy, high-resolution transmission electron microscopy, and selected area electron diffraction (TEM-HRTEM-SAED) analytical techniques, as shown in Figure 11. The TEM images of ZnO-GNPs seem to have a less agglomerated, non-perfect spherical-type morphology (Figure 11a), while a relatively greater agglomerated mixture of spherical and cylindrical shapes is seen for the GCD-Z10.5 (Figure 11b). The particle sizes for ZnO-GNPs and GCD-Z10.5 were in the range of 5–20 nm and 20–40 nm, respectively, which is consistent with the XRD pattern analysis. The d-spacing value for the ZnO-GNPs crystal is 0.275 nm (Figure 11c, inset image), which corresponds to the ZnO-GNPs (002) crystallographic plane. The HRTEM image for GCD-Z10.5 confirmed the presence of 0.268 and 0.212 nm lattice fringe values (Figure 11d, inset image), which are also matching with the (002) and (200) crystal planes of ZnO- and CuO-GNPs, respectively (Abebe *et al.*, 2023; Park *et al.*, 2012). There is a slight ZnO crystallographic plane lattice fringe value difference between single ZnO-GNPs and GCD-Z10.5 that is probably due to the effect of copper inclusion in the ZnO lattice as a dopant, leading to slight distortion (Majeed Khan *et al.*, 2020; Kazmi *et al.*, 2021). The HRTEM image also confirmed the more crystalline nature of the GCD-Z10.5 crystal than that of ZnO, which is also clearly observed as shown in the SAED ring analysis (Figures 11e and f) respectively. The XRD pattern analysis results of ZnO-GNPs and GCD-Z10.5 were also depicted in the respective ZnO-GNPs and GCD-Z10.5 SAED rings as insets for comparison.

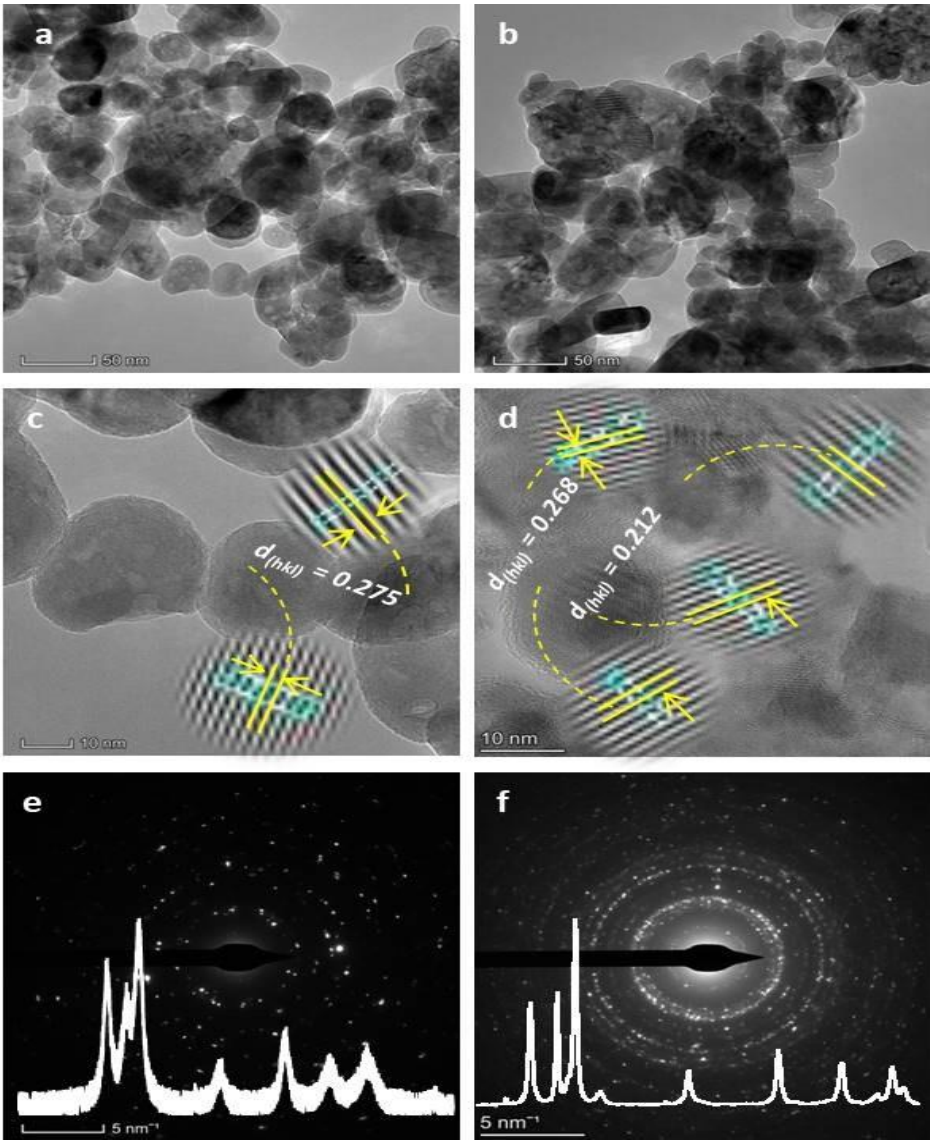

Figure 11. TEM/HRTEM/SAED morphological, particle size, and crystallinity analysis for ZnO-GNPs and GCD-Z10.5: (a) ZnO-GNPs TEM image, (b) GCD-Z10.5 TEM image, (c) ZnO-GNPs HRETM images, (d) GCD-Z10.5 HRETM images, (e) ZnO-GNPs SAED images, (f) GCD-Z10.5 SAED images.

4.7. UV–vis diffuse reflectance spectroscopy (DRS)

Doping and heterojunction are crucial strategies used for tuning the properties of host materials, which are also beneficial for several applications such as antibacterial activity, sensors, and catalysis (Abebe and Murthy, 2022). The optical property of ZnO-GNPs was tuned by copper doping and forming a CuO-ZnO heterojunction, as analyzed by DRS-UV-vis spectra analysis and shown in Figures 12a and b. The percentage reflection vs. wavelength plots of the DRS-UV-vis analysis showed greater light absorption properties for

GCD-Z10.5 than ZnO-GNPs (Figure 12a). The reflection observed within the wavelength range of 370–410 nm may be attributed to the conduction band-to-valence band electron-hole recombination characteristics of ZnO-GNPs (Liu *et al.*, 2019). The greater absorption properties of the GCD-Z10.5 are a result of the shallow level *d-d* transition created within ZnO-GNP's energy gap after copper inclusion. The shallow level creation is further confirmed by the Kubelka-Munk (K-M) function plots, which were shown by interpolation of the linear plots towards the x-axis. The direct electron transition occurred when photon-induced electron-hole recombination occurred without relaxation. Conversely, in the indirect electron transition, electrons have a relaxation time before recombination. The crystal momentum, *k factors*, for a direct transition is zero, unlike the indirect transition, which has a non-zero value (Theyvaraju and Muthukumaran, 2015). Electron relaxation and transition from the host conduction band to the shallow level or CuO crystal have great importance for ROS generation, which has important properties for bactericidal activities (Abebe *et al.*, 2020). The direct bandgap values for ZnO-GNPs and GCD-Z10.5 are 3.23 and 3.04 eV, respectively (Figure 12b, inset labels i and ii). The indirect bandgap values for ZnO-GNPs and GCD-Z10.5 are 3.13 and 2.97 eV, respectively (Figure 12b, inset labels iii and iv). The red shift on both the direct and indirect bandgaps for GCD-Z10.5, compared to ZnO-GNPs, confirms the inclusion of copper in the ZnO lattice and visible light absorption enhancement (Thabit *et al.*, 2022).

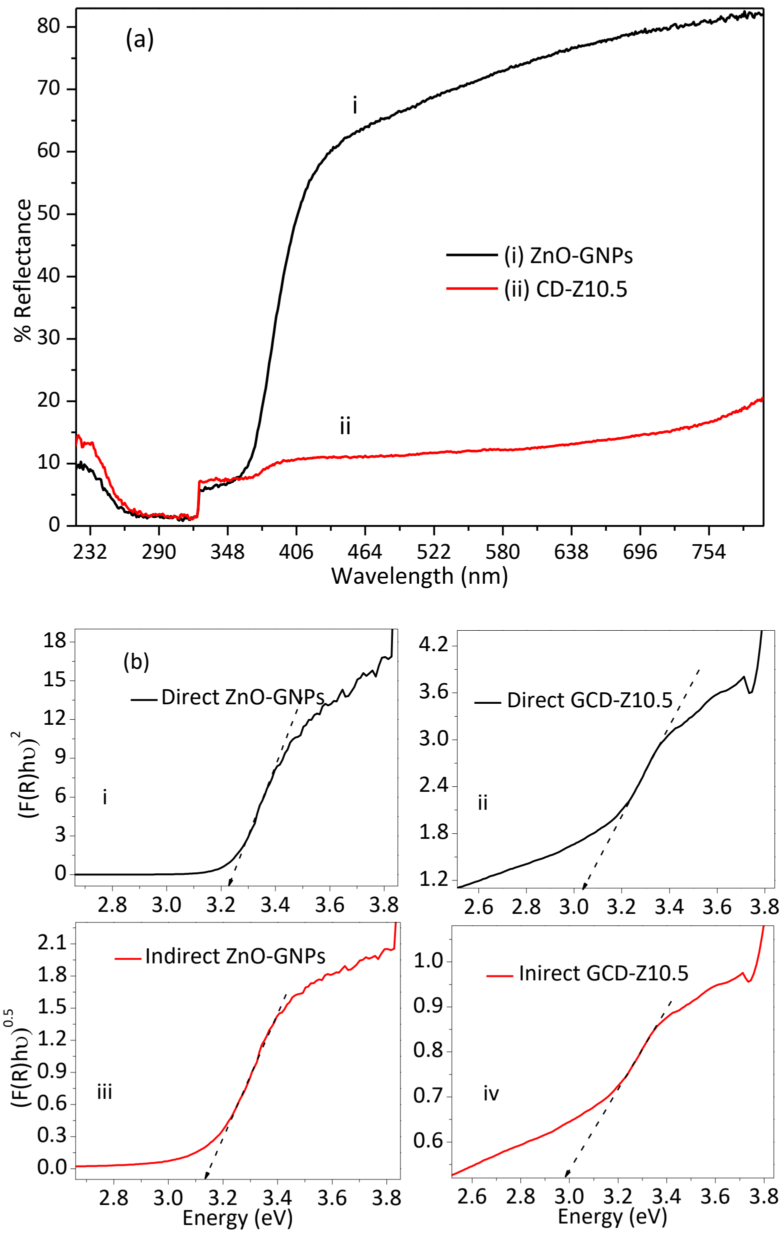

Figure 12. Optical properties study using the DRS-UV-vis spectroscopic technique (a) and Kubelka-Munk function (b) analysis:

In the graph (Figure 12. a) %reflectance versus wavelength plot of ZnO-GNPs and GCD-Z10.5 NCs, with greater light harvesting behaviour for the GCD-Z10.5 NCs. The Kubelka-Munk function plots(Figure 12. b): (inset labels i and ii) the direct and (inset labels iii and iv) the indirect Kubelka-Munk plots for ZnO-GNPs and GCD-Z10.5 NCs, respectively. Redshift for both direct and indirect GCD-Z10.5 plots confirms the inclusion of copper in the ZnO lattice of GCD-Z10.5.

4.8. Photo-luminescence (PL) spectroscopy

The optical properties of CuO, ZnO and GCD-Z10.5 materials were further confirmed using photoluminescence (PL) spectroscopy, as shown in Figure 13. ZnO-GNPs have two broad peaks at 367 and 465 nm and one intense band at about 403 nm, respectively. The peak detected at 403 nm is a characteristic near-band edge (NBE) transition in ZnO-GNPs that occurred due to free exciton electron-hole recombination (Singh *et al.*, 2020). The green emission that occurred at about 465 nm is probably due to intrinsic defects (oxygen vacancies) (Ma *et al.*, 2019). The CuO-GNPs also has two short and broad emission peaks at 369 and 473 nm and one relatively intense and broad peak at 409 nm, respectively. These CuO emission peaks occurred as a result of the ultraviolet, green, and violet emissions, respectively. The GCD-Z10.5 also showed one ultraviolet and two visible bands at 370, 406, and 470 nm. The two broad peaks on the GCD-Z10.5 showed an emission intensity rise and a slight shift due to the combined effects of copper. The green emission is attributed to the electron transition from the dopant shallow level to the host valence band after relaxation (Singh *et al.*, 2020). All the emissions detected on the copper oxide spectrum were also detected on GCD-Z10.5, which indicates the presence of copper crystals as a local contact (heterojunction) with ZnO-GNPs. This has importance in improving the charge transfer properties and consequently enhancing the generation of ROS species through electron and hole reactions with oxygen and water, respectively.

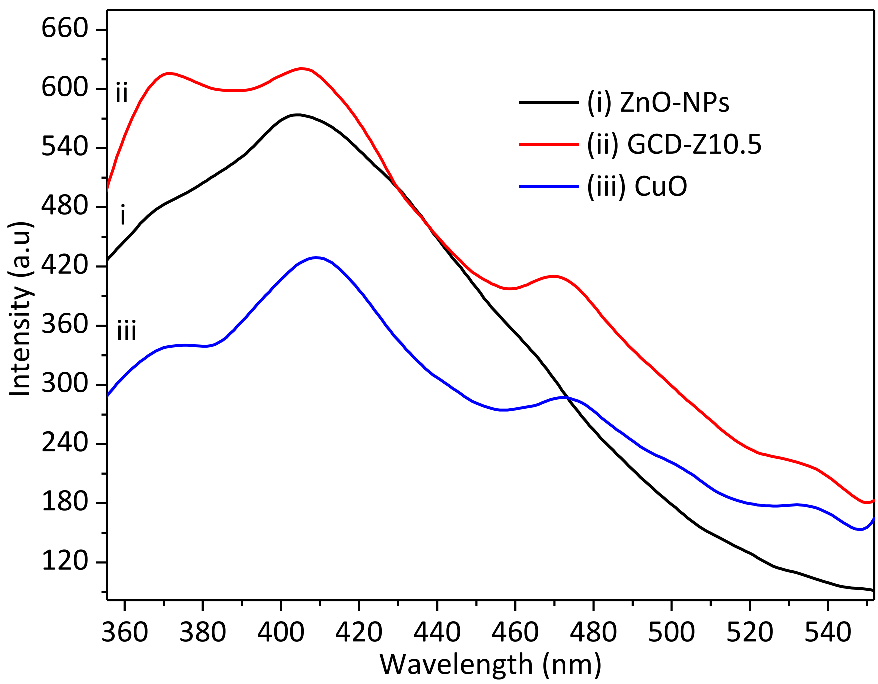

Figure 13. Optical analysis for CuO-GNPs and ZnO-GNPs and GCD-Z10.5 NCs by photoluminescence spectroscopic technique:

The single ZnO-GNPs showed a characteristic emission peak at 403 nm. Copper has three emission peaks attributed to defects: violet and green emissions. The copper emission peaks were also detected on the composite spectra, indicating the presence of CuO-ZnO local contact within the composites.

4.9. Fourier-Transform Infrared Spectroscopy (FTIR)

The functional groups and purity of the GNPs and GNCs were analyzed by Fourier-transform infrared (FTIR) spectroscopy. Figure 14a shows the FTIR spectra of ZnO-GNPs before and after calcination, and CuO-GNPs and GCD-Z10.5 NCs after calcination. The distinctive signal detected at the approximate band positions of 3440 and 3245 cm^{-1} on the uncalcined ZnO-GNPs is attributed to the plant extract alkyne C-H stretching, carboxylic acid, and phenol O-H stretching from the hemicellulose, cellulose, and lignin groups (Lashin *et al.*, 2021; AL-Shehri *et al.*, 2022). The two sharp but short bands detected at about 2360 and 2330 cm^{-1} are attributed to carbon dioxide absorption. The other new peak at 1360 cm^{-1} for uncalcined ZnO-GNPs is the result of a symmetric or asymmetric stretching vibration of C=O (Ali *et al.*, 2022). The peaks at 890 and 625 cm^{-1} are probably due to the bending vibration of other organic residues left over (Doan Thi *et al.*, 2020). However, the broad peak detected at 3370 and 1640 cm^{-1} on the calcined ZnO-GNPs are due to O-H stretching and bending vibration of the surface or interstitial adsorbed water molecules, respectively (Theyvaraju and Muthukumaran, 2015). The effect of copper doping resulted in a peak intensity reduction compared to a single ZnO peak, with the occurrence of copper bands on the GCD-Z10.5 NCs spectrum. These bending vibration peaks for GCD-Z10.5 resemble those of the copper spectrum with shifts after copper inclusion compared to ZnO, which is caused by copper inclusion. Our concern is that the fingerprint region (400–500 cm^{-1}) shows the presence of metal-oxygen bonds (Cu-, Zn-)O. Figure 14b shows the magnified view of the lower wave number FTIR spectrum, in which 450 and 430 cm^{-1} for Zn-O bending vibration; 440 and 415 cm^{-1} for the GCD-Z10.5; and 440 and 405 cm^{-1} for CuO (Theyvaraju and Muthukumaran, 2015).

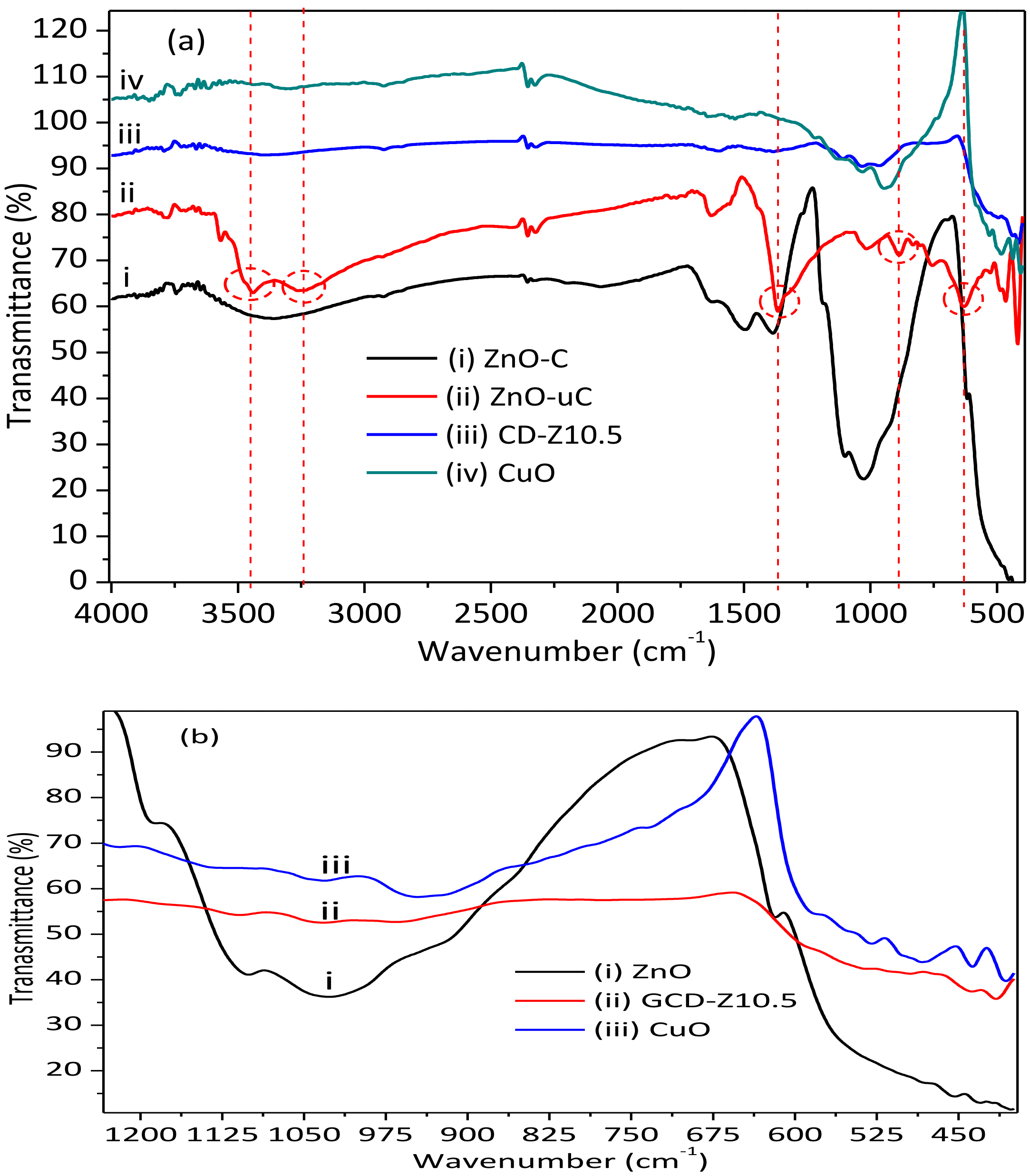

Figure 14. Chemical bonding, covalent stability analysis by FTIR spectroscopic technique: (a) FTIR spectra of ZnO before and after calcination; (b) magnified view of calcined ZnO, GCD-Z10.5, and CuO.

4.10. UV-vis Spectroscopy

The Uv result shown in the figure below at the wavelength range 270-295 nm, peak of CuO was appeared on the graph of GCD-Z10.5. This peak appearance determine the inclusion of CuO in the ZnO as it was confirmed by XRD. The peak of Zinc was also detected in conistence with previous reports (Abdelbaky *et al.*, 2022; Sorbiun *et al.*, 2018) that green synthesized ZnO spectrum at 370 nm. In addition to the other characterization the UV spectrum of GCD-Z10.5 was shown that Cu dopant in the ZnO.

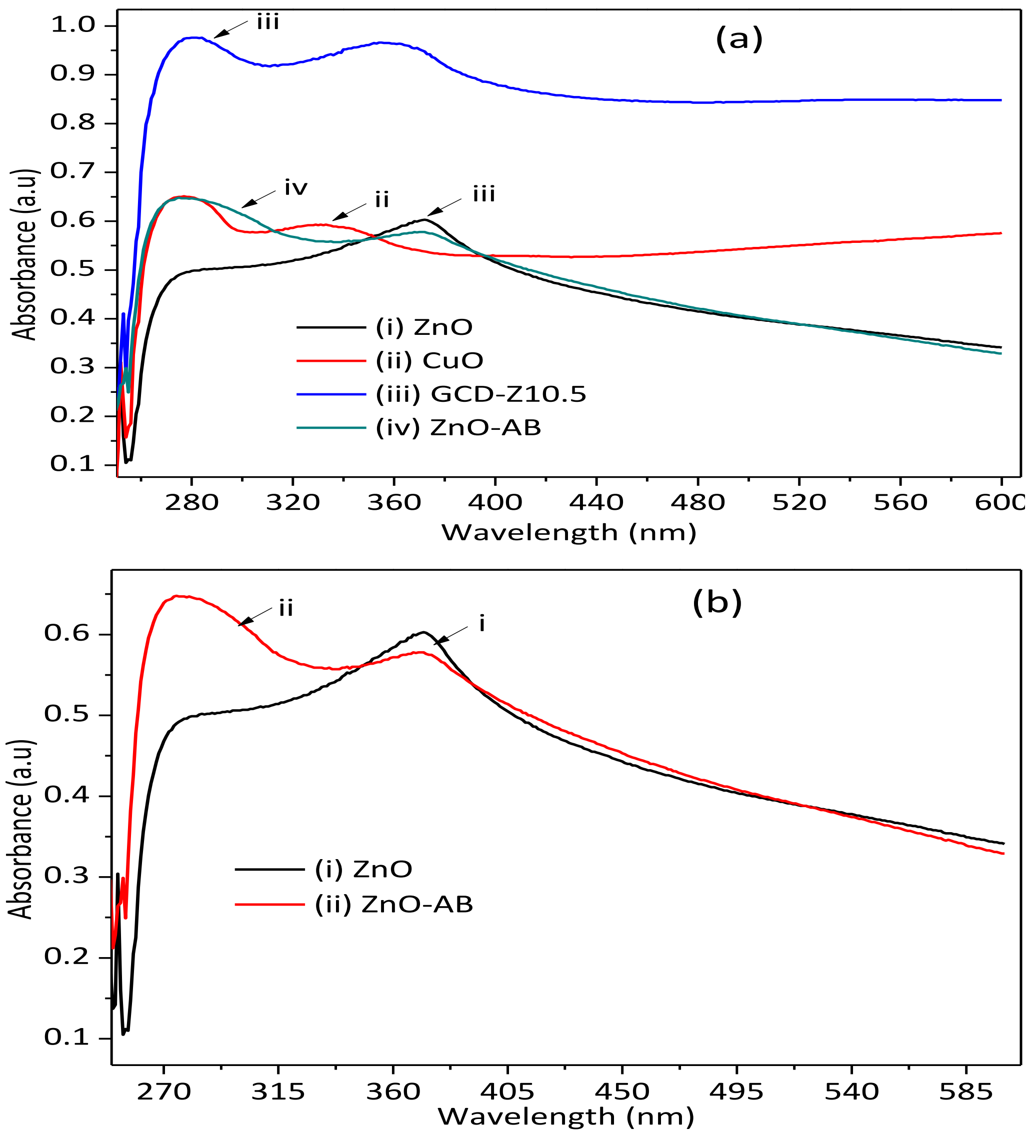

Figure 15. Graphical representation of Uv-vis spectroscopy spectrum of ZnO, CuO, GCD-Z10.5, and ZnO-AB (a) and comparison of the graph of ZnO and ZnO-AB (b).

Figure 15a, the different peak of the synthesized NPs, NC, and conjugate that shown the both peak of ceftriaxone and zinc oxide. Figure 15b, the comparison of the graph peak of ZnO and ZnO-AB that indicate the presence of ceftriaxone in the conjugation graph confirm early reported peak (Akbar *et al.*, 2021).

The conjugation of antibiotics with nanoparticles have crucial role in enhancement of various biological activities such as antibacterial and antioxidant (Akbar *et al.*, 2021). In our study the conjugation of ceftriaxone with ZnO-NPs was concerned as the graph (Figure 15 inset iii). The formation of conjugate with ZnO was determined by the spectrum peak of ceftriaxone at wavelength range 240-280 nm on the graph of ZnO-Ceftriaxone. The peak shift (sharpness) on ZnO-AB that not observed on ZnO at 275 nm was due to the conjugated ceftriaxone. This result was really confirmed with the report for the conjugation of ceftriaxone with Zinc for enhancement of antibacterial activities.

4.11. Antibacterial activities of green synthesized NPs, NC, and conjugate

The antibacterial activity of all GNPs, GNCs, and conjugate was examined using the disc diffusion method and different bacterial strains that included two gram-positive (*S. aureus* and *S. pyogenes*) and two gram-negative (*E. coli* and *P. aeruginosa*) at different concentrations of GNPs/GNCs/ZnO-AB (2.5, 5, and 10 mg/mL). Ciprofloxacin (30 µg/mL) and DMSO (10%) were used as a positive control (PC) and negative control (NC), respectively. The results are shown in Table 5 and Figure 16 for all tests. In general, all the GNPs, GNCs, and conjugate showed antibacterial activity against both the gram-positive and gram-negative bacterial strains tested with dose-dependency manner in the following order: ZnO-GNP<CuO-GNP<GCD-Z10.5. Also, the ZnO-antibiotic conjugate showed slightly less antibacterial activity than GCD-Z10.5 composite and higher activity than GNPs alone. The measurable zone of inhibition (MZI) values for ZnO-GNPs varied from 7.2 ± 0.58 mm- 10 ± 0.58 mm, PC: 25.0 ± 1.00 mm *E. coli*, 6.1± 0.33 mm-8.1± 0.33 mm, PC: 23.3± 0.58 mm *P.aeruginosa*, 9.5±0.58 mm-12± 0.58 mm, PC: 27.7±1.20 mm *S. aureus*, 6.9±0.33 mm-13.3±0.58 mm, PC: 39.3±0.88 mm *S. pyogenes*, CuO-GNPs 6.9 ± 0.33 mm–11.7 ± 0.33 mm, PC: 26.9 ± 0.33 mm *E. coli*, 6.1±0.33 mm-8.1±0.33 mm, PC: 22.1±0.33 mm *P. aeruginosa*, 7.1±0.58 mm-12.7±0.33 mm, PC: 25.7±0.33 mm *S. aureus*, 6.2±0.33 mm-12.3±0.33 mm, PC: 25.8±0.33 mm *S. pyogenes*, GCD-Z10.5 7.0±0.88 mm-15.7±0.33mm, PC: 28.6±0.57 mm *E. coli*, 6.4±0.33 mm-13.3±0.33 mm, PC: 17.7±0.33 mm *P. aeruginosa*, 6.7±0.58 mm-16.3±0.58 mm, PC: 20.5±0.58 mm *S. aureus*, 9.9±0.58 mm-16.7±0.33 mm, PC: 22.2±1.20 mm,, ZnO-AB 6.4 ± 0.67 mm–14.3± 0.33 mm, PC: 27.2 ± 0.58 mm *E. coli*, 6.5±0.88 mm-13.7±0.33 mm, PC: 18.3±0.33 mm *P.aeruginosa*, 6.3±0.88 mm-14.3±0.67 mm, PC: 22.1±0.33 mm *S. aureus*, 8.8±0.33 mm-15.3±0.88 mm, PC: 21.3±0.88 mm *S. pyogenes* respectively for the different strains with significance value of less than 0.05.

The control normalized percent inhibition for ZnO-GNP was found to be 17.5–44.5%, CuO-GNP 18.8–49.5%, ZnO-AB 23.4-71.5%, and GCD-Z10.5 24.5–79.5%, respectively (Table 5). The ZnO-GNP caused an observable inhibitory effect against the tested pathogenic bacterial strains, which may be due to the interaction between the negatively charged membrane of the bacteria and the positively charged ions of ZnO-GNP (Sánchez-López *et al.*, 2020). The size of the synthesized ZnO-GNP is very small (7 nm), which is appropriate to penetrate the membrane of bacteria and cause unicellular damage to the bacteria (Tamayo et al., 2014). These GNPs could also disturb biological processes and cause damage to the DNA, as previously reported (Xie *et al.*, 2011). In support of this result, it is also confirmed by the PL and DRS results (Figure 13 and Figure 12, respectively), which show high surface defects that indicate roughness, which can generate ROS and cause damage to the bacteria's cells (Gupta and Bahadur, 2018). It was also observed that CuO NPs show significant toxicity to the bacterial strains. According to a previous report, CuO NPs have the potential to penetrate the cells of microorganisms as well as accumulate in the cell (Abbas *et al.*, 2022). Since copper has a high affinity to fix oxygen, it generates ROS that cause cell damage (Abbas *et al.*, 2022). Doping of ZnO and CuO NPs has been shown to impart a synergy effect and improve the antibacterial property (Gupta and Bahadur, 2018). We also observed a significant enhancement of antibacterial activity by GCD-Z10.5 compared to ZnO and CuO NPs alone. The ceftriaxone-conjugated ZnO was observed to have a high antibacterial effect against the bacteria tested. This is due to the synergistic effect of different functional groups in ceftriaxone, such as hydroxyl and carboxyl groups, that might assist in the generation of ROS and cause cell damage in bacteria (Sanganabhatla and Sunder, 2019).

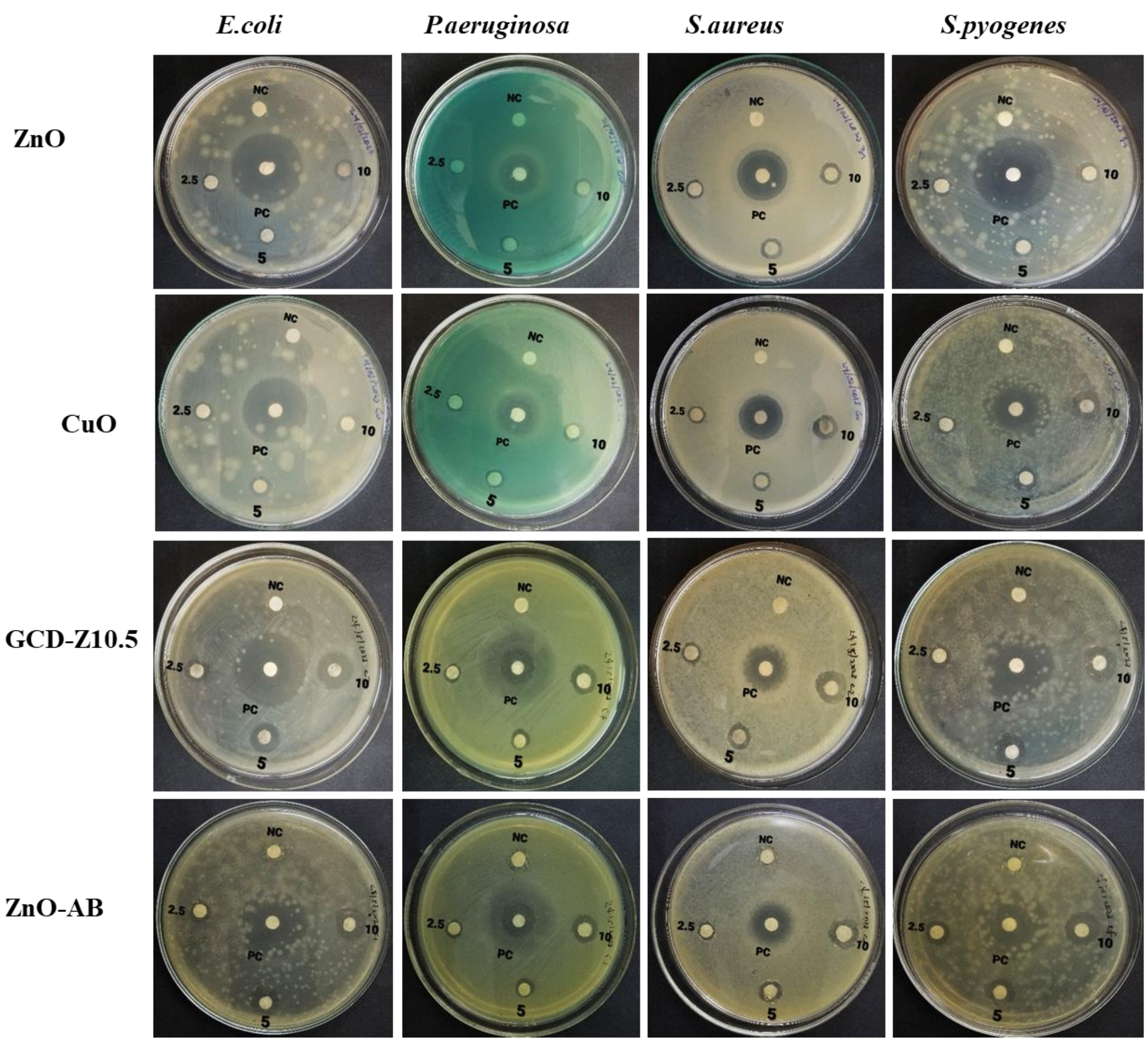

Figure 16. Zone of inhibition of ZnO, CuO, GCD-Z10.5, and ZnO-AB agianst two gram-positive (*E. coli* and *P. aeruginosa*) and two gram-positive (*S. aureus* and *S. pyogenes*).

The inhibition of growth of bacteria was observed around the discs and measured. The numbers on the plates indicate concentration of respective samples (2.5, 5 and 10 mg/mL), NC is negative control and PC is positive control. GNCs (GCD-Z10.5), and conjugate (ZnO-AB) showed higher activity, which is plausibly due to the synergistic effect of zinc with copper and ceftriaxone. All experiments were done in triplicates.

Among the bacterial strains tested, all the GNPs, GNCs, and conjugate showed slightly higher activity against gram-positive bacteria (*S. aureus* and *S. pyogenes*) compared to gram-negative bacteria (*E. coli* and *P. aeruginosa*). This may be attributed to the difference in cell wall composition. The gram-positive bacterial cell is composed of teichoic acids that partially imparts a negative charge to the cell surface and facilitate passage of metal ions, and thereby plausibly rupture the cells resulting in higher antibacterial activity of GNPs and GNCs. Also nanoparticles with reduced band gap have high free electron on the surface of particles that have high probable to interact with bacterial cell and can be toxic (ref Pharm Micro book). Both the gram-positive strains, *S. aureus* and *S. pyogenes* showed 79.5 and 75.2% inhibition (higher susceptibility) at the highest concentration tested (10 mg/mL). On the other hand, the cell wall composition of gram-negative bacteria is complex and consists of a second membrane that restricts the penetration of molecules and thereby plausibly imparts resistance to antibacterial agents.

Among the two gram-negative strains tested, *P. aeruginosa* was found to be less susceptible to ZnO and CuO compared to *E. coli*. *P. aeruginosa* has been categorized as a multidrug-resistant strain, which may explain this resistance against the GNPs and GNCs(Govindasamy *et al.*, 2021). However, it is interesting to note that both strains showed enhanced susceptibility (75.1 and 54.8% inhibition) against GCD-Z10.5 at the concentration of 10 mg/mL, up from 34.5% (ZnO, *P. aeruginosa)* and 40% (ZnO, *E. Coli*), respectively. The increased potency of GCD-Z10.5 compared to single GNPs may be plausibly due to the synergistic effect of ZnO and CuO GNPs. Furthermore, the ZnO-cef conjugate showed more inhibition than ZnO alone. This indicates that the higher inhibition of the conjugate may plausibly be due to the synergy effect. It is interesting to note that ZnO-cef showed comparable potency by generating comparable inhibition with GCD-Z10.5, 52.6% (*E.coli*) and 64.6% (*P. aeruginosa*) against the strains at the concentration of 10 mg/ml (Table 5). Therefore, both the GNCs and conjugate can be regarded as potential antimicrobials.

Table 5. Antibacterial activity (zone of inhibition) of ZnO, CuO, GCD-Z10.5, and ZnO – AB conjugate determined by disc diffusion assay.

	Measurable zone of inhibition (MZI) of ZnO (mm)							
Concentration (mg/mL)	*E. coli*	%RI	*P. aeruginosa*	%RI	*S. aureus*	%RI	*S. pyogenes*	%RI
10	10 ± 0.58	40	8.1 ± 0.33	34.5	12 ± 0.58	43.3	13.3 ± 0.58	34.7
5	7.9 ±0.58	31.5	7.2 ± 0.33	30.8	11.1± 0.33	40.1	9.2 ± 0.58	33.5
2.5	7.2 ± 0.88	28.6	6.1 ± 0.33	26.2	9.5 ± 0.58	34.6	6.9 ± 0.33	27.5
NC	6 ± 0.00	24.0	6 ± 0.00	25.7	6 ± 0.00	21.6	6 ± 0.00	15.3
PC	25 ± 1.00	100	23.3 ± 0.58	100	27.7± 1.20	100	39.3 ± 0.88	100
	Measurable zone of inhibition (MZI) of CuO (mm)							
Concentration (mg/mL)	*E. coli*	%RI	*P. aeruginosa*	%RI	*S. aureus*	%RI	*S. pyogenes*	%RI
10	11.7 ±0.33	43.5	8.1 ± 0.33	36.7	12.7± 0.33	49.5	12.3 ± 0.33	47.5
5	9.3 ±0.33	34.5	7.5 ± 0.33	34.0	8.1 ± 0.88	31.2	8.2 ± 0.58	31.5
2.5	6.9 ±0.33	25.8	6.1± 0.33	27.7	7.1 ± 0.58	27.6	6.2 ± 0.33	23.7
NC	6 ± 0.00	23.3	6.0 ± 0.00	27.1	6.0 ± 0.00	23.3	6.0 ± 0.00	23.3
PC	26.9 ±0.33	100	22.1 ± 0.33	100	25.7± 0.33	100	25.8 ± 0.33	100
	Measurable zone of inhibition (MZI) of GCD-Z10.5 (mm)							
Concentration (mg/mL)	*E. coli*	%RI	*P. aeruginosa*	%RI	*S. aureus*	%RI	*S. pyogenes*	%RI
10	15.7± 0.33	54.8	13.3 ±0.33	75.1	16.3± 0.58	79.5	16.7 ± 0.33	75.2
5	12.2± 0.58	42.5	7.5 ±0.58	42.1	11.2± 0.33	54.7	14.0 ±0.88	63.1
2.5	7.0±0.88	24.5	6.4 ± 0.33	36.2	6.7 ± 0.58	32.6	9.9 ± 0.58	44.6
NC	6.00± 0.00	20.9	6.00 ± 0.00	33.9	6.0 ± 0.00	29.3	6.0 ± 0.00	27.0
PC	28.6±0.57	100	17.7 ± 0.33	100	20.5 ±0.58	100	22.2 ± 1.20	100
	Measurable zone of inhibition (MZI) of ZnO-AB (mm)							
Concentration (mg/mL)	*E. coli*	%RI	*P. aeruginosa*	%RI	*S. aureus*	%RI	*S. pyogenes*	%RI
10	14.3± 0.33	52.6	13.7 ± 0.33	64.6	14.3± 0.67	64.8	15.3± 0.88	71.5
5	13.5± 0.33	49.6	7.9 ± 0.33	43.3	10.8± 0.56	48.8	11.3 ± 0.88	52.8
2.5	6.4 ± 0.67	23.4	6.5 ± 0.88	35.4	6.3 ± 0.88	28.5	8.8 ± 0.33	40.2
NC	6 ± 0.00	22.1	6 ± 0.00	32.8	6 ± 0.00	27.8	6 ± 0.00	28.2
PC	27.2± 0.58	100	18.3 ± 0.33	100	22.1± 0.33	100	21.3 ± 0.88	100

%RI:Percent of relative inhibition, PC: Positive control, NC : Negative control; Zone of inhibition was expressed in Mean± Standard deviation.

4.12. Minimum Inhibition Concentration (MIC) and Minimum Bactericidal Concentration (MBC) analysis

The determination of the minimum inhibitory concentration (MIC) and minimum bactericidal concentration (MBC) is crucial to consider the cytotoxicity of GNP's, GNCs, and conjugate (Applerot *et al.*, 2012). The MIC is the lowest concentration of a substance needed to prevent the visible growth of a bacterium, while the MBC is the lowest concentration required to kill the bacterium. Thus, the smallest concentration value indicates the material's effectiveness at low concentrations. A tolerance test provides information about the potency of the test materials; higher values indicate bacteriostatic action, while lower values indicate bactericidal action. Table 6. show the MIC, MBC, and tolerance test of various GNPs, GNCs, and NP-AB against different bacterial strains. The MIC of the synthesized GNPs, GNCs, and NP-ABs was found to vary from 1.25–5 mg/mL , MBC from 5–20 mg/mL, and tolerance value (TV) from 2-4 (Table 6.). The minimal concentration of NPs suspension that causes efficient metal ions was detected, also suggest that the bacterial growth inhibition is mainly due to the interaction of GNPs and GNCs with the membrane of the microorganism's (Roy *et al.*, 2019). The results obtained in this study showed a good correlation with the %inhibition of the antibacterial assay in the following order: ZnO-GNP<CuO-GNP<ZnO-AB<GCD-Z10.5. In particular, *P. aeruginosa* was more resistant compared to others and generated higher MIC/MBC/TV. ZnO-GNP and CuO-GNP showed equal potency in terms of MIC/MBC/TV against *P. aeruginosa*, however, it is interesting to note that GCD-Z10.5 showed higher potency in reducing the TV of *P. aeruginosa*, which indicates higher bactericidal action. The results obtained here are comparable and in good agreement with the previous reports (Kalia *et al.*, 2021). This clearly suggests the synergistic effects of GNPs with each other and with conventional antibiotics on antibacterial activity.

Table 6. MIC, MBC and TV of green synthesized ZnO, CuO, GCD-Z10.5, and ZnO-AB.

Bacterial strains tested	MIC and MBC (mg/ml) with TV of green synthesized nanoparticles											
	ZnO			CuO			GCD-Z10.5			ZnO-AB		
	MIC	MBC	TV	MIC	MBC	TV	MIC	MBC	TV	MIC	MBC	TV
E. coli	2.5	10	4	5	5	1	1.25	2.5	2	2.5	5	2
P. aeruginosa	5	20	4	5	20	4	2.5	5	2	2.5	10	4
S. aureus	2.5	10	4	2.5	5	2	1.25	2.5	2	5	10	2
S. pyogenes	2.5	10	4	5	10	2	1.25	2.5	2	2.5	5	2

TV: tolerance values of the bacteria, MIC : minimum inhibition concentration (mg/mL), MBC : minimum bactericidal concentration (mg/mL).

Even if the antibacterial activity of NPs is based on a different mechanism, it is reported to be mainly due to the release of antimicrobial ions, interactions of NPs with microorganisms, and the production of ROS as a result of light radiation (Abebe *et al.*, 2020). According to this study, the minimal effects of metal ions were confirmed from the MIC and MBC analyses, and the experiments also did not use light as a radion source. Thus, the main mechanism for bacterial deactivation is bacterial cell interaction with the GNPs or GNCs, although with some release of ions. It has been reported that oxidative stress is induced by the generation of ROS as a result of the electrostatic and/or van der Waals interactions between NPs and bacterial cells (Mat Yusuf *et al.*, 2020). The generation of ROS was also confirmed on the antioxidant experimental test based on the 2,2-diphenyl-1-picrylhydrazyl (DPPH) free radical scavenging, which indicated that the amount of ROS that might be generated corresponded with a higher %RSA of GNPs-AB. Similar ROS generation through chitosan-MoS_2 nanosheets with bacterial cell interaction, ROS generation, and then oxidative stress was also reported, as shown in Figure 1 (Roy *et al.*, 2019).

4.13. Antioxidation potential

The antioxidant activity was determined by a DPPH free radical scavenging assay that works on the principle of reduction of DPPH by hydrogen donors to 2,2-diphenyl-1-picrylhydrazyl (DPPH) (Akbar *et al.*, 2021). The GNPs, GNCs, and GNPs-AB used in this study were found to show an effective range of radical scavenging at the different concentrations examined (125–2000 µg/mL) (Figure 17). In general, the activities of the samples ranged from 24.8–54.4% RSA for ZnO NPs, 25.6–58.6% RSA for CuO–NPs, 33.6–69.4 % RSA for GCD–Z10.5, and 40.8-80.9 for ZnO-AB were found to be dose-dependent. Ascorbic acid was used as a standard reference with the same concentrations, and the generated values were found to be in the range of 90.8–93.3% RSA. The antioxidation potential was observed in the following order: ZnO-GNP<CuO-GNP<GCD-Z10.5<ZnO-AB, The higher antioxidant potential may have implications in the intracellular generation of ROS that may be conducive and useful for the bactericidal action.

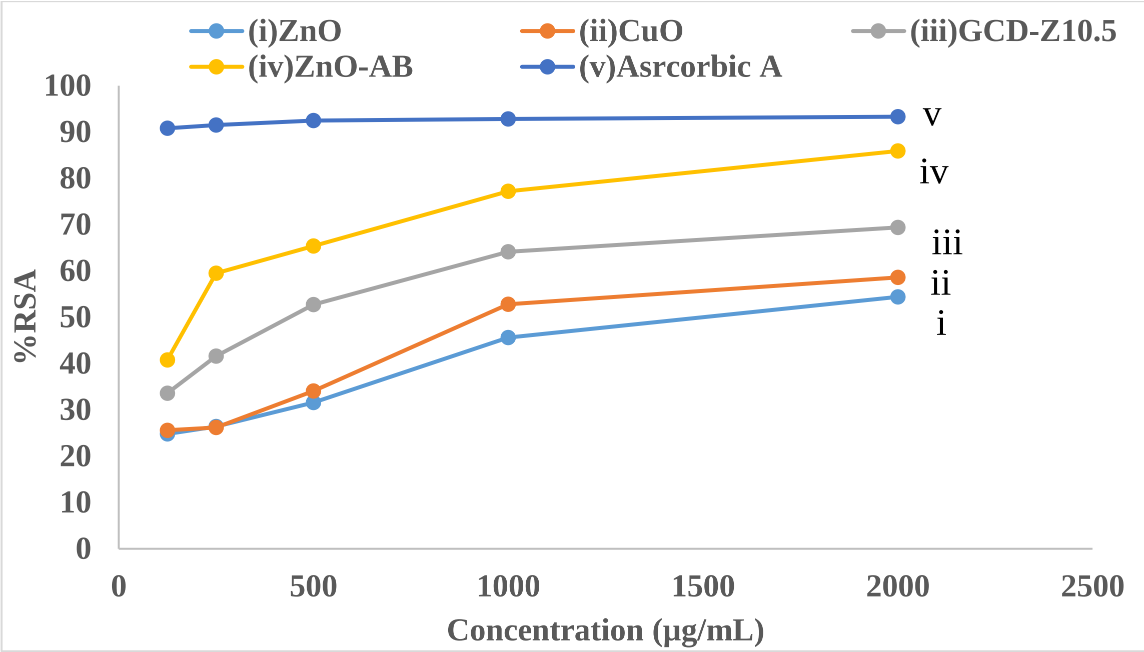

Figure 17. Antioxidant activity of ZnO, CuO, GCD-Z10.5, ZnO-AB, and Vitamin C (ascorbic acid, standard control) determined by the DPPH free radical scavenging assay.

The IC_{50} for ZnO, CuO, GD-Z10.5, and Zn-AB were found to be 1596.5, 1331.8, 648.3 and 191.1 mg/mL, respectively. IC50 is the concentration of the testing sample for antioxidant activities that required to scavenge 50% of initial DPPH radicals. The GCD-Z10.5 and ZnO-AB showed the least IC50 values (648.3, and 191.1 mg/mL) that indicate higher antioxidant activity compared with ZnO (1596.5), and CuO (1331.8) alone, respectively. This might be due to much free electron on surface of metal nanocomposites and some functional groups on the antibiotic in ZnO-antibiotic conjugate, which highly enable to scavenge the radicals from solution.

5. CONCLUSION AND RECOMMENDATION

The *S. incanum* L. extract-based green approach was successfully employed to synthesize Cu-doped ZnO (GCD-Zs) and intimately contact CuO-ZnO composites. The XRD pattern and TEM analysis of the synthesized materials showed nanometer-scale size (in the range of 10–50 nm). The presence of a redshift for the doped GCD-Zs composites over single ZnO (from 3.23 to 3.13 on the direct and from 3.04 to 2.97 eV on the indirect Kubelka-Munk function) was confirmed. The PL analysis showed the presence of electron-hole recombination hindrance in the GCD-Zs composites over ZnO, which is the result of shallow-level copper inclusion and heterojunction. The HRTEM analysis confirmed the nearby contact within the CuO-ZnO composite, with d-spacing values of 0.212 and 0.268 nm, which match the (200) and (002) crystal planes of CuO and ZnO, respectively. The overall doping and heterojunction effects proved to improve the crystallinity of GCD-Zs and ROS generation and consequently enhanced the antibacterial activity with the significance values less 0.05 and lowered the MIC/MBC/TV of the GCD-Zs composite over single ZnO in both gram-positive and negative bacteria by the synergy effect. Furthermore, the significant decrease of the tolerance test values to the lowest by the doped mixture on the multi drug-resistant strain, *P. aeruginosa* was notable. The ZnO-AB conjugate was also found to impart synergy effect. It was effective in significantly enhancing all the tested parameters of antibacterial activity, MIC, and MBC compared to ZnO alone. We believe that this green approach to the synthesis of NPs, NCs and ZnO-AB conjugate may contribute to and add possible solutions in the pursuit of antimicrobials for antimicrobial resistant, multidrug-resistant bacteria, and possibly other microbes. Regarding the future prospect of metal oxide nanoparticles, it should be an important consideration to synthesize at neutral and room temperature since adjusting these parameters requires extra costs like buffers and heat. However, tested experiments on the antibacterial and antioxidant properties of synthesized particles were encouraging, and it will need more *in vitro* tests in the future to reduce cytotoxicity by carrying out in vitro cell cytotoxicity tests. The green synthesis approach was observed as appreciable in the current study to fabricate composites, but it has to be improved to get attention from the pharmaceutical industry as nanobiotics after further screenings and improvements. Since zinc oxide-ceftriaxone conjugate showed a high synergistic effect of antibacterial activities as well as antioxidant in the current study, it gives the researchers hope to enhance activities with the rest of the conventional antibiotics that were resisted by microorganisms.

RESEARCH FUND ACKNOWLEDGEMENT

This research is funded by Adama Science and Technology University under grant number ASTU/SM-R/708/23.

REFERENCES

Abbas, A.M., Aboelmagd, A., Kishk, S.M., Nasrallah, H.H., Boyd, W.C., Kalil, H., Orabi, A.S., 2022. A Novel Ibuprofen Derivative and Its Complexes: Physicochemical Characterization, DFT Modeling, Docking, In Vitro Anti-Inflammatory Studies, and DNA Interaction. Molecules **27**, 7540. https://doi.org/10.3390/molecules27217540

Abdelbaky, A.S., Abd El-Mageed, T.A., Babalghith, A.O., Selim, S., Mohamed, A.M.H.A., 2022. Green Synthesis and Characterization of ZnO Nanoparticles Using Pelargonium odoratissimum (L.) Aqueous Leaf Extract and Their Antioxidant, Antibacterial and Anti-inflammatory Activities. Antioxidants 11, 1444. https://doi.org/10.3390/antiox11081444

Abebe, A.F., Cai, T., Wale, M., Song, G., Fjeldså, J., Lei, F., 2019. Factors determining species richness patterns of breeding birds along an elevational gradient in the Horn of Africa region. Ecol. Evol. 9, 9609–9623. https://doi.org/10.1002/ece3.5491

Abebe, B., Kefale, B., Leku, D.T., 2023. Synthesis of copper–silver–zinc oxide nanocomposites for 4-nitrophenol reduction: doping and heterojunction. RSC Adv. 13, 4523–4529. https://doi.org/10.1039/D2RA07845G

Abebe, B., Murthy, H.C.A., 2022. Insights into ZnO-based doped porous nanocrystal frameworks. RSC Adv. 12, 5816–5833. https://doi.org/10.1039/D1RA09152B

Abebe, B., Zereffa, E.A., Murthy, H.C.A., 2021. Synthesis of Poly(vinyl alcohol)-Aided ZnO/Mn 2 O 3 Nanocomposites for Acid Orange-8 Dye Degradation: Mechanism and Antibacterial Activity. ACS Omega 6, 954–964. https://doi.org/10.1021/acsomega.0c05597

Abebe, B., Zereffa, E.A., Tadesse, A., Murthy, H.C.A., 2020. A Review on Enhancing the Antibacterial Activity of ZnO: Mechanisms and Microscopic Investigation. Nanoscale Res. Lett. 15, 190. https://doi.org/10.1186/s11671-020-03418-6

Achamo, T., Zereffa, E.A., Murthy, H.C.A., Ramachandran, V.P., Balachandran, R., 2022. file:///E:/rrrr/New folder/New folder/antioxidant/antioxidants-11-01444.pdf abyssinica leaf extract and its antioxidant, antimicrobial and DNA binding activities. Green Chem. Lett. Rev. 15, 598–614. https://doi.org/10.1080/17518253.2022.2121620

Agarwal, D.C., Singh, U.B., Gupta, S., Singhal, R., Kulriya, P.K., Singh, F., Tripathi, A., Singh, J., Joshi, U.S., Avasthi, D.K., 2019. Enhanced room temperature ferromagnetism and green photoluminescence in Cu doped ZnO thin film synthesised by neutral beam sputtering. Sci. Rep. 9, 6675. https://doi.org/10.1038/s41598-019-43184-9

Agidew, M.G., 2022. Phytochemical analysis of some selected traditional medicinal plants in Ethiopia. Bull. Natl. Res. Cent. 46, 87. https://doi.org/10.1186/s42269-022-00770-8

Ahmad, F., Taj, M.B., Ramzan, M., Ali, H., Ali, A., Adeel, M., Iqbal, H.M.N., Imran, M., 2021. One-pot synthesis and characterization of in-house engineered silver nanoparticles from Flacourtia jangomas fruit extract with effective antibacterial profiles. J. Nanostructure Chem. 11, 131–141. https://doi.org/10.1007/s40097-020-00354-w

Akbar, N., Aslam, Z., Siddiqui, R., Shah, M.R., Khan, N.A., 2021. Zinc oxide nanoparticles conjugated with clinically-approved medicines as potential antibacterial molecules. AMB Express 11, 104. https://doi.org/10.1186/s13568-021-01261-1

AL-Shehri, H.S., Alanazi, H.S., Shaykhayn, A.M., ALharbi, L.S., Alnafaei, W.S., Alorabi, A.Q., Alkorbi, A.S., Alharthi, F.A., 2022. Adsorption of Methylene Blue by Biosorption on Alkali-Treated Solanum incanum: Isotherms, Equilibrium and Mechanism. Sustainability 14, 2644. https://doi.org/10.3390/su14052644

Ali, H.M., Ibrahim, S.M., Abo Zeid, E.F., Al-Hossainy, A.F., El-Aal, M.A., 2022. A comparative study of Cu-anchored 0D and 1D ZnO nanostructures for the reduction of organic pollutants in water. RSC Adv. 12, 16496–16509. https://doi.org/10.1039/D2RA02515A

Applerot, G., Lellouche, J., Lipovsky, A., Nitzan, Y., Lubart, R., Gedanken, A., Banin, E., 2012. Understanding the Antibacterial Mechanism of CuO Nanoparticles: Revealing the Route of Induced Oxidative Stress. Small 8, 3326–3337. https://doi.org/10.1002/smll.201200772

Auta, R., 2011. NUTRITIONAL AND CHEMICAL EVALUATION OF SOLANUMINCANUM (BITTER GARDEN EGG) Toxicology View project Nutrition View project.

Baba, H., Nishiyama, M., Watanabe, T., Kanamori, H., 2022. Review of Antimicrobial Resistance in Wastewater in Japan: Current Challenges and Future Perspectives. Antibiotics 11, 849. https://doi.org/10.3390/antibiotics11070849

Bekru, A.G., Tufa, L.T., Zelekew, O.A., Goddati, M., Lee, J., Sabir, F.K., 2022. Green Synthesis of a CuO–ZnO Nanocomposite for Efficient Photodegradation of Methylene Blue and Reduction of 4-Nitrophenol. ACS Omega 7, 30908–30919. https://doi.org/10.1021/acsomega.2c02687

Ben Salem, B., Essalah, G., Ben Ameur, S., Duponchel, B., Guermazi, H., Guermazi, S., Leroy, G., 2023. Synthesis and comparative study of the structural and optical properties of binary ZnO-based composites for environmental applications. RSC Adv. 13, 6287–6303. https://doi.org/10.1039/D2RA07837F

Bengtsson-Palme, J., Kristiansson, E., Larsson, D.G.J., 2018. Environmental factors influencing the development and spread of antibiotic resistance. FEMS Microbiol. Rev. 42, 68–80. https://doi.org/10.1093/femsre/fux053

Bhushan, M., Mohapatra, D., Kumar, Y., Kasi Viswanath, A., 2021. Fabrication of novel bioceramic α-Fe2O3/MnO nanocomposites: Study of their structural, magnetic, biocompatibility and antibacterial properties. Mater. Sci. Eng. B 268, 115119. https://doi.org/10.1016/j.mseb.2021.115119

Bowden, J.A., Heckert, A., Ulmer, C.Z., Jones, C.M., Koelmel, J.P., Abdullah, L., Ahonen, L., Alnouti, Y., Armando, A.M., Asara, J.M., Bamba, T., Barr, J.R., Bergquist, J., Borchers, C.H., Brandsma, J., Breitkopf, S.B., Yao, L., Yuan, M., Zhao, X.H., Zhou, S., 2017. Harmonizing lipidomics: NIST interlaboratory comparison exercise for lipidomics using SRM 1950–Metabolites in Frozen Human Plasma. J. Lipid Res. 58, 2275–2288. https://doi.org/10.1194/jlr.M079012

Bürgmann, H., Frigon, D., H Gaze, W., M Manaia, C., Pruden, A., Singer, A.C., F Smets, B., Zhang, T., 2018. Water and sanitation: an essential battlefront in the war on antimicrobial resistance. FEMS Microbiol. Ecol. 94, 1–14. https://doi.org/10.1093/femsec/fiy101

Costas, A., Florica, C., Preda, N., Besleaga, C., Kuncser, A., Enculescu, I., 2022. Self-connected CuO–ZnO radial core–shell heterojunction nanowire arrays grown on interdigitated electrodes for visible-light photodetectors. Sci. Rep. 12, 6834. https://doi.org/10.1038/s41598-022-10879-5

Crabtree, J.H., Shrestha, B.M., Chow, K.-M., Figueiredo, A.E., Povlsen, J. V., Wilkie, M., Abdel-Aal, A., Cullis, B., Goh, B.-L., Briggs, V.R., Brown, E.A., Dor, F.J.M.F., 2019. Creating and Maintaining Optimal Peritoneal Dialysis Access in the Adult Patient: 2019 Update. Perit. Dial. Int. J. Int. Soc. Perit. Dial. 39, 414–436. https://doi.org/10.3747/pdi.2018.00232

Cushing, B.L., Kolesnichenko, V.L., O'Connor, C.J., 2004. Recent Advances in the Liquid-Phase Syntheses of Inorganic Nanoparticles. Chem. Rev. 104, 3893–3946. https://doi.org/10.1021/cr030027b

Din, M.I., Jabbar, S., Najeeb, J., Khalid, R., Ghaffar, T., Arshad, M., Khan, S.A., Ali, S., 2020. Green synthesis of zinc ferrite nanoparticles for photocatalysis of methylene blue. Int. J. Phytoremediation 22, 1440–1447.

https://doi.org/10.1080/15226514.2020.1781783
Doan Thi, T.U., Nguyen, T.T., Thi, Y.D., Ta Thi, K.H., Phan, B.T., Pham, K.N., 2020. Green synthesis of ZnO nanoparticles using orange fruit peel extract for antibacterial activities. RSC Adv. 10, 23899–23907. https://doi.org/10.1039/D0RA04926C
Dye, C., 2014. After 2015: infectious diseases in a new era of health and development. Philos. Trans. R. Soc. B Biol. Sci. 369, 20130426. https://doi.org/10.1098/rstb.2013.0426
Frascaroli, G., Reid, D., Hunter, C., Roberts, J., Helwig, K., Spencer, J., Escudero, A., 2021. Pharmaceuticals in Wastewater Treatment Plants: A Systematic Review on the Substances of Greatest Concern Responsible for the Development of Antimicrobial Resistance. Appl. Sci. 11, 6670. https://doi.org/10.3390/app11156670
Gashe, F., Mulisa, E., Mekonnen, M., Zeleke, G., 2018. Antimicrobial Resistance Profile of Different Clinical Isolates against Third-Generation Cephalosporins. J. Pharm. 2018, 1–7. https://doi.org/10.1155/2018/5070742
Ghaffar, N., Javad, S., Farrukh, M.A., Shah, A.A., Gatasheh, M.K., AL-Munqedhi, B.M.A., Chaudhry, O., 2022. Metal nanoparticles assisted revival of Streptomycin against MDRS Staphylococcus aureus. PLoS One 17, e0264588. https://doi.org/10.1371/journal.pone.0264588
Govindasamy, G.A., Mydin, R.B.S.M.N., Sreekantan, S., Harun, N.H., 2021. Compositions and antimicrobial properties of binary ZnO–CuO nanocomposites encapsulated calcium and carbon from Calotropis gigantea targeted for skin pathogens. Sci. Rep. 11, 99. https://doi.org/10.1038/s41598-020-79547-w
Gupta, A., Tiwari, S.K., Netrebov, V., Chikindas, M.L., 2016. Biochemical Properties and Mechanism of Action of Enterocin LD3 Purified from Enterococcus hirae LD3. Probiotics Antimicrob. Proteins 8, 161–169. https://doi.org/10.1007/s12602-016-9217-y
Gupta, J., Bahadur, D., 2018. Defect-Mediated Reactive Oxygen Species Generation in Mg-Substituted ZnO Nanoparticles: Efficient Nanomaterials for Bacterial Inhibition and Cancer Therapy. ACS Omega 3, 2956–2965. https://doi.org/10.1021/acsomega.7b01953
Halder, U., Roy, R.K., Biswas, R., Khan, D., Mazumder, K., Bandopadhyay, R., 2022. Synthesis of copper oxide nanoparticles using capsular polymeric substances produced by Bacillus altitudinis and investigation of its efficacy to kill pathogenic Pseudomonas aeruginosa. Chem. Eng. J. Adv. 11, 100294. https://doi.org/10.1016/j.ceja.2022.100294

Hasheminya, S.-M., Dehghannya, J., 2021. Development and characterization of novel edible films based on Cordia dichotoma gum incorporated with Salvia mirzayanii essential oil nanoemulsion. Carbohydr. Polym. 257, 117606. https://doi.org/10.1016/j.carbpol.2020.117606

Hassan, I.A., Sathasivam, S., Nair, S.P., Carmalt, C.J., 2017. Antimicrobial Properties of Copper-Doped ZnO Coatings under Darkness and White Light Illumination. ACS Omega 2, 4556–4562. https://doi.org/10.1021/acsomega.7b00759

Hayat, S., Ashraf, A., Zubair, M., Aslam, B., Siddique, M.H., Khurshid, M., Saqalein, M., Khan, A.M., Almatroudi, A., Naeem, Z., Muzammil, S., 2022. Biofabrication of ZnO nanoparticles using Acacia arabica leaf extract and their antibiofilm and antioxidant potential against foodborne pathogens. PLoS One 17, e0259190. https://doi.org/10.1371/journal.pone.0259190

Hirpha, H.H., Mpandeli, S., Bantider, A., 2020. Determinants of adaptation strategies to climate change among the smallholder farmers in Adama District, Ethiopia. Int. J. Clim. Chang. Strateg. Manag. 12, 463–476. https://doi.org/10.1108/IJCCSM-01-2019-0002

Hussain, R., Zafar, A., Hasan, M., Tariq, T., Saif, M.S., Waqas, M., Tariq, F., Anum, M., Anjum, S.I., Shu, X., 2023. Casting Zinc Oxide Nanoparticles Using Fagonia Blend Microbial Arrest. Appl. Biochem. Biotechnol. 195, 264–282. https://doi.org/10.1007/s12010-022-04152-8

Ibrahim, M.I., Alsafadi, D., Alamry, K.A., Oves, M., Alosaimi, A.M., Hussein, M.A., 2022. A promising antimicrobial bionanocomposite based poly(3-hydroxybutyrate-co-3-hydroxyvalerate) reinforced silver doped zinc oxide nanoparticles. Sci. Rep. 12, 14299. https://doi.org/10.1038/s41598-022-17470-y

Jain, M.K., Ridker, P.M., 2005. Anti-Inflammatory Effects of Statins: Clinical Evidence and Basic Mechanisms. Nat. Rev. Drug Discov. 4, 977–987. https://doi.org/10.1038/nrd1901

Jerwood, S., Cohen, J., 2007. Unexpected antimicrobial effect of statins. J. Antimicrob. Chemother. 61, 362–364. https://doi.org/10.1093/jac/dkm496

Jubeh, B., Breijyeh, Z., Karaman, R., 2020. Resistance of Gram-Positive Bacteria to Current Antibacterial Agents and Overcoming Approaches. Molecules 25, 2888. https://doi.org/10.3390/molecules25122888

Kalia, A., Kaur, M., Shami, A., Jawandha, S.K., Alghuthaymi, M.A., 2021. Nettle-Leaf Extract Derived ZnO / CuO Nanoparticle- Biopolymer-Based Antioxidant and Antimicrobial Nanocomposite Packaging Films and Their Impact on Extending the

Post-Harvest Shelf Life of Guava Fruit 1–24.

Kara, M., Hasinoff, B., McKay, D., Campbell, N., 1991. Clinical and chemical interactions between iron preparations and ciprofloxacin. Br. J. Clin. Pharmacol. 31, 257–261. https://doi.org/10.1111/j.1365-2125.1991.tb05526.x

KARATAŞ, A., ÜLKÜ, B., KAYA, M., ÖZTURAN, A., 2020. Chronic Kidney Disease and Multiple Myeloma Case in Clinical Nephrology. Middle Black Sea J. Heal. Sci. 6, 135–138. https://doi.org/10.19127/mbsjohs.694541

Karthik, K.V., Raghu, A.V., Reddy, K.R., Ravishankar, R., Sangeeta, M., Shetti, N.P., Reddy, C.V., 2022. Green synthesis of Cu-doped ZnO nanoparticles and its application for the photocatalytic degradation of hazardous organic pollutants. Chemosphere 287, 132081. https://doi.org/10.1016/j.chemosphere.2021.132081

Kazmi, J., Ooi, P.C., Raza, S.R.A., Goh, B.T., Karim, S.S.A., Samat, M.H., Lee, M.K., Mohd. Razip Wee, M.F., Taib, M.F.M., Mohamed, M.A., 2021. Appealing stable room-temperature ferromagnetism by well-aligned 1D Co-doped zinc oxide nanowires. J. Alloys Compd. 872, 159741. https://doi.org/10.1016/j.jallcom.2021.159741

Khalid, A., Ahmad, P., Alharthi, A.I., Muhammad, S., Khandaker, M.U., Faruque, M.R.I., Din, I.U., Alotaibi, M.A., Khan, A., 2021. Synergistic effects of Cu-doped ZnO nanoantibiotic against Gram-positive bacterial strains. PLoS One 16, e0251082. https://doi.org/10.1371/journal.pone.0251082

Khan, M.F., Khan, M.A., 2023. Plant-Derived Metal Nanoparticles (PDMNPs): Synthesis, Characterization, and Oxidative Stress-Mediated Therapeutic Actions. Futur. Pharmacol. 3, 252–295. https://doi.org/10.3390/futurepharmacol3010018

Khan, S.A., Noreen, F., Kanwal, S., Iqbal, A., Hussain, G., 2018. Green synthesis of ZnO and Cu-doped ZnO nanoparticles from leaf extracts of Abutilon indicum, Clerodendrum infortunatum, Clerodendrum inerme and investigation of their biological and photocatalytic activities. Mater. Sci. Eng. C 82, 46–59. https://doi.org/10.1016/j.msec.2017.08.071

Landage, S.., Wasif, A.., Dhuppe, P., 2014. Synthesis of Nanosilver Using Chemical Reduction Methods. Int. J. Adv. Res. Eng. Appl. Sci. 3, 14–22.

Lashin, I., Fouda, A., Gobouri, A.A., Azab, E., Mohammedsaleh, Z.M., Makharita, R.R., 2021. Antimicrobial and In Vitro Cytotoxic Efficacy of Biogenic Silver Nanoparticles (Ag-NPs) Fabricated by Callus Extract of Solanum incanum L. Biomolecules 11, 341. https://doi.org/10.3390/biom11030341

Liu, J., Li, J., Wei, F., Zhao, X., Su, Y., Han, X., 2019. Ag–ZnO Submicrometer Rod Arrays for High-Efficiency Photocatalytic Degradation of Congo Red and Disinfection. ACS Sustain. Chem. Eng. 7, 11258–11266. https://doi.org/10.1021/acssuschemeng.9b00610

Luo, F., Yu, Y., Li, M., Chen, Y., Zhang, P., Xiao, C., Lv, G., 2022. Polymeric nanomedicines for the treatment of hepatic diseases. J. Nanobiotechnology 20, 488. https://doi.org/10.1186/s12951-022-01708-y

Luu, T.L.A., Cao, X.T., Nguyen, V.T., Pham, N.L., Nguyen, H.L., Nguyen, C.T., 2020. Simple Controlling Ecofriendly Synthesis of Silver Nanoparticles at Room Temperature Using Lemon Juice Extract and Commercial Rice Vinegar. J. Nanotechnol. 2020, 1–9. https://doi.org/10.1155/2020/3539701

Ma, Y., Choi, T.-W., Cheung, S.H., Cheng, Y., Xu, X., Xie, Y.-M., Li, H.-W., Li, M., Luo, H., Zhang, W., So, S.K., Chen, S., Tsang, S.-W., 2019. Charge transfer-induced photoluminescence in ZnO nanoparticles. Nanoscale 11, 8736–8743. https://doi.org/10.1039/C9NR02020A

Majeed Khan, M.A., Siwach, R., Kumar, S., Ahmed, M., Ahmed, J., 2020. Investigations on microstructure, optical, magnetic, photocatalytic, and dielectric behaviours of pure and Co-doped ZnO NPs. J. Mater. Sci. Mater. Electron. 31, 6360–6371. https://doi.org/10.1007/s10854-020-03192-2

Manikandan, A., Sridhar, R., Arul Antony, S., Ramakrishna, S., 2014. A simple aloe vera plant-extracted microwave and conventional combustion synthesis: Morphological, optical, magnetic and catalytic properties of CoFe2O4 nanostructures. J. Mol. Struct. 1076, 188–200. https://doi.org/10.1016/j.molstruc.2014.07.054

Marinescu, L., Ficai, D., Oprea, O., Marin, A., Ficai, A., Andronescu, E., Holban, A.-M., 2020. Optimized Synthesis Approaches of Metal Nanoparticles with Antimicrobial Applications. J. Nanomater. 2020, 1–14. https://doi.org/10.1155/2020/6651207

Maruthapandi, M., Saravanan, A., Das, P., Natan, M., Jacobi, G., Banin, E., Luong, J.H.T., Gedanken, A., 2020. Antimicrobial Activities of Zn-Doped CuO Microparticles Decorate(1) Hassan, I. A.; Sathasivam, S.; Nair, S. P.; Carmalt, C. J. Antimicrobial Properties of Copper-Doped ZnO Coatings under Darkness and White Light Illumination. ACS Omega 2017, 2 (8), 4556–4. ACS Appl. Polym. Mater. 2, 5878–5888. https://doi.org/10.1021/acsapm.0c01104

Mat Yusuf, S.N.A., Che Mood, C.N.A., Ahmad, N.H., Sandai, D., Lee, C.K., Lim, V., 2020. Optimization of biogenic synthesis of silver nanoparticles from flavonoid-rich Clinacanthus nutans leaf and stem aqueous extracts. R. Soc. Open Sci. 7, 200065. https://doi.org/10.1098/rsos.200065

Mekawi, E.M., Sharoba, A.M., Ramadan, M.F., 2019. Reduction of acrylamide formation in potato chips during deep-frying in sunflower oil using pomegranate peel nanoparticles extract. J. Food Meas. Charact. 13, 3298–3306. https://doi.org/10.1007/s11694-019-00252-y

Mitchell, M.J., Billingsley, M.M., Haley, R.M., Wechsler, M.E., Peppas, N.A., Langer, R., 2021. Engineering precision nanoparticles for drug delivery. Nat. Rev. Drug Discov. 20, 101–124. https://doi.org/10.1038/s41573-020-0090-8

Momeni, S.S., Nasrollahzadeh, M., Rustaiyan, A., 2016. Green synthesis of the Cu/ZnO nanoparticles mediated by Euphorbia prolifera leaf extract and investigation of their catalytic activity. J. Colloid Interface Sci. 472, 173–179. https://doi.org/10.1016/j.jcis.2016.03.042

Morales-Mendoza, J.E., Paraguay-Delgado, F., 2021. Widening UV–Vis absorption band by Cu doped ZnO and ZnO/CuO composite. Mater. Lett. 291, 129494. https://doi.org/10.1016/j.matlet.2021.129494

Muthuvel, A., Jothibas, M., Manoharan, C., 2020. Synthesis of copper oxide nanoparticles by chemical and biogenic methods: photocatalytic degradation and in vitro antioxidant activity. Nanotechnol. Environ. Eng. 5, 14. https://doi.org/10.1007/s41204-020-00078-w

Nadimpalli, M.L., Marks, S.J., Montealegre, M.C., Gilman, R.H., Pajuelo, M.J., Saito, M., Tsukayama, P., Njenga, S.M., Kiiru, J., Swarthout, J., Islam, M.A., Julian, T.R., Pickering, A.J., 2020. Urban informal settlements as hotspots of antimicrobial resistance and the need to curb environmental transmission. Nat. Microbiol. 5, 787–795. https://doi.org/10.1038/s41564-020-0722-0

Oloya, B., Namukobe, J., Ssengooba, W., Afayoa, M., Byamukama, R., 2022. Phytochemical screening, antimycobacterial activity and acute toxicity of crude extracts of selected medicinal plant species used locally in the treatment of tuberculosis in Uganda. Trop. Med. Health 50. https://doi.org/10.1186/s41182-022-00406-7

Onoue, S., Uchida, A., Kuriyama, K., Nakamura, T., Seto, Y., Kato, M., Hatanaka, J., Tanaka, T., Miyoshi, H., Yamada, S., 2012. Novel solid self-emulsifying drug delivery system of coenzyme Q10 with improved photochemical and pharmacokinetic behaviors. Eur. J. Pharm. Sci. 46, 492–499. https://doi.org/10.1016/j.ejps.2012.03.015

Paraguay-Delgado, F., Hermida-Montero, L.A., Morales-Mendoza, J.E., Durán-Barradas, Z., Mtz-Enriquez, A.I., Pariona, N., 2022. Photocatalytic properties of Cu-containing ZnO nanoparticles and their antifungal activity against agriculture-pathogenic fungus.

RSC Adv. 12, 9898–9908. https://doi.org/10.1039/D2RA00863G

Park, J.C., Kim, A.Y., Kim, J.Y., Park, S., Park, K.H., Song, H., 2012. ZnO–CuO core–branch nanocatalysts for ultrasound-assisted azide–alkyne cycloaddition reactions. Chem. Commun. 48, 8484. https://doi.org/10.1039/c2cc31654d

Perelshtein, I., Lipovsky, A., Perkas, N., Gedanken, A., Moschini, E., Mantecca, P., 2015. The influence of the crystalline nature of nano-metal oxides on their antibacterial and toxicity properties. Nano Res. 8, 695–707. https://doi.org/10.1007/s12274-014-0553-5

Pioletti, M., 2001. Crystal structures of complexes of the small ribosomal subunit with tetracycline, edeine and IF3. EMBO J. 20, 1829–1839. https://doi.org/10.1093/emboj/20.8.1829

Ren, M., Frimmel, F.H., Abbt-Braun, G., 2015. Multi-cycle photocatalytic degradation of bezafibrate by a cast polyvinyl alcohol/titanium dioxide (PVA/TiO2) hybrid film. J. Mol. Catal. A Chem. 400, 42–48. https://doi.org/10.1016/j.molcata.2015.02.004

Rizvi, A., Zaidi, A., Ameen, F., Ahmed, B., AlKahtani, M.D.F., Khan, M.S., 2020. Heavy metal induced stress on wheat: phytotoxicity and microbiological management. RSC Adv. 10, 38379–38403. https://doi.org/10.1039/D0RA05610C

Rousham, E.K., Unicomb, L., Islam, M.A., 2018. Human, animal and environmental contributors to antibiotic resistance in low-resource settings: integrating behavioural, epidemiological and One Health approaches. Proc. R. Soc. B Biol. Sci. 285, 20180332. https://doi.org/10.1098/rspb.2018.0332

Roy, S., Mondal, A., Yadav, V., Sarkar, A., Banerjee, R., Sanpui, P., Jaiswal, A., 2019. Mechanistic Insight into the Antibacterial Activity of Chitosan Exfoliated MoS 2 Nanosheets: Membrane Damage, Metabolic Inactivation, and Oxidative Stress. ACS Appl. Bio Mater. 2, 2738–2755. https://doi.org/10.1021/acsabm.9b00124

Salleh, A., Naomi, R., Utami, N.D., Mohammad, A.W., Mahmoudi, E., Mustafa, N., Fauzi, M.B., 2020. The Potential of Silver Nanoparticles for Antiviral and Antibacterial Applications: A Mechanism of Action. Nanomaterials 10, 1566. https://doi.org/10.3390/nano10081566

Sánchez-López, E., Gomes, D., Esteruelas, G., Bonilla, L., Lopez-Machado, A.L., Galindo, R., Cano, A., Espina, M., Ettcheto, M., Camins, A., Silva, A.M., Durazzo, A., Santini, A., Garcia, M.L., Souto, E.B., 2020. Metal-Based Nanoparticles as Antimicrobial Agents: An Overview. Nanomaterials 10, 292. https://doi.org/10.3390/nano10020292

Sanganabhatla, D., Sunder, R.S., 2019. Development and Validation of UV Spectrophotometric Method For The Estimation of Finasteride Drug. Int. J. Pharm.

Qual. Assur. 10, 597–600. https://doi.org/10.25258/ijpqa.10.4.6

Sanginario, A., Miccoli, B., Demarchi, D., 2017. Carbon Nanotubes as an Effective Opportunity for Cancer Diagnosis and Treatment. Biosensors 7, 9. https://doi.org/10.3390/bios7010009

Saravanan, R., Karthikeyan, S., Gupta, V.K., Sekaran, G., Narayanan, V., Stephen, A., 2013. Enhanced photocatalytic activity of ZnO/CuO nanocomposite for the degradation of textile dye on visible light illumination. Mater. Sci. Eng. C 33, 91–98. https://doi.org/10.1016/j.msec.2012.08.011

Sbhatu, D.B., Abraha, H.B., 2020. Preliminary Antimicrobial Profile of Solanum incanum L.: A Common Medicinal Plant. Evidence-Based Complement. Altern. Med. 2020, 1–6. https://doi.org/10.1155/2020/3647065

Scandorieiro, S., de Camargo, L.C., Lancheros, C.A.C., Yamada-Ogatta, S.F., Nakamura, C. V., de Oliveira, A.G., Andrade, C.G.T.J., Duran, N., Nakazato, G., Kobayashi, R.K.T., 2016. Synergistic and Additive Effect of Oregano Essential Oil and Biological Silver Nanoparticles against Multidrug-Resistant Bacterial Strains. Front. Microbiol. 7, 1–14. https://doi.org/10.3389/fmicb.2016.00760

Sharma, D., Jha, R., 2017. Analysis of structural, optical and magnetic properties of Fe/Co co-doped ZnO nanocrystals. Ceram. Int. 43, 8488–8496. https://doi.org/10.1016/j.ceramint.2017.03.201

Singh, B., Singh, B.N., Chandra, A., Al-Haddad, K., Pandey, A., Kothari, D.P., 2004. A Review of Three-Phase Improved Power Quality AC–DC Converters. IEEE Trans. Ind. Electron. 51, 641–660. https://doi.org/10.1109/TIE.2004.825341

Singh, G.P., Aman, A.K., Singh, R.K., Roy, M.K., 2020. Effect of low Co-doping on structural, optical, and magnetic performance of ZnO nanoparticles. Optik (Stuttg). 203, 163966. https://doi.org/10.1016/j.ijleo.2019.163966

Singh, J., Dutta, T., Kim, K.H., Rawat, M., Samddar, P., Kumar, P., 2018. "Green" synthesis of metals and their oxide nanoparticles: Applications for environmental remediation. J. Nanobiotechnology 16, 1–24. https://doi.org/10.1186/s12951-018-0408-4

Singh, P.K., kumar, P., hussain, M., das, A.K., nayak, G.C., 2016. Synthesis and characterization of CuO nanoparticles using strong base electrolyte through electrochemical discharge process. Bull. Mater. Sci. 39, 469–478. https://doi.org/10.1007/s12034-016-1159-1

Sorbiun, M., Shayegan Mehr, E., Ramazani, A., Taghavi Fardood, S., 2018. Green Synthesis of Zinc Oxide and Copper Oxide Nanoparticles Using Aqueous Extract of Oak Fruit

Hull (Jaft) and Comparing Their Photocatalytic Degradation of Basic Violet 3. Int. J. Environ. Res. 12, 29–37. https://doi.org/10.1007/s41742-018-0064-4

Stanton, I.C., Tipper, H.J., Chau, K., Klümper, U., Subirats, J., Murray, A.K., 2022. Does Environmental Exposure to Pharmaceutical and Personal Care Product Residues Result in the Selection of Antimicrobial-Resistant Microorganisms, and is this Important in Terms of Human Health Outcomes? Environ. Toxicol. Chem. 00, 1–14. https://doi.org/10.1002/etc.5498

Tamayo, L.A., Zapata, P.A., Vejar, N.D., Azócar, M.I., Gulppi, M.A., Zhou, X., Thompson, G.E., Rabagliati, F.M., Páez, M.A., 2014. Release of silver and copper nanoparticles from polyethylene nanocomposites and their penetration into Listeria monocytogenes. Mater. Sci. Eng. C 40, 24–31. https://doi.org/10.1016/j.msec.2014.03.037

Tan, S.Y., Tan, I.K.P., Tan, M.F., Dutta, A., Choo, S.W., 2016. Evolutionary study of Yersinia genomes deciphers emergence of human pathogenic species. Sci. Rep. 6, 36116. https://doi.org/10.1038/srep36116

Tatli Seven, P., Seven, I., Gul Baykalir, B., Iflazoglu Mutlu, S., Salem, A.Z.M., 2018. Nanotechnology and nano-propolis in animal production and health: an overview. Ital. J. Anim. Sci. 17, 921–930. https://doi.org/10.1080/1828051X.2018.1448726

Thabit, H.A., Kabir, N.A., Ismail, A.K., Alraddadi, S., Bafaqeer, A., Saleh, M.A., 2022. Development of Ag-Doped ZnO Thin Films and Thermoluminescence (TLD) Characteristics for Radiation Technology. Nanomaterials 12, 3068. https://doi.org/10.3390/nano12173068

Theyvaraju, D., Muthukumaran, S., 2015. Preparation, structural, photoluminescence and magnetic studies of Cu doped ZnO nanoparticles co-doped with Ni by sol–gel method. Phys. E Low-dimensional Syst. Nanostructures 74, 93–100. https://doi.org/10.1016/j.physe.2015.06.012

Tornberg-Belanger, S.N., Rwigi, D., Mugo, M., Kitheka, L., Onamu, N., Ounga, D., Diakhate, M.M., Atlas, H.E., Wald, A., McClelland, R.S., Soge, O.O., Tickell, K.D., Kariuki, S., Singa, B.O., Walson, J.L., Pavlinac, P.B., 2022. Antimicrobial resistance including Extended Spectrum Beta Lactamases (ESBL) among E. coli isolated from kenyan children at hospital discharge. PLoS Negl. Trop. Dis. 16, e0010283. https://doi.org/10.1371/journal.pntd.0010283

Vaez, Z., Javanbakht, V., 2020. Synthesis, characterization and photocatalytic activity of ZSM-5/ZnO nanocomposite modified by Ag nanoparticles for methyl orange degradation. J. Photochem. Photobiol. A Chem. 388, 112064.

https://doi.org/10.1016/j.jphotochem.2019.112064

Vazquez-Muñoz, R., Meza-Villezcas, A., Fournier, P.G.J., Soria-Castro, E., Juarez-Moreno, K., Gallego-Hernández, A.L., Bogdanchikova, N., Vazquez-Duhalt, R., Huerta-Saquero, A., 2019. Enhancement of antibiotics antimicrobial activity due to the silver nanoparticles impact on the cell membrane. PLoS One 14, e0224904. https://doi.org/10.1371/journal.pone.0224904

Verma, N., Kumar, N., 2019. Synthesis and Biomedical Applications of Copper Oxide Nanoparticles: An Expanding Horizon. ACS Biomater. Sci. Eng. 5, 1170–1188. https://doi.org/10.1021/acsbiomaterials.8b01092

Versporten, A., Zarb, P., Caniaux, I., Gros, M.-F., Drapier, N., Miller, M., Jarlier, V., Nathwani, D., Goossens, Septimus, E.J., Greer, N., Gawrys, G., Rios, E., May, S., 2018. Antimicrobial consumption and resistance in adult hospital inpatients in 53 countries: results of an internet-based global point prevalence survey. Lancet Glob. Heal. 6, e619–e629. https://doi.org/10.1016/S2214-109X(18)30186-4

Wang, L., Hu, C., Shao, L., 2017. The antimicrobial activity of nanoparticles: present situation and prospects for the future. Int. J. Nanomedicine 12, 1227–1249. https://doi.org/10.2147/IJN.S121956

Westerhoff, P., Lee, S., Yang, Y., Gordon, G.W., Hristovski, K., Halden, R.U., Herckes, P., 2015. Characterization, Recovery Opportunities, and Valuation of Metals in Municipal Sludges from U.S. Wastewater Treatment Plants Nationwide. Environ. Sci. Technol. 49, 9479–9488. https://doi.org/10.1021/es505329q

Wilson, D.N., Hauryliuk, V., Atkinson, G.C., O'Neill, A.J., 2020. Target protection as a key antibiotic resistance mechanism. Nat. Rev. Microbiol. 18, 637–648. https://doi.org/10.1038/s41579-020-0386-z

Xie, Y., He, Y., Irwin, P.L., Jin, T., Shi, X., 2011. Antibacterial Activity and Mechanism of Action of Zinc Oxide Nanoparticles against Campylobacter jejuni. Appl. Environ. Microbiol. 77, 2325–2331. https://doi.org/10.1128/AEM.02149-10

Yesuf, A., Wondimeneh, Y., Gebrecherkos, T., Moges, F., 2016. Occurrence of Potential Bacterial Pathogens and Their Antimicrobial Susceptibility Patterns Isolated from Herbal Medicinal Products Sold in Different Markets of Gondar Town, Northwest Ethiopia. Int. J. Bacteriol. 2016, 1–11. https://doi.org/10.1155/2016/1959418

Zebedee, S.L., Lamb, R.A., 1988. Influenza A virus M2 protein: monoclonal antibody restriction of virus growth and detection of M2 in virions. J. Virol. 62, 2762–2772. https://doi.org/10.1128/jvi.62.8.2762-2772.1988

Zhu, D., Wang, L., Yu, W., Xie, H., 2018. Intriguingly high thermal conductivity increment for CuO nanowires contained nanofluids with low viscosity. Sci. Rep. 8, 5282. https://doi.org/10.1038/s41598-018-23174-z

APPENDIX

Appendix 1. The photograph representation of the highlight of the whole synthesis process of nanoparticles

Appendix 2. Shows low-resolution SEM images for (a) ZnO and (b) CuO, in which zinc oxide has a porous and/or amorphous morphology and copper has a highly crystalline morphology.

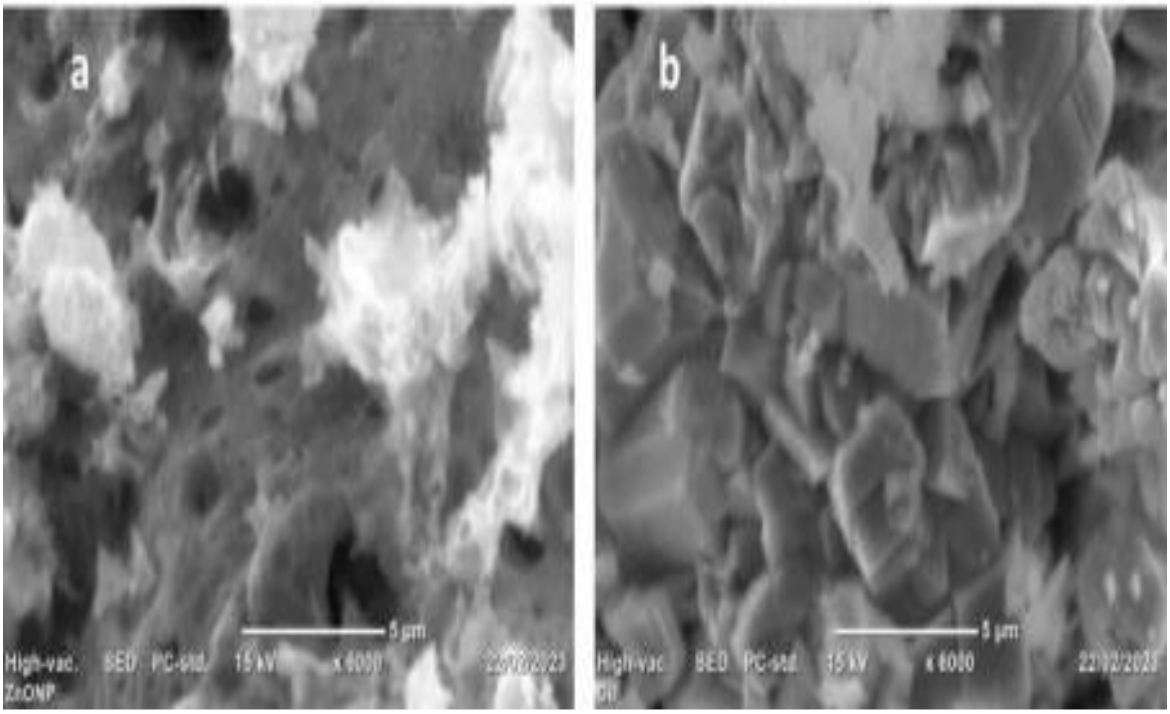

Appendix 3. The radical scavenging activity of ZnO, CuO, GCD-Z10.5, and ZnO-AB

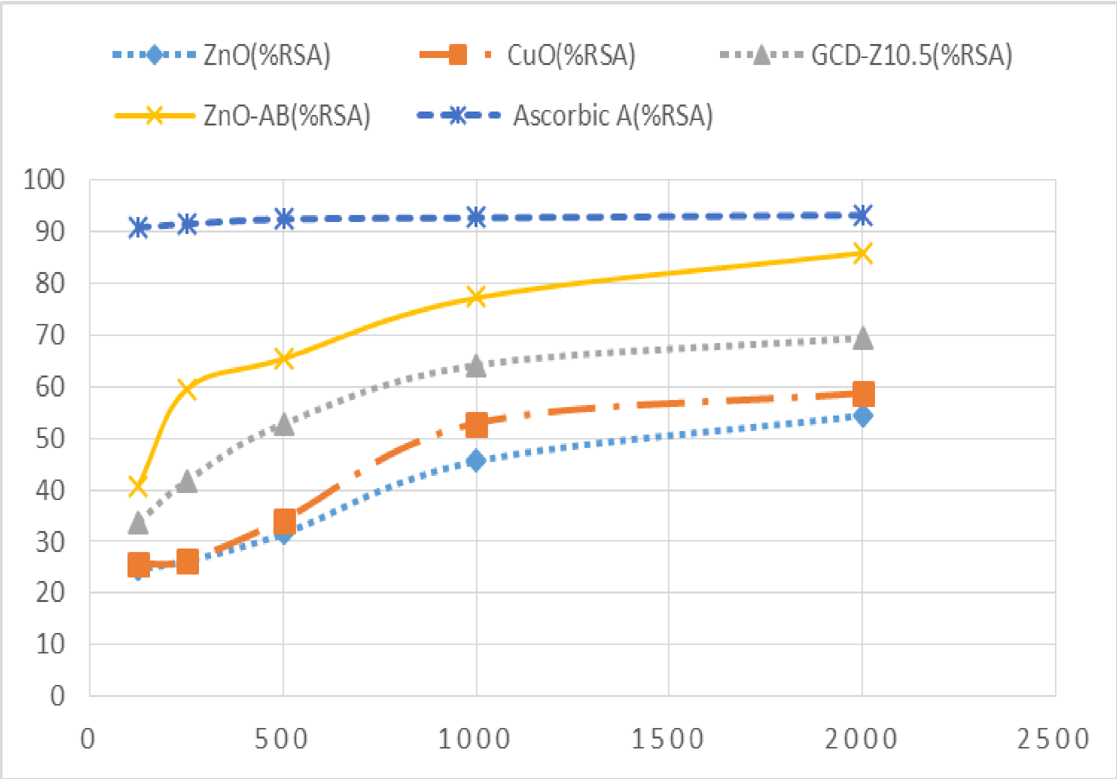

Appendix 4. The equation graph of scavenging activity

Appendix 4.1. The equation graph of ZnO nanoparticle scavenging activity

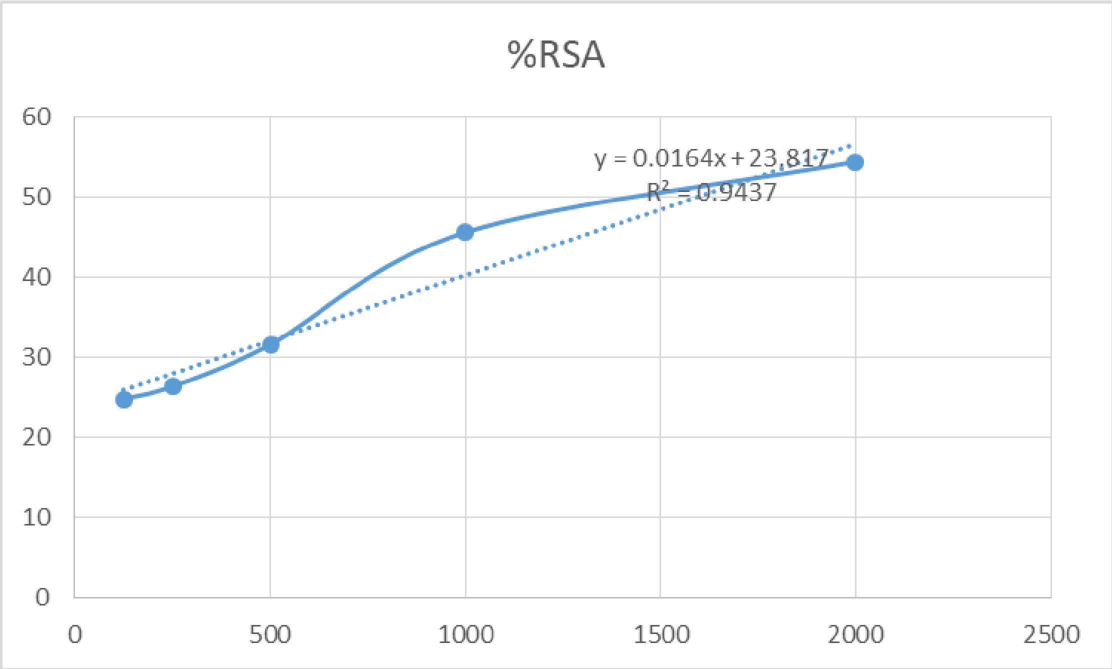

Appendix 4.2. The equation graph of CuO scavenging activity

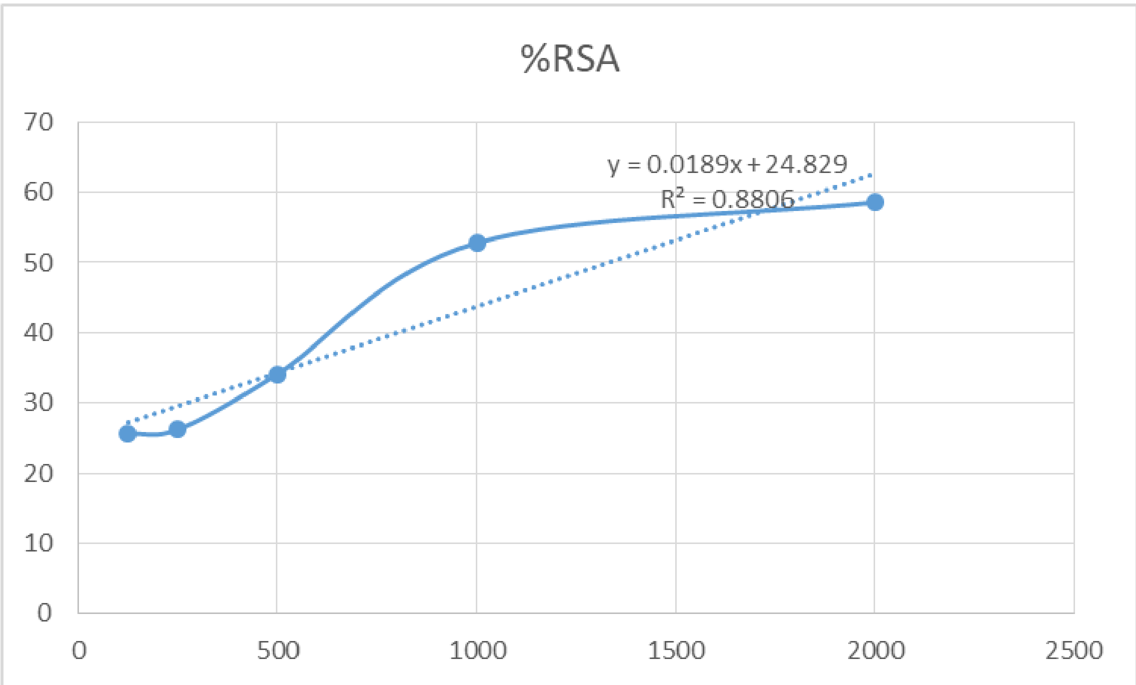

Appendix 4.3. The equation graph of GCD-Z10.5 scavenging activity

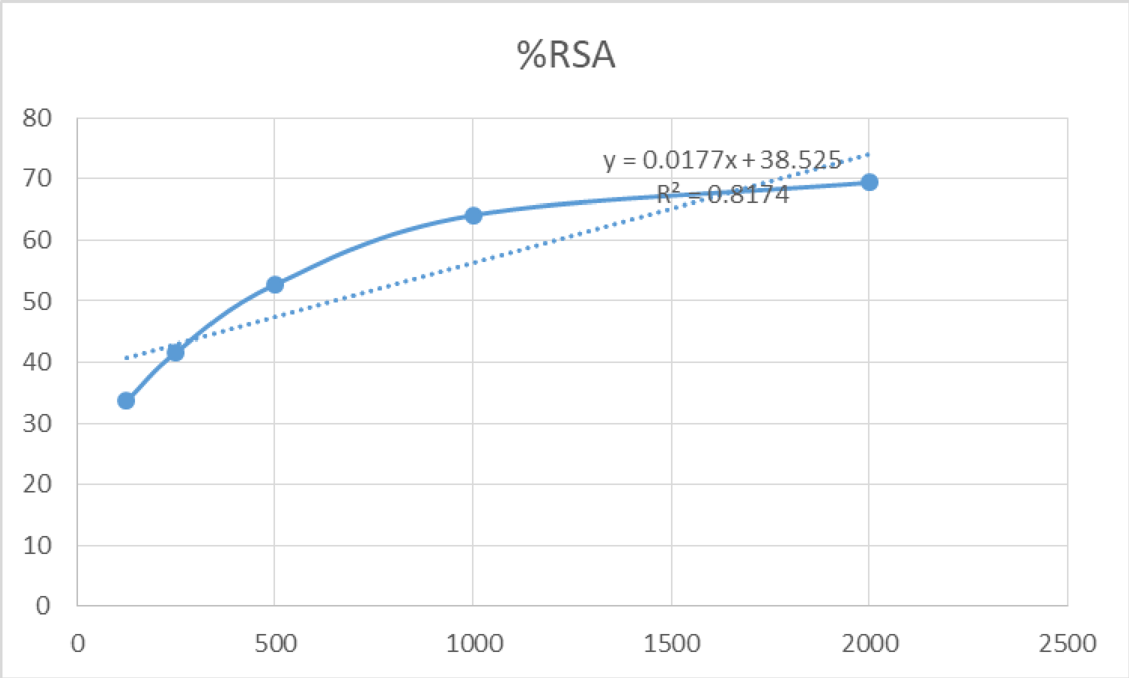

Appendix 4.4. The equation graph of ZnO-AB scavenging activity.

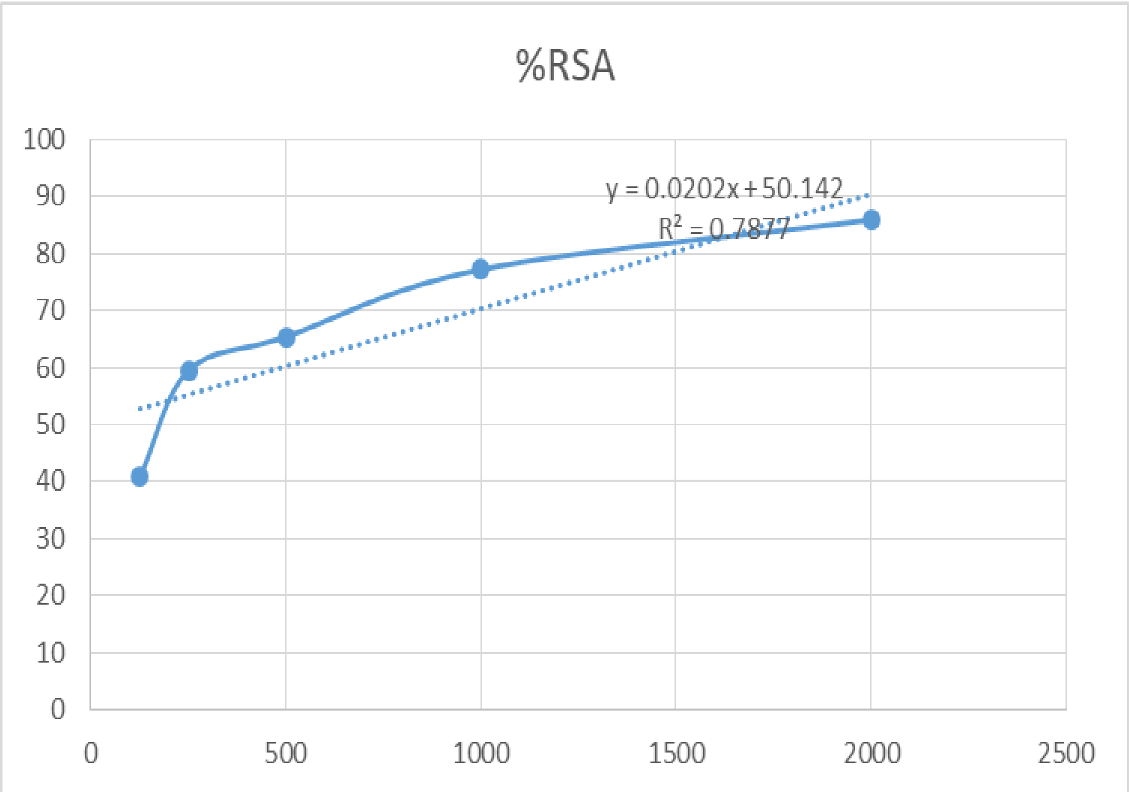

Appendix 4.5. The equation graph of Ascorbic acid scavenging activity

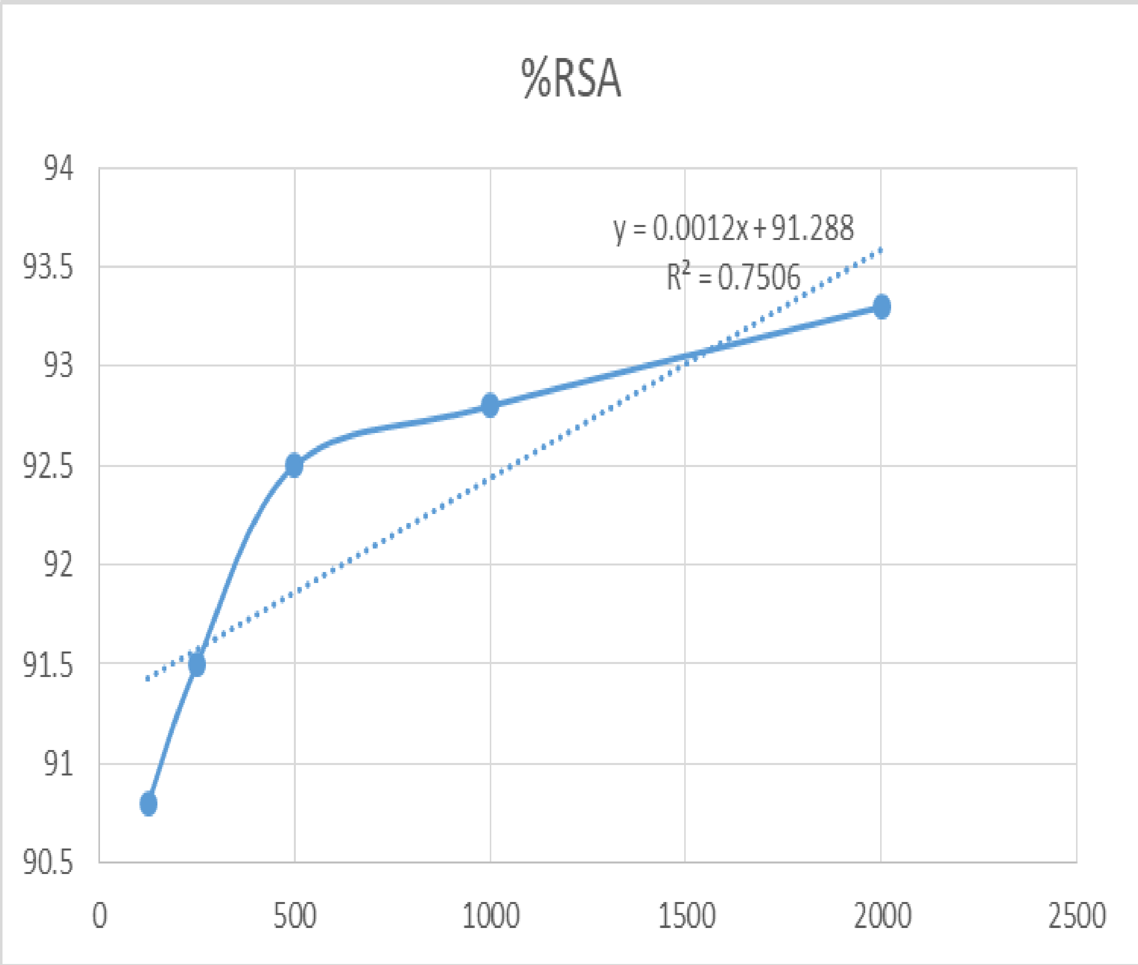

Appendix 5. The qualitative observation of MIC value

Green synthesized nanoparticles	Concentration (mg/ml)	Visual observation for bacterial growth as turbid			
		S.aur	E.col	S.pyo	P. au
ZnO	20	Not turbid	Not turbid	Not turbid	Not turbid
	10	Not turbid	Not turbid	Not turbid	Not turbid
	5	Not turbid	Not turbid	Not turbid	Turbid
	2.5	Turbid	Not turbid	Not turbid	Turbid
	1.25	Turbid	Turbid	Turbid	Turbid
	0.625	Turbid	Turbid	Turbid	Turbid
CuO	20	Not turbid	Not turbid	Not turbid	Not turbid
	10	Not turbid	Not turbid	Not turbid	Not turbid
	5	Not turbid	Not turbid	Not turbid	Not turbid
	2.5	Not turbid	Turbid	Turbid	Turbid
	1.25	Turbid	Turbid	Turbid	Turbid
	0.625	Turbid	Turbid	Turbid	Turbid
CuO/ZnO	20	Not turbid	Not turbid	Not turbid	Not turbid
	10	Not turbid	Not turbid	Not turbid	Not turbid
	5	Not turbid	Not turbid	Not turbid	Not turbid
	2.5	Not turbid	Not turbid	Not turbid	Not turbid
	1.25	Not turbid	Not turbid	Not turbid	Turbid
	0.625	Turbid	Turbid	Turbid	Turbid
ZnO-Cef	20	Not turbid	Not turbid	Not turbid	Not turbid
	10	Not turbid	Not turbid	Not turbid	Not turbid
	5	Not turbid	Not turbid	Not turbid	Not turbid
	2.5	Turbid	Not turbid	Not turbid	Not turbid
	1.25	Turbid	Turbid	Turbid	Turbid
	0.625	Turbid	Turbid	Turbid	Turbid

Appendix 6. Antibacterial MIC, and MBC, for GNPs, GNCs, and GNP-AB against *S. aureus*, *E. coli*, *S. pyogenes*, and *P. aeruginosa* bacteria.

GNps	**[](mg/ml)**	**Absorbance (UV) of bacterial growth before and after incubation**							
		S.aureus		*E.coli*		*S.pyogenes*		*P.aeruginosa*	
		Before	After	Before	After	Before	After	Before	After
ZnO	20	0.068	0.064	0.078	0.069	0.068	0.060	0.074	0.061
	10	0.063	0.060	0.065	0.049	0.059	0.047	0.069	0.069
	5	0.056	0.043	0.068	0.060	0.049	0.051	0.068	0.060
	2.5	0.042	0.038	0.058	0.052	0.049	0.049	0.061	0.552
	1.25	0.044	0.315	0.052	0.148	0.041	0.213	0.060	0.623
	0.625	0.038	0.647	0.052	0.217	0.042	0.418	0.057	0.654
CuO	20	0.082	0.080	0.093	0.073	0.087	0.087	0.083	0.079
	10	0.081	0.081	0.090	0.072	0.082	0.081	0.079	0.079
	5	0.074	0.075	0.080	0.048	0.080	0.078	0.073	0.072
	2.5	0.073	0.070	0.054	0.376	0.077	0.188	0.065	0.157
	1.25	0.055	0.578	0.054	0.382	0.076	0.219	0.058	0.153
	0.625	0.045	0.674	0.040	0.382	0.074	0.488	0.049	0.319
GCD-Z10.5	20	0.081	0.074	0.081	0.080	0.084	0.080	0.085	0.079
	10	0.078	0.073	0.080	0.080	0.081	0.081	0.084	0.079
	5	0.069	0.069	0.074	0.059	0.076	0.073	0.075	0.072
	2.5	0.052	0.045	0.068	0.051	0.076	0.074	0.074	0.074
	1.25	0.048	0.285	0.053	0.051	0.074	0.074	0.067	0.153
	0.625	0.042	0.516	0.053	0.398	0.070	0.382	0.060	0.319
ZnO-AB	20	0.063	0.060	0.065	0.064	0.069	0.068	0.065	0.065
	10	0.063	0.064	0.061	0.061	0.066	0.066	0.060	0.054
	5	0.057	0.057	0.051	0.050	0.065	0.061	0.053	0.053
	2.5	0.048	0.210	0.050	0.050	0.065	0.065	0.047	0.049
	1.25	0.041	0.521	0.049	0.479	0.062	0.218	0.044	0.306
	0.625	0.041	0.697	0.044	0.516	0.060	0.526	0.042	0.502